Experimental Characterisation of the Far Wake of a Modelled Floating Wind Turbine as a Function of Incoming Swell

Benyamin Schliffke

THESE DE DOCTORAT DE

L'ÉCOLE CENTRALE DE NANTES

ECOLE DOCTORALE N° 602
Sciences pour l'Ingénieur
Spécialité : Mécanique des milieux fluides

Par

Benyamin SCHLIFFKE

Caractérisation expérimentale de l'impact de la houle sur le comportement aérodynamique des éoliennes flottantes

Thèse présentée et soutenue à l'École Centrale de Nantes, le 16/02/2022
Unité de recherche : UMR 6598, Laboratoire de recherche en Hydrodynamique, Énergétique et Environnement Atmosphérique (LHEEA)

Rapporteurs avant soutenance :

Jeroen VAN-BEECK Professeur, Institut Von Karman, Sint-Genesius-Rode, Belgique
Axelle VIRÉ Professeure, Technical University of Delft, Pays-Bas

Composition du Jury :

Président :	Jeroen VAN-BEECK	Professeur, Institut Von Karman, Sint-Genesius-Rode, Belgique
Examinateurs :	Erin BACHYNSKI-POLIĆ	Professeure, N.T.N.U., Trondheim, Norvège
	Stéphane BARRE	Chargé de Recherche HDR, Grenoble INP
Dir. de thèse :	Sandrine AUBRUN-SANCHES	Professeure des universités, École Centrale de Nantes
Co-encadrant :	Boris CONAN	Maître de Conférences, École Centrale de Nantes

Invité :

	Vincent GUENARD	Ingénieur, ADEME, Valbonne

Experimental Characterisation of the Far Wake of a Modelled Floating Wind Turbine as a Function of Incoming Swell

Benyamin Schliffke

SEMREV+ & DAUC

LHEEA

Centrale Nantes

Encadrant: Prof. Sandrine Aubrun (ECN - LHEEA)

Co-encadrant: Dr. Boris Conan (ECN - LHEEA)

16/02/2022

Abstract

Decarbonising the energy sector is a major challenge of our times. Renewable energies offer a viable solution. Offshore wind alone can contribute a large portion of the energy demand. To access the large wind resource further offshore floating wind turbines are necessary, as fixed bottom turbines become too expensive to install due to the increasingly deeper waters. Floating offshore wind turbines (FOWTs) are a potential source for increased offshore energy production. As the technology is still in a pre-industrial state several questions remain to be addressed. Using physical modelling at a reduced scale, this thesis aims to investigate the unsteady behaviour and the development of the wake in a simplified FOWT model. A porous disc model is placed in an atmospheric wind tunnel and subjected to a range of idealised and realistic motions. Each degree of freedom is studied separately and all three degrees of freedom (Dof) together. The effects of induced sinusoidal surge motion on the characteristics of the model's wake up to 8 rotor diameters (D) downstream are studied. The results show largely unchanged mean velocity values but modified turbulence intensity and turbulent kinetic energy. A turbulent kinetic energy (TKE) budget analysis reveals that the turbulent production and dissipation are enhanced with the introduction of idealised surge motion. Increased momentum transport in the shear layer is responsible for the increased turbulent production. The energy spectra of the flow are affected by the introduction of motion. The motion must be sufficiently strong in order to observe a response. Idealised single frequency motion leads to detectable peaks at the imposed motion frequency in the wake flow's energy spectra. A shift to higher frequencies can be observed for several motion regimes. Realistic 3 Dof motion affects the wake differently compared to idealised 3 Dof motion.

Résumé

L'un des défis les plus importants auxquels l'humanité est confrontée est l'adaptation au changement climatique. Les émissions de dioxyde de carbone (CO_2) dues à l'activité humaine étant le moteur du changement climatique, il est très important de réduire radicalement les émissions de CO_2 dans tous les secteurs d'activité. Le secteur de l'énergie est un émetteur important en raison de l'utilisation continue et généralisée des combustibles fossiles. Ce secteur est crucial pour toutes les autres parties de l'activité humaine. Sa décarbonisation est donc une nécessité absolue. Les énergies renouvelables comme le vent et le soleil sont essentielles pour atteindre cet objectif. L'énergie éolienne en mer a, à elle seule, le potentiel de contribuer à l'approvisionnement mondial en électricité à hauteur de $420\,PWh$, selon le 2019 Offshore Wind Outlook publié par l'Agence internationale de l'énergie (AIE). C'est plus que la demande mondiale totale d'énergie en 2018 (IEA, 2019). Afin d'utiliser le potentiel de l'éolienne en mer, il est nécessaire d'aller plus loin des côtes, là où la ressource éolienne est plus importante. Aller plus loin en mer réduit également les conflits de partage d'usage. Par ailleurs, à mesure que les eaux deviennent plus profondes, les coûts d'installation de turbines fixes deviennent prohibitifs. D'autres solutions sont donc nécessaires.

Les éoliennes flottantes en mer sont une source potentielle d'augmentation de la production d'énergie en mer. Leur principal avantage est qu'elles peuvent être ancrées dans des eaux beaucoup plus profondes que les éoliennes fixes. Les éoliennes flottantes permettent donc d'accéder à des ressources éoliennes plus élevées et plus régulières plus au large, tout en étant presque invisibles depuis la côte. Les prototypes opérationnels et les parcs sont encore rares, Hywind en Écosse étant un parc opérationnel depuis 2017 et plusieurs autres étant actuellement installés en Europe (WindEurope, 2020). Un certain nombre de démonstrateurs ont été installés dans le monde, un exemple étant FLOATGEN actuellement installé sur le site d'essai en mer SEM-REV de Centrale Nantes (BW Ideol, Centrale Nantes, 2014). La technologie étant encore dans une phase pré-industrielle, peu de données de terrain sont disponibles. Les quelques données qui existent ne sont pas diffusées car les leaders du secteur sont des acteurs sur un marché très concurrentiel.

Les effets du mouvement de l'éolienne sur son sillage suscitent un intérêt croissant. Le sillage d'une turbine entraîne des pertes de production pour les turbines en aval. Cela soulève la question de savoir si le sillage d'une éolienne flottante peut être

considéré comme similaire à celui d'une turbine fixe ou s'il existe des caractéristiques spécifiques du sillage d'une éolienne flottante qui doivent être prises en compte. Par conséquent, plusieurs questions relatives au sillage d'une éolienne flottante restent sans réponse. L'une de ces questions concerne le comportement et le développement du sillage d'une éolienne flottante dans différentes conditions de mer.

Les sillages des éoliennes fixes ont fait l'objet d'études approfondies, tant numériques qu'expérimentales, à l'échelle réelle ou réduite. Les sillages des éoliennes augmentent les charges de fatigue sur les turbines en aval en raison des turbulences supplémentaires. La production d'énergie est réduite en raison du déficit énergétique du sillage par rapport au flux incident non perturbé. Le flux incident lui-même joue également un rôle important dans le développement du sillage d'une éolienne. Ce flux régissent les caractéristiques des méandres du sillage. En même temps, la diffusion turbulente à l'intérieur du sillage dépend également des conditions du flux incident. L'introduction d'un mouvement dans l'éolienne devrait modifier davantage les caractéristiques du sillage. L'excitation de la turbine à des fréquences du même ordre de grandeur que les fréquences caractéristiques des instabilités du sillage peut avoir des conséquences inattendues sur les méandres du sillage ainsi que sur les processus de diffusion dans le sillage. Ceci est dû à la non-linéarité inhérente aux processus impliqués, ce qui rend également les prédictions difficiles. Les expériences menées au cours de ce travail tentent d'identifier les processus et les quantités impactées par l'introduction du mouvement.

D'un point de vue physique, des effets positifs et négatifs sur le sillage peuvent être attendus. Premièrement, l'introduction de mouvement peut agir comme un filtre dans l'écoulement, en retirant de l'énergie cinétique. Cela entraînerait un déficit de vitesse plus important dans le sillage, car moins d'énergie est disponible. Une éventuelle turbine en aval produirait donc moins d'énergie. Deuxièmement, l'introduction du mouvement peut ajouter de l'énergie à l'écoulement, car l'éolienne flottante agit comme un moyen de transférer l'énergie des vagues de surface et de la houle au sillage. Ce mécanisme permettrait de mettre davantage d'énergie dans l'écoulement et, par conséquent, plus d'energie à la disposition des turbines en aval, d'où une production d'énergie plus élevée. Un argument similaire peut être avancé en ce qui concerne la turbulence. Des niveaux modifiés de turbulence dans le sillage modifieraient les charges de fatigue subies par les turbines en aval. Les sillages de deux turbines interagissent également l'un avec l'autre. La modification de la fréquence de leurs interactions peut également avoir des effets sur les turbines en aval, à la fois en termes de production d'énergie et de charges de fatigue.

Cette thèse étudie le comportement aérodynamique du sillage d'une éolienne flottante en fonction du mouvement imposé afin d'identifier les effets dominants sur le sillage de l'éolienne. L'idée est d'imposer un mouvement caractéristique à un modèle d'éolienne dans une soufflerie atmosphérique. La modélisation physique à une échelle réduite présente de nombreux avantages par rapport aux autres méthodes. L'utilisation d'une soufflerie permet de réaliser des expériences dans un environnement

contrôlé, garantissant des résultats reproductibles. Les conditions d'entrée peuvent être ajustées de manière à ce qu'elles soient représentatives d'une couche limite atmosphérique. L'éolienne est modélisée à l'aide d'un disque poreux. En utilisant les simulations de mouvements d'un flotteur donné, une série temporelle du mouvement est mise à l'échelle conformément aux lois de similitude géométrique. Le système de mouvement nécessaire est conçu en conséquence. Les trois degrés de liberté (DDL) les plus importants sont sélectionnés. Le système de mouvement peut ainsi reproduire un mouvement à trois DDL. Chaque DDL peut être contrôlé indépendamment des autres. Des régimes de mouvement réalistes et idéalisés sont modélisés. Le modèle est ensuite placé dans un écoulement de couche limite atmosphérique à l'échelle de la soufflerie. Différentes techniques de mesure sont utilisées pour saisir l'effet du mouvement imposé sur le sillage. L'utilisation d'une variété de technologies ouvre une multitude d'analyses possibles révélant différentes caractéristiques du sillage d'une éolienne flottante.

Il est nécessaire d'émuler le mieux possible les conditions rencontrées par un éolienne flottante opérationnelle. C'est dans cette optique que le travail présenté dans cette thèse vise à combler le manque de connaissances. La soufflerie atmosphérique du LHEEA/Centrale Nantes est utilisée. Un modèle d'éolienne est placé dans un écoulement de couche limite atmosphérique modélisé et soumis à divers mouvements pour trois modes distincts (cavalement, pilonnement et tangage) et pour les trois modes ensemble. Les régimes de mouvement idéalisés et réalistes sont étudiés au cours de cette thèse.

Lors du développement du système de mouvement à 3 DDL, un certain nombre d'observations ont été faites. Le système de mouvement 3 DDL se compose de deux moteurs linéaires et d'un élément rotatif qui peuvent être utilisés de manière modulaire. L'unité de commande centrale permet une utilisation polyvalente du système, avec une précision de 2% et une résolution temporelle de $1\,ms$. Il existe un décalage de $4\,ms$ entre la position commandée et la position réelle. À l'heure actuelle, on pense que ce système de mouvement est l'un des rares disponibles dans le monde.

L'autre élément central des préparatifs a été le développement d'une couche limite atmosphérique modélisée. L'écoulement remplit la plupart des critères proposés par la directive VDI 3783 (VDI, 2000). L'exception est la longueur de rugosité, qui est trop petite. Les données de terrain suggèrent que la longueur de rugosité calculée pour la couche limite modélisée est en fait réaliste pour les eaux côtières (He et al., 2021). L'importance d'une couche limite de haute fidélité est soulignée par la sensibilité du sillage de la turbine à l'écoulement incident.

Comment le mouvement de la turbine affecte-t-il le développement du sillage ?

L'effet global du mouvement idéalisé de cavalement or d'embardée sur le sillage est limité pour les valeurs moyennes et turbulentes. La tendance générale des valeurs

moyennes et turbulentes indique des processus de résorption du sillage légèrement accélérés. Cette tendance a depuis été confirmée par Fontanella et al. (2021).

Y a-t-il des différences par rapport à un modèle stationnaire ? Les quantités moyennes ne sont que légèrement affectées par l'introduction du mouvement de cavalement. Les profils verticaux des quantités moyennes et turbulentes le soulignent, montrant des changements de l'ordre de 5% pour l'intensité de turbulence. La distribution spatiale de ces mêmes quantités moyennes et turbulentes est également légèrement affectée par l'introduction du mouvement de cavalement. Des indications d'une résorption accélérée du sillage peuvent être trouvées dans les niveaux accrus d'intensité de turbulence ajoutée au sillage, de TKE et de $\overline{u'w'}$ pour $f_{red} \geq 0.1$ par rapport à une turbine fixe. Ces résultats semblent confirmer ceux discutés dans Schliffke et al. (2020). La couche de cisaillement plus épaisse et les zones plus larges de TKE accrue indiquent des processus de mélange améliorés dans les régions de sillage proche et intermédiaire.

Les résultats dépendent-ils de la fréquence et de l'amplitude des mouvements ? Oui, mais la dépendance n'est pas toujours claire. Les données suggèrent qu'un mouvement plus fort a un effet plus important sur le sillage. Un mouvement idéalisé n'a pas le même effet sur le sillage qu'un mouvement réaliste.

Quelles sont les explications physiques des différences observées ? La résorption accélérée observée est due à l'augmentation du transport de la quantité de mouvement dans la couche de cisaillement du sillage du disque poreux, comme l'a révélé l'analyse du budget TKE. Le transport de quantité de mouvement est augmenté d'environ 10% et semble être indépendant des fréquences de mouvement cavalement testées dans le cadre de ce travail. Il est possible que les niveaux réels de TKE mesurés ici soient sous-estimés par rapport à une turbine modèle rotative (Camp and Cal, 2016). Une analyse du bilan TKE dans le sillage d'un modèle rotatif est donc nécessaire pour vérifier ces résultats.

Y a-t-il une signature spectrale identifiable du mouvement de l'éolienne sur le sillage ?

Oui, lorsqu'un certain seuil est dépassé. Un mouvement de 1 DDL imposé à des fréquences ou des amplitudes suffisamment élevées laisse une signature claire dans le spectre d'énergie du sillage. Ceci est vrai pour les mouvements de cavalement, embardée et pilonnement, pour les régimes de mouvement testés. Pour le mouvement de cavalement, le seuil d'une fréquence minimale se situe autour de $f_{red} = 0.18$ et à des amplitudes de $0.25\,D$. Même la fréquence de mouvement la plus élevée testée pour le pilonnement à $f_{red} = 0.3$ ne fournit pas de traces claires dans le spectre à une amplitude de $0.0125\,D$. Il est intéressant de noter que les amplitudes supérieures à $0.03125\,D$ entraînent des pics détectables dans les spectres. Les fréquences et les amplitudes testées pour le mouvement de tangage ne présentent pas de pics identifiables dans les spectres du sillage. Des expériences plus détaillées sont nécessaires

pour mieux définir ces seuils. Le mouvement caractéristique idéalisé à 3 DDL montre un petit pic associé au mouvement de cavalement. Le mouvement de cavalement est le DDL dominant dans le régime de mouvement 3 DDL idéalisé. Les mouvements 3 DDL réalistes ne montrent pas de pics clairs dans les spectres d'énergie de l'écoulement de sillage.

Comment la réponse instable du sillage se développe-t-elle latéralement et verticalement ? La signature peut être détectée à $4.6\,D$ dans les cas où le mouvement est suffisamment fort. La distance à laquelle la signature du mouvement peut être détectée en aval reste à établir dans le cadre de travaux futurs. Latéralement, la signature la plus claire peut être trouvée le long de la ligne centrale de l'éolienne à la hauteur du moyeu. Les effets du mouvement deviennent moins clairs vers les frontières du sillage. Verticalement, la couche de cisaillement, à une hauteur juste au-dessus de l'extrémité supérieure de l'éolienne, présente les pics les plus forts dans les spectres d'énergie.

Toutes les composantes de l'écoulement sont-elles affectées de la même manière par le mouvement imposé ? Les composantes longitudinale et verticale de l'écoulement sont affectées par le mouvement de cavalement. Lorsqu'on impose un mouvement d'embardée, les composantes longitudinale et latérale de l'écoulement montrent des réponses claires dans les spectres du sillage. Contrairement au cavalement, la variation de l'amplitude du mouvement d'embardée n'affecte pas aussi clairement l'amplitude du pic.

La réponse dynamique du sillage dépend-elle de la fréquence et de l'amplitude des mouvements ? Oui. Ceci est plus clair quand on applique un mouvement 3 DDL idéalisé et réaliste. En ce qui concerne le mouvement 3 DDL idéalisé, la cohérence entre le spectre de mouvement et l'écoulement du sillage montre une réponse claire pour la fréquence du mouvement de cavalement imposé, tandis que des réponses faibles peuvent être identifiées aux fréquences de pilonnement et de tangage imposées. Ceci indique que la fonction de transfert entre le mouvement du flotteur et l'énergie du sillage a une composante linéaire. Le manque de cohérence en ce qui concerne le mouvement réaliste indique que les interactions non linéaires entre le sillage et le mouvement sont prédominantes. Les différences dans la vitesse moyenne normalisée et l'intensité de la turbulence dans le sillage entre les cas de mouvement idéalisé et réaliste peuvent être considérées comme des indicateurs supplémentaires d'interactions non linéaires entre la turbine en mouvement et son sillage. Les résultats indiquent que les processus de résorption du sillage sont modifiés pour le mouvement réaliste par rapport au mouvement idéalisé.

List of Figures

List of Tables

Contents

Chapter 1

Introduction

One of the most important challenge facing humankind is adapting to climate change. As carbon-dioxide (CO_2) emissions driven by human activity are the driving force of climate change, it is of great importance to drastically reduce CO_2 emissions from all sectors of activity. The energy sector is an important emitter due to the continued wide spread use of fossil fuels. This sector is crucial for all other parts of human activity, thus decarbonisation is of high necessity. Renewable energies like wind and solar are central to achieving this goal. Offshore wind power alone has the potential to contribute $420\,PWh$ to the global power supply, according to the 2019 Offshore Wind Outlook published by the International Energy Agency (IEA). This is more than the total global demand for energy in 2018 (IEA, 2019). In order to use offshore wind power's potential it is necessary to go further offshore, where more wind resource is available. Going further offshore also reduces the number of other parties with interests in the area. As the waters get deeper the costs of installing fixed bottom turbines becomes prohibitive. Thus other solutions are necessary.

Floating offshore wind-turbines (FOWTs) are a potential source for increased offshore energy production. Their main advantage being that they can be anchored in significantly deeper waters than fixed bottom offshore wind-turbines. FOWTs thus provide access to higher and steadier wind resources further offshore, while being almost invisible from the coast. Operational prototype FOWTs and parks are still rare, with Hywind in Scotland being an operational park since 2017 and several others being installed around Europe around the time of writing (WindEurope, 2020). A number of demonstrators have been installed around the world, an example being FLOATGEN currently installed at Centrale Nantes' SEM-REV offshore test site (BW Ideol, Centrale Nantes, 2014). As the technology is still in a pre-industrial phase, little field data is available. The little data that does exist is not disseminated as the industry leaders in the sector are in a highly competitive market.

With the development of FOWT parks the effects of the turbine's motion on its wake are of growing interest. A turbine's wake leads to production losses for downstream turbines. This raises the question whether the wake of an FOWT can be considered similar to that of a fixed turbine or whether there are specific

characteristics of an FOWT's wake that must be taken into account. Consequently several questions related to an FOWT's wake are unanswered. One of these questions relates to the behaviour and the development of an FOWT's wake in different sea conditions.

The wakes of fixed wind turbines have been studied extensively, both numerically and experimentally at full and reduced scales. Wind turbine wakes increase fatigue loads on downstream turbines through added turbulence. The power production is reduced due to the wake's energy deficit compared to the undisturbed inflow. The inflow itself also plays an important role in the development of a wind turbine's wake. They govern wake's meandering characteristics. At the same time the turbulent diffusion within the wake is also dependent on the inflow conditions. Introducing motion to the turbine is expected to further modify the characteristics of the wake. Excitation of the turbine at frequencies in the same order of magnitude as the characteristic frequencies of the boundary layer can lead to unexpected consequences on the wake's meandering as well as the diffusive processes within the wake. This is due to the non-linearity inherent to the processes involved, which also makes predictions difficult. The experiments conducted in the course of this work attempt to identify the processes and quantities impacted by the introduction of motion.

From a physical point of view both positive and negative effects on the wake can be expected. First, the introduction of motion may act as a filter in the flow, removing kinetic energy. This would lead to a higher velocity deficit in the wake as less energy is available. A potential downstream turbine would thus produce less power. Second, the introduction of motion may add energy to the flow, as the FOWT acts as a medium to transfer energy from the surface waves and swell to the wake. This mechanism would lead to more energy being available to the flow and consequently the downstream turbines resulting in higher energy production. A similar argument can be made when considering turbulence. Modified levels of turbulence in the wake would change the fatigue loads experienced by the downstream turbines. The wakes of two turbines also interact with each other. Modifying the frequency of their interactions can also have effects on the downstream turbines, both in terms of power production and fatigue loads.

This thesis investigates the aerodynamic behaviour of the wake of an FOWT as a function of imposed motion to identify the dominating effects on the turbine's wake. The idea is to impose characteristic motion on a model wind turbine in an atmospheric wind tunnel. Physical modelling at a reduced scale has numerous advantages compared to other methods. Using a wind tunnel allows for experiments in a controlled environment, assuring reproducible results. The inflow conditions can be adjusted in such a way that they are representative of an atmospheric boundary layer (ABL). The inherent variability, driven by meso-scale phenomena, of the natural ABL does not affect the wind tunnel flow. It is thus possible to measure physical processes that would be difficult to capture in field measurements, when statistically converged data is necessary.

The wind-turbine is modelled using an actuator disc. Using numerically modelled data of a given floater, a time-series of the motion is down scaled according to geometric similarity laws. The necessary motion system is designed accordingly. The three most important degrees of freedom (Dof) are selected. The motion system can thus reproduce 3 Dof motion. Each Dof can also be controllen independently from the others. Both realistic and idealised motion regimes are modelled. The model is then placed in a scaled atmospheric boundary layer flow in the wind tunnel. Different measurement techniques are used to capture the effect of the imposed motion on the wake. Using a variety of technologies opens up a multitude of possible analyses revealing different characteristics of the FOWT's wake.

In this thesis the methods described above are applied to investigate the wake of a modelled FOWT in an atmospheric wind tunnel. In a first step, mean and turbulent quantities, like the turbulence intensity I, the turbulent kinetic energy TKE and the shear stresses, are investigated for idealised surge motion only. These quantities allow a first assessment of the principle processes responsible for any possible modifications. Their vertical profiles measured in the wake can give an estimation of the degree of changes to expect. The most effective motion regimes can also be identified at this point. Then the spatial development of said quantities is analysed in order to verify whether the conclusions from the vertical profiles hold in a large part of the wake. The results are discussed in the context of existing literature on the subject.

In a second step, the physical processes impacted by the introduction of motion are identified. For this purpose an analysis of the TKE budget is conducted. The effects of motion on each component of the budget can be assessed, delivering a good understanding of the relation of physical processes in the wake of an FOWT and their dependence on the imposed motion.

In a third step, the unsteady characteristics of an FOWT wake are analysed. Limited literature is available on the unsteady characteristics of an FOWT's wake. In this context a variety of motion regimes will be investigated. These include idealised single Dof and three Dof motion. Realistic motion regimes are also used. The effects of each Dof alone and combined will be studied. Also possible differences between idealised and realistic motion regimes will be assessed.

Combining the results of the three parts of the planned work would enable a first understanding of what role the motion of an FOWT plays in the development of its wake. The knowledge of the physical processes modified by the motion and the unsteady behaviour could help develop more precise models of FOWT wakes. These models can in turn help reducing the cost of floating offshore wind energy, increasing its competitivity compared to other sources of energy. The study of the unsteady behaviour of the wake is a part of the knowledge gap identified and where this thesis adds new knowledge to the current state of the art.

Chapter 2

The State of the Art

This chapter gives an overview of the literature that motivates this thesis. The chapter consists of two parts. The first part deals with turbulent boundary layers and their modelling theory. The second part presents the state of the art regarding wind turbines, focusing on floating turbines, and their wakes.

Regarding turbulent boundary layers, an introduction into the basic mathematical and qualitative knowledge required to understand turbulent boundary layer flows is given (section 2.1.1). The atmospheric boundary layer, as a specific case of a turbulent boundary layer, is then presented in section 2.1.2. Section 2.1.3 presents the theory allowing us to model an atmospheric boundary layer in a wind tunnel.

The current understanding of wind turbines and their wakes is presented (section 2.2). The basic functionality of a wind turbine is presented (section 2.2.1), followed by a more detailed description of a wind turbine's wake (section 2.2.2). The specifics of floating offshore wind turbine's (FOWT) wakes are then described (section 2.3). The research questions resulting from the current state of the art are presented and discussed in section 2.4.

2.1 The Atmospheric Boundary Layer

2.1.1 Atmospheric Boundary Layer Flows

Frost and Moulden say in the preface of their Handbook of Turbulence, "turbulence takes place in practically all flow situations that occur naturally or in modern technological systems" (Frost, 2012). This is particularly pertinent with reference to this thesis, which deals with both natural flows (the atmospheric boundary layer) and modern technology (floating wind turbines). Other technological systems that are linked to turbulent flows include ship design, wind turbine blade and aeroplane wing optimisation, propulsion systems and vehicle design. As turbulent flows are instationary and three dimensional phenomena, they change in time and space. Starting from global atmospheric circulation flows, the relevant assumptions, simplifications and resulting limitations regarding wind tunnel modelling need to be

taken into consideration.

The atmospheric boundary layer is characterised by turbulent processes. These processes govern the turbulent transport of energy, mass and momentum. Thus these quantities are conserved in the flow. The Navier-Stokes equation for momentum conservation in an incompressible Newtonian fluid (equation 2.1) governs the processes in the atmospheric boundary layer. It is a second order non-linear differential equation. The Navier-Stokes equation for momentum conservation assumes that only surface forces influence the fluid elements, while also considering gravity to be negligible in atmospheric boundary layer flows. The sum of the temporal change and the advective forces is thus dependent on pressure and surface forces:

$$\frac{\partial u_i}{\partial t} + u_j \frac{\partial u_i}{\partial x_j} = \frac{1}{\rho} \frac{\partial}{\partial x_j} \left(-p\delta_{ij} + 2\mu s_{ij} \right) \tag{2.1}$$

where ρ is density, p is pressure, μ is dynamic viscosity, δ_{ij} is the Kronecker-Delta and s_{ij} is the shear tensor, defined as:

$$s_{ij} = \frac{1}{2} \left(\frac{\partial \tilde{u}_i}{\partial x_j} + \frac{\partial \tilde{u}_j}{\partial x_i} \right) \tag{2.2}$$

To describe turbulent flows the measured value (u_i) is decomposed into mean flow component, U, and a turbulent component, u':

$$u_i = U + u' \tag{2.3}$$

Applying this method to the Navier-Stokes equation for momentum conservation (equation 2.1) results in the Reynolds Averaged Navier Stokes (RANS) equation (2.4), where the bar presents temporally averaged quantities:

$$0 = U_j \frac{\partial U_i}{\partial x_j} - \frac{1}{\rho} \frac{\partial}{\partial x_j} \left(-P\delta_{ij} + 2\mu S_{ij} - \rho \overline{u_i u_j} \right) \tag{2.4}$$

The RANS equation is a temporally averaged and rearranged version of the law of conservation of momentum. The parentheses contain the total stress tensor. This tensor is comprised of the normal stress due to pressure $-P\delta_{ij}$, the viscous friction stress $2\mu S_{ij}$ and the temporally averaged Reynolds stress $\rho \overline{u_i u_j}$. The Reynolds stresses are the result of mathematical transformations and averaging applied to the Navier-Stokes equation for momentum conservation. It is evident that the Reynolds stresses and friction stresses have comparable effects on the mean flow. As these quantities are most pronounced in shear layers, it is necessary to understand the vertical structure of the atmospheric boundary layer. It will be presented in the

following section.

2.1.2 Structure of the Atmospheric Boundary Layer

As with all flows, the Earth's atmosphere consists of a number of layers. Those most relevant for this study are presented here. It is beneficial to the understanding of the specific case of the atmospheric boundary layer to have a general idea of the processes dominant in the troposphere.

The troposphere covers the first $11\,km$ from the ground upwards. It is the lowest layer of the Earth's atmosphere. The boundary layer is the lowest part of the troposphere and is affected by the ground. Its height ranges between $100\,m$ and $2\,km$. The free atmosphere refers to all layers above the boundary layer. In the free atmosphere the pressure gradient and Coriolis force are considered equal, as this part of the atmosphere is not influenced by friction from the ground. As a result, the geostrophic wind develops. It has two components as defined in Holton (2004):

$$\begin{aligned} v_g &= \frac{1}{f\rho}\frac{\partial P}{\partial x} \\ u_g &= -\frac{1}{f\rho}\frac{\partial P}{\partial y} \end{aligned} \tag{2.5}$$

where $f = 2\,\Omega \sin\varphi$ is the Coriolis parameter, Ω is the Earth's rotational velocity, φ is the latitude, P represents the pressure, ρ the air's density and x is the zonal direction and y the meridional direction, u_g and v_g are the eastward and northward flow components, respectively. As the balance between Coriolis force and pressure gradient dictates, the geostrophic wind follows the isobars in the free atmosphere. This approach presents a first approximation of the real flow conditions.

As the movement in the atmosphere follows a curved pattern in reality, the centrifugal force is added to the geostrophic wind resulting in the gradient wind. Equation 2.6 describes the gradient wind (V) in polar coordinates, as is standard in meteorological literature (e.g. Holton, 2004):

$$fV + \frac{V^2}{r} = \frac{1}{\rho}\frac{\partial P}{\partial r} \tag{2.6}$$

The radius of the eddy is noted as r. The gradient wind is a more precise approximation of the atmospheric flow in the free atmosphere (Holton, 2004).

As the geostrophic and gradient winds are not affected by friction or thermal fluxes from the earth's surface, these approximations cannot accurately represent the winds encountered in the boundary layer. More complex models are necessary. More specifically, the boundary layer is split into three sublayers, namely the viscous sublayer, the Prandtl layer and the Eckman layer (Etling, 2008). Figure 2.1 depicts

the general structure of the atmospheric boundary layer. Each sublayer is briefly described below.

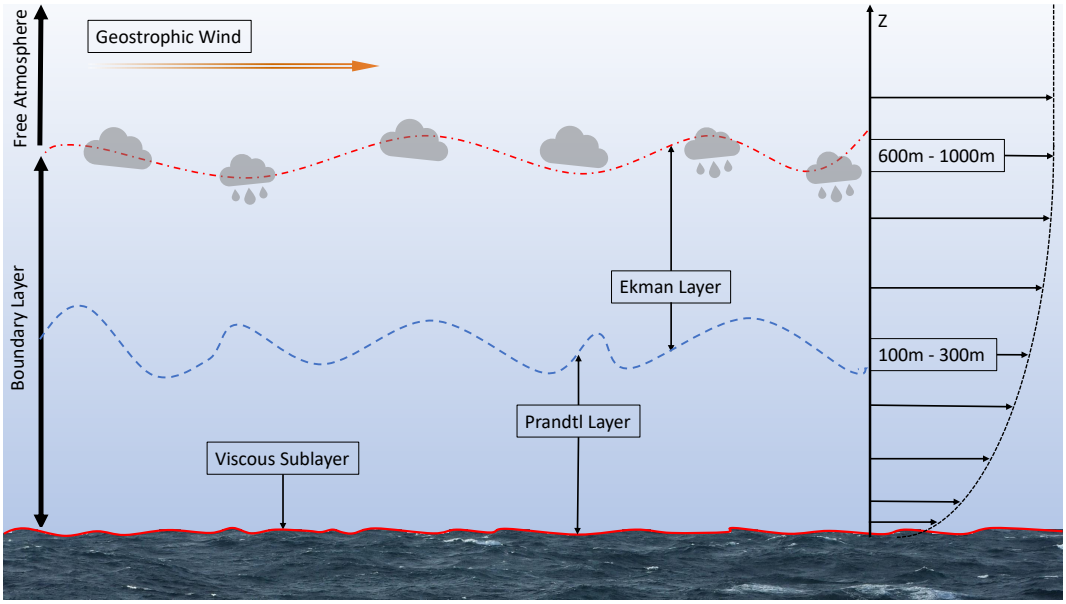

Figure 2.1 – Sketch of the atmospheric boundary layer over a body of water. Adapted from Harms (2010).

As the name viscous sublayer suggests, viscous effects are dominant. The wind speed is considered to be close to 0 as friction has a strong impact. The viscosity effectively eliminates any turbulent effects. As heat and momentum transport is accomplished by molecular processes in this sublayer, they have no influence on processes dominating the remaining boundary layer. The viscous sublayer covers the first few millimetres above the ground.

The Prandtl layer, situated above the viscous sublayer and spanning about 10 % on the entire boundary layer height, is dominated by increased, yet more or less constant, turbulence and shear stress. These quantities vary around 10 % of their respective mean values. Friction near the surface is responsible for a considerable velocity gradient in the lower part of the layer. An approach to calculate the wind profile in the first few hundred metres of the boundary is the power law wind profile:

$$U(z) = U_r \left(\frac{z}{z_r} \right)^{\alpha} \tag{2.7}$$

U denotes the wind speed dependent on the height z. U_r is the velocity at a reference height z_r. α is the profile exponent and is often used to characterise a boundary layer wind velocity profile. The exponential wind profile is a simple approach that requires little data. In the Prandtl layer the more detailed logarithmic wind profile

can be applied (equation 2.8). It requires knowledge of surface characteristics:

$$U(z) = \frac{U_*}{\kappa} \cdot \ln\left(\frac{z}{z_0}\right) \tag{2.8}$$

U denotes the wind speed dependent on the height z. U_* is the friction velocity and κ the von-Karman constant. z_0 is the roughness length. Equation 2.8 approximates the wind speed at a given height above ground. As the Coriolis force is negligible in the Prandtl layer the mean wind direction can be assumed to be constant in a vertical plane (Etling, 2008).

The Eckman layer is situated on top of the Prandtl layer. In the Eckman layer the average wind velocity increases due to a reduction in the influence of the ground friction. The Coriolis force becomes increasingly important, thus influencing the wind direction causing it to follow the geostrophic wind. The wind velocity in the Eckman layer reaches the magnitude of the geostrophic wind.

The model of the atmosphere and its boundary layer described above can accurately capture the true behaviour of the atmospheric flows encountered over most surfaces. Given that this thesis aims to investigate floating wind turbines, the characteristics of the sea surface are relevant. Despite the waves, tides and currents that affect the sea surface, the sea is considered a smooth surface in the VDI Guideline 3783 (VDI, 2000). Consequently the model of the boundary layer holds. The precise value of the surface roughness at sea depends on the wind and wave conditions at a given location (Toba and Ebuchi, 1991). Reference guidelines (e.g.: VDI, 2000) give the range of acceptable roughness lengths for flows over water surfaces between $10^{-5}\,m$ and $10^{-3}\,m$. Newer field data suggests that smaller values in the range of $10^{-6}\,m$ are also possible in coastal waters (He et al., 2021).

2.1.3 Physical Modelling of Boundary Layer Flows

Boundary Layer Turbulence

The basic scales of the turbulent energy distribution in the atmosphere were first shown by van der Hoven (Van der Hoven, 1957). The distribution is comprised of the range of scales, from the global scale to local microscales and down to the dissipation of the smallest eddies. The distribution enables one to distinguish between large scale phenomena, such as weather, and small scale phenomena (turbulence) due to the spectral gap between these scales. The universal validity of the van der Hoven spectrum is contested but it suffices as a qualitative introduction to atmospheric motion Etling (2008).

Etling (2008) understands turbulence as the superimposed high frequency, three-dimensional variability on a mean flow. It is generally understood that mixing and transport processes are caused by turbulence. The energy in the eddies is transported downwards in scale through interaction between eddies of different sizes

and strengths. Large eddies dissipate into ever smaller eddies, thus passing the energy on, until they are dissipated by friction. This phenomenon is known as the energy cascade and is central to turbulence theory. An eddy can never be larger than the depth of the boundary layer. Thus, there is a natural limitation on the maximum size of eddies in a given flow.

Taylor (1938) introduced the hypothesis of frozen turbulence. Here eddies are invariantly advected by the mean wind. Thus, measuring at a given position over a certain time span delivers the same results as measuring along the streamwise direction at any given time. The hypothesis is limited to scenarios where the variability is small compared to the mean wind (Stull, 1988). This restriction infers that the eddies can be seen as stationary in their structure while passing through a plane perpendicular to the mean flow direction. This would suggest that it is possible to determine the size of an eddy from its frequency, or period, and vice versa (equation 2.9):

$$L = \frac{U}{f_{eddy}} \tag{2.9}$$

where L is the characteristic length of the eddy, U is the local flow velocity, and f_{eddy} is the eddy's frequency. Large eddies have low frequencies, while small eddies have high frequencies.

Similarity Theory and Reynolds-Independence

Similarity Theory is based on a set of dimensionless values. The theory ensures comparability between different flows. A general definition was given by Monin and Obukhov (Monin and Obukhov, 1954). To obtain these dimensionless values the Buckingham-Pi-Theory (Buckingham, 1914) is applied to the fundamental equations of motion in order to conduct a dimension analysis. This process results in a set of dimensionless values that can be used as a reference for the similarity of turbulent flows. These values include the Rossby Number (Ro), the Reynolds Number (Re) and the densimetric Froude Number (Fr_d). These are defined as:

$$Ro = \frac{u_{ref}}{L_{ref} \cdot f} \tag{2.10}$$

$$Re = \frac{u_{ref} \cdot L_{ref}}{\nu} \tag{2.11}$$

$$Fr_d = u_{ref} \sqrt{L_{ref} g \frac{\rho - \rho_{sur}}{\rho}} \tag{2.12}$$

with u_{ref} being the reference speed, L_{ref} the reference length, f the Coriolis force, ν the kinematic viscosity, g the gravitational acceleration, ρ the fluid's density and ρ_{sur} the density of the surrounding fluid. The relation of inertia forces to the Coriolis force is described by the Rossby Number (equation 2.10). The Reynolds Number (equation 2.11) indicates the ratio of inertia forces to viscous forces, giving information about the significance of turbulent (and laminar) effects in the flow. The densimetric Froude Number (equation 2.12), the ratio of inertia to buoyancy, is an indicator for stratification. There is a large variety of other dimensionless values. These two are relevant for physical flow modelling and are therefore presented here. For the flows to be considered similar, these values must be identical in each flow.

In practice it is impossible to match all the dimensionless values in a modelled flow. It is therefore necessary to define the values that must match in each flow. Which values are defined may vary from experiment to experiment.

When focusing on the Prandtl layer the effect of the Coriolis force is negligible given the predominance of turbulent effects in the flow, thus eliminating the need to match the Rossby Number. In a boundary layer wind tunnel a neutral stratification is assumed since the temperature within the tunnel is considered constant with height. Thus, the Froude Number is matched automatically when modelling neutral stratification. This leaves the Reynolds Number as an indicator for turbulence in a flow as a key parameter in Similarity Theory.

As it is necessary to scale models in a wind tunnel it becomes increasingly difficult to match the Reynolds Number precisely. This is due to the decreasing reference length L_{ref} with smaller model scales. Townsend (1976) postulates that turbulent flows are similar if a certain Reynolds Number is surpassed. This hypothesis is known as Reynolds Number Independence.

Small eddies are predominantly influenced by viscosity. This leads to a limitation of Reynolds Number independence because viscous effects are more prevalent in the wind tunnel than in nature. This leads to a shortened energy density spectrum at the high frequency end. The larger, more powerful eddies are controlled by the size of the wind tunnel rather than the Reynolds Number. These large eddies are dominant in a boundary layer flow (Snyder, 1981). With the above limitations in mind, it is possible to model turbulent flows in a meaningful manner in a boundary layer wind tunnel.

2.2 Wind Turbines & Their Wakes

The wind has long been used as a source of energy for mankind. More recently, on the scale of the history of man, wind, through the use of wind turbines, has become a large scale source of carbon emission free electric power. Decades of research have gone into what is now a mature industry, both onshore and offshore. This section aims to give an overview of the current scientific understanding of wind turbines and, more specifically, their wake's behaviour. First the general theory and function

of a modern wind turbine will be discussed before going into the more specific case of a wind turbine's wake. Second, the current state of the art regarding the wakes of floating offshore wind turbines (FOWT) will be presented.

In this thesis two normalised quantities are of central importance to maintain comparability within this work but also between different studies. Firstly, all distances are normalised using the wind turbine's or the model's diameter D. Secondly, the height coordinate (z) is normalised around the hub height h and related to D:

$$h = (z - h) \cdot D^{-1} \tag{2.13}$$

Applying this normalisation leads to the hub height always having a coordinate of $h = 0$, while the top tip of the turbine is at $h = 0.5$ and the bottom tip as the coordinate $h = -0.5$. This area is marked grey in most figures presenting vertical profiles. Finally, the reduced frequency f_{red} is used amply. The applied motion frequency f is normalised using the reference velocity U_{ref} and D:

$$f_{red} = \frac{f \cdot U_{ref}}{D} \tag{2.14}$$

Knowledge of these normalised quantities will help when evaluating the various studies related to FOWTs that will be discussed in this chapter.

2.2.1 General Wind Turbine Theory

In order to better understand how a wake develops, it is necessary to take a brief look at the object creating the wake, a wind turbine in this case. Burton et al. (2011) give a comprehensive introduction to all aspects of wind turbine design and operation. The following section uses information presented in the Wind Energy Handbook (Burton et al., 2011). Most modern industrial scale horizontal axis wind turbines consist of a tower, a nacelle and three turbine blades. The nacelle houses the gear box, brake, generator and control elements. The blades are the principle part of the turbine, as they are forced into rotation by the lift created on their air foils by the incoming wind. Due to the projection of the lift vector into the rotation plane, the blade moves in a given direction. As the blade has a rotational velocity it experiences a velocity relative to the oncoming wind. This relative velocity changes along the span of the blade, thus dictating the skewed nature of most wind turbine blades. Each blade can be rotated around its principle axis. This operation is generally referred to as pitch control, as the pitch angle of the blade is changed. Pitch control is used to achieve a variety of optimisation and safety functions. When generating power the blades are pitched in such a manner that the optimum power output of the wind turbine can be achieved. In extreme situations the blades can be turned so that no more power is produced, for example when the wind velocity

is too high. Pitch control can also be used to influence the wind turbine in order to improve the overall power output of a wind farm (e.g. Munters and Meyers, 2018), a topic to be briefly discussed later in this section.

In most current wind turbines the rotor's shaft is connected to a gear box in order to achieve the rotational velocities necessary for the generator to produce electric power. A brake is mounted between the gear box and the generator for operational and safety reasons. Some wind turbines don't have a gear box, these are called direct transmission turbines. The power from the generator is fed to the power grid via a transformer. Figure 2.2 gives a general overview of the process described above. Not shown for reasons of simplicity are the rotational functionalities of the nacelle (or hub) as a whole. The nacelle is guided to remain in line with the oncoming wind.

Each component mentioned here has its own fields of research to further optimise wind turbines as a whole. As the main topic of this study is the wake of a wind turbine, the above mentioned fields of research will not be discussed further at this point. For a comprehensive review of many aspects of wind energy research the reader is referred to Porté-Agel et al. (2019).

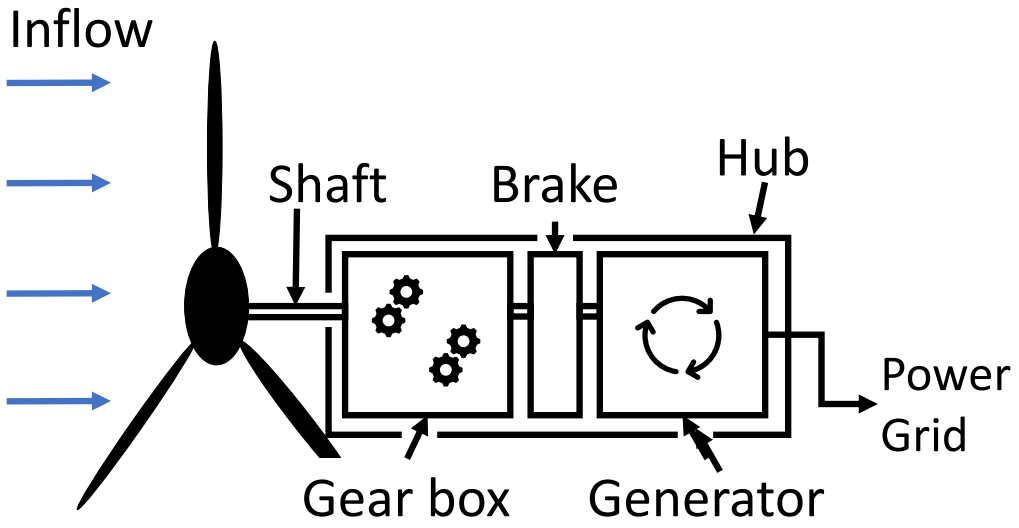

Figure 2.2 – A sketch of the power generation process in a geared wind turbine.

2.2.2 Wind Turbine Wakes

As wind turbines extract kinetic energy from the incoming flow they produce wakes. A wake is considered to be the area downstream of the turbine where the mean velocity is reduced and turbulence intensity is increased (Burton et al., 2011). The wake interacts with the ambient flow as kinetic energy is entrained and the velocity deficit in the wake is slowly reduced until the flow has completely retrieved the energy extracted by the turbine. Wind turbine wakes have been studied extensively in the past (for example: Vermeer et al., 2003; Churchfield et al., 2015; Porté-Agel et al., 2019). This section gives an overview of the current state of the research regarding general wake theory and the dependence of a wind turbine's wake on its surroundings as well as the wake's meandering characteristics.

Analytical Wake Models

Analytical models of a wind turbine's wake are usually derived using the velocity deficit. A first wake loss model was suggested by Jensen (1983). This model is also known as the top-hat model. The model is derived using momentum conservation according to the authors [1]. It describes the velocity deficit as a function of the downstream distance from the turbine as described in equation 2.15:

$$1 - \frac{u_2}{u_1} = \frac{1 - \sqrt{1 - C_t}}{(1 + k \cdot x \cdot R^{-1})^2} \tag{2.15}$$

where u_2 is the velocity at distance x, u_1 is the inflow velocity, C_t is the thrust coefficient of the turbine, k_w is the wake decay parameter and R is the rotor radius. Over time this model has proven its simplicity and is thus widely employed in areas

1. This is contested in Bastankhah and Porté-Agel (2014), who claim that Jensen (1983) in fact only applied mass conservation.

where precise knowledge of the wake deficit is not deemed necessary. The model is known to overestimate the available energy. The assumption that the velocity deficit profile is constant within the wake can not be considered realistic. The Jensen model has since served as a basis for the development of more advanced wake models such as the wake loss models suggested by Larsen (1988) and Frandsen et al. (2006).

A more realistic depiction of the wake is delivered by assuming a Gaussian distribution of the velocity deficit (Bastankhah and Porté-Agel, 2014). The model proposed by Bastankhah and Porté-Agel (2014) respects mass and momentum conservation. The model only requires the wake's growth rate as an input variable. The general form of this model is described in equation 2.16:

$$\frac{\Delta U}{U_{\text{inf}}} = \left(1 - \sqrt{1 - \frac{C_t}{8\left(k \cdot x/d_0 + 0.2\sqrt{\beta}\right)^2}}\right) \cdot \exp\left(-\frac{1}{2\left(k \cdot x/d_0 + 0.2\sqrt{\beta}\right)^2}\left(\left(\frac{z - z_h}{d_0}\right)^2 + \left(\frac{y}{d_0}^2\right)\right)\right) \tag{2.16}$$

where ΔU is the velocity deficit, U_{inf} is the inflow velocity, C_t is the thrust coefficient, x is the downstream position, d_0 is the rotor diameter, β is the wake decay parameter, z is the vertical coordinate, z_h is the hub height and y is the lateral coordinate. The Gaussian model suggested by Bastankhah and Porté-Agel (2014) delivers good agreement with LES and wind tunnel measurements used to verify the model. It is noted by Xie and Archer (2015) that the lateral and the vertical growth rates can not be considered equal when respecting atmospheric stratification. This requires the introduction of an additional vertical growth rate k_z to the model. This Gaussian model has since been used in a number of studies (e.g.: Parada et al., 2017; Stevens and Meneveau, 2017).

Latest research in wake modelling points to the development of super-Gaussian wake models as suggested by Blondel and Cathelain (2020). Their model is tested against a selection of current models (amongst them Jensen, 1983; Frandsen et al., 2006; Bastankhah and Porté-Agel, 2014) by Hegazy et al. (2021). The authors find that the super-Gaussian model proposed by Blondel and Cathelain (2020) compares best to field data opening a promising path to high fidelity wake models.

Figure 2.3 shows a comparative illustration of the different models (top-hat and Gaussian) mentioned here. A detailed review of different wake loss models was conducted by Archer et al. (2018).

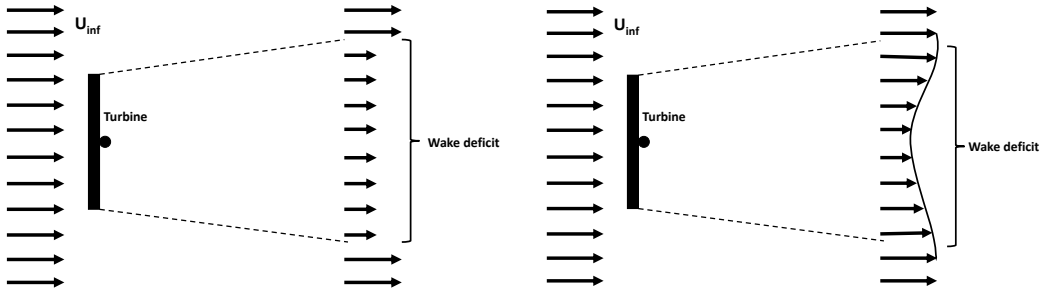

Figure 2.3 – Illustration of the Jensen (left) and Gaussian (right) wake loss models highlighting their differences.

Physical Modelling of Wind Turbine Wakes

In the past, two types of physical models have been used to imitate a horizontal axis wind turbine. These are a scaled down rotating model and an actuator disc model. Both types of models have advantages and disadvantages that must be weighed against each other, when devising a measurement campaign. Some of these advantages and disadvantages will be discussed in the following.

Rotating models have been developed at Politecnico di Milano (e.g. Bottasso et al., 2014; Campagnolo et al., 2016) and the University of Oldenburg (e.g. Berger et al., 2018) in recent years, to mention but two. These models are technologically complex and, consequently, relatively expensive. The models generally require careful scaling of the aerodynamic characteristics of the blades. In order to avoid extremer Reynolds number mismatches, and resulting highly distorted blades, few smaller models exist. At small scales it becomes increasingly difficult to maintain kinematic similarity between the original and the model, as the model must rotate faster with smaller scales.

The challenges related to scaling a wind turbine are presented and discussed in Canet et al. (2021). The authors point out that while geometric scaling is a relatively straightforward approach and delivers acceptable results, the Reynolds number mismatch between the original and the model causes the aerodynamic and load quantities of the blades to diverge. The Reynolds number mismatch is inherent to wind tunnel testing. This requires that the model blades be redesigned aerodynamically as well, in order to match the variety of values to be matched between the model and the original. Canet et al. (2021) also underline the challenges faced when looking for materials that can recreate the elasticity of the blades at scale. Generally, the aerodynamic redesign of the blades delivers good results with regard to the values to be matched, though not all values can be matched at once.

Wang et al. (2021) investigate the wake of the TUM G1 turbine compared to a numerical simulation of an equivalent full-scale turbine. The authors find that the rotating model produces highly similar near and far wakes to the numerical simulation regarding mean values such as wake deficit, turbulence and other wake shape and meandering characteristics. The spectra of the flow components are also

found to be similar (Wang et al., 2021).

In contrast to the rotating model, the porous disc model is considered to be a low-cost, easy to implement wind turbine model. This approach also makes it possible to overcome Reynolds dependence issues at small geometric scales as grid turbulence is Reynolds independent (Mohamed and Larue, 1990). The first similarity tests between a porous disc and a rotating model were carried out by Aubrun et al. (2013). In this study the actuator disc is designed to match the rotating model's thrust coefficient c_t. In their study the authors, using an atmospheric boundary layer (ABL), find that the wakes of each model are sufficiently similar at distances of $x/D > 3$. According to Aubrun et al. (2013) all significant streamwise quantities like the mean velocity deficit, the statistical quantities and the integral length scale are similar beyond $x/D > 3$. Furthermore, the rotational momentum is not measurable beyond this distance and the tip vortex signature at the edges of the wake are undetectable. These results are found to be valid for high turbulence intensity (I) ABLs ($I \approx 13\%$), and to a slightly lesser extent, for less turbulent ABLs ($I \approx 4\%$), too (Aubrun et al., 2013). Neunaber et al. (2021) extend the comparability of the actuator disc model to higher order statistics, allowing a more extensive investigation of an actuator disc's far wake.

Camp and Cal (2016) investigate the different development of physical quantities in the near wake (up to $x/D \approx 6$) of each model type. The inflow conditions are ABL-like, without mention of precise values. They point out that for distances of $x/D \leq 3.5$ the effect of rotation can clearly be measured, especially when investigating the mean and turbulent kinetic energy budgets. The turbulent kinetic energy (TKE) is significantly increased around the top tip of the rotating turbine model compared to the actuator disc. Beyond $x/D > 3.5$ the authors find few differences between the actuator disc model and the rotating model.

Lignarolo et al. (2014) analysed the physics involved that dominate the near wake instability of a rotating model. As the tip vortices become unstable and collapse, the mixing process is enhanced. This phenomenon can obviously not be observed with a porous disc, thus limiting the disc's ability to reproduce the near wake of the wind turbine correctly.

With regard to the comparison of a rotating wind turbine model and an actuator disc model it may be concluded from current literature that the wake of a porous disc is sufficiently similar in a statistical and physical way to the wake of a rotating model in an ABL flow at downstream distances of $x/D \geq 3.5$. If the aim is to study the near wake, i.e. $x/D < 3.5$, then it is necessary to use a rotating model as the turbulence induced by the rotation plays a crucial role in this part of the wake.

Dependence on Inflow Conditions

The wake of a wind turbine is strongly dependent on the inflow conditions encountered. The turbulence level and the uniformity of the inflow play a central role

in the wake's shape and downstream evolution.

In a vertically uniform flow the wake of a wind turbine is axisymmetric around the longitudinal axis (Vermeer et al., 2003). Introducing a turbulent, yet uniform flow will lead to a shortening of the wake, as the momentum entrainment from the surrounding flow is increased, while the wake remains axisymmetric (Murata et al., 2016). When adding a boundary layer flow, i.e. non-uniform inflow conditions, the wake characteristics depart from axisymmetry. This again, leads to stronger vertical gradients favouring the entrainment of momentum from the ambient flow (Lignarolo et al., 2014). The wake is thus dependent on many of the same values that are widely used to characterise a boundary layer flow's turbulence, such as the roughness length (z_0) or the Reynolds number (Re).

The wake is, in fact, dependent on the surface roughness z_0, as demonstrated by Chamorro and Porté-Agel (2009). Generally, rougher surfaces will lead to higher turbulence in the inflow, thus decreasing the velocity deficit and accelerating the wake recovery. The explanation for the enhanced recovery is the increased in departure from symmetry in the velocity and turbulence intensity profiles in the inflow and the resulting higher vertical gradients, leading to more shear and enhanced energy entrainment, compared to a smooth surface (Chamorro and Porté-Agel, 2009). The elevated levels of ambient turbulence further favour energy entrainment. Chamorro and Porté-Agel (2009) point out that the velocity deficit remains nearly axisymmetric despite the non-axisymmetric nature of the velocity distribution.

Chamorro et al. (2012) investigates the effect of the Reynolds number on the wake's mean velocity and higher order statistics. They find that mean quantities achieve Re independence at lower velocities than the higher order statistics. Chamorro and Porté-Agel (2009) also find that Re independence is dependent on the downstream distance of the wake. The far wake appears to be less sensitive to Re than the near wake. This is significant as the inflow velocity, the main driver for Re, when using a rotating turbine model, may need to be changed depending on the values and regions of interest in a given study.

As the integral length scale L_u^x describes the most energetic eddies in a boundary layer flow, it also affects the large scale behaviour of a wind turbine's wake, i.e. meandering. Meandering, so the random lateral and vertical instantaneous displacement of the overall wake, is an important characteristic of any wake. Larsen et al. (2008) state that all atmospheric turbulent eddies larger than twice the wind turbine's diameter will induce meandering. Smaller eddies will contribute to turbulent diffusion. Expanding on this, Espana et al. (2012) study the effects of large eddies on the wake of a model wind turbine. A porous disc model is employed. The authors do not observe any wake meandering when L_u^x is smaller than the disc diameter, yet they do when the largest eddies are significantly larger than the model's diameter (Espana et al., 2012). This observation proves the importance of the ratio of L_u^x to the turbine's diameter, when modelling a wind turbine's wake.

The stratification of the flow, i.e. the thermal structure of the boundary layer,

also plays a role in the development of a wind turbine's wake (Abkar and Porté-Agel, 2015). As stratification is difficult to model in a physically correct fashion in a wind tunnel, most studies rely on numerical simulations (Chamorro and Porté-Agel, 2010). Different stratification conditions result in varying wake lengths. Unstable conditions result in faster wake recovery and increased wake meandering, as these conditions favour mixing processes. Neutral and stable stratification lead to slower wake recovery and less meandering. The authors attribute this to reduced turbulence levels in the inflow under these stratification conditions. In their numerical study, Abkar and Porté-Agel (2015) find that stratification also affects the energy balance in the wake

As this section has shown, a wind turbine's wake is strongly dependent on the inflow conditions. Surface roughness, turbulence levels and scales, flow uniformity and, the vertical thermal composition of the flow, play important roles in a wind turbine's wake development. The second relevant characteristic, apart from the velocity deficit, for large scale wind energy applications is wake meandering because it impacts directly on power production and fatigue loads on downstream turbines. Thus wake meandering has been the subject of further research, as presented in the following section.

Wake Meandering & Optimisation

A wind turbine's wake is strongly influenced by the upstream flow and surface conditions that lead to wake meandering in real-life conditions (Espana et al., 2011). A number of studies have investigated the characteristics of wake meandering in more detail. In the following a selection of these studies will be discussed.

Espana et al. (2011) investigate the spatial distribution of the wake meandering. They find that lateral meandering is larger than vertical meandering by a ratio of $\sigma_v/\sigma_w \approx 1.3$ in atmospheric flow conditions. The authors also note that turbulent diffusion has negligible effects on the wake. They attribute this observation to the turbulence scales involved. These length scales are smaller than the wake width and thus less energetic.

In their experimental investigation of the near wake Howard et al. (2015) use PIV to study a variety of near wake characteristics. The authors point out that the wake expansion angle can vary, is not necessarily symmetric and depends on the turbine's operational regime. They further deduce the wavelength of the meandering process which is found to be around $1\,D \pm 0.2\,D$, depending on the operational regime of the turbine model. The meander wavelength and amplitude fall into two characteristic groups. The first is influenced by hub vortices for $x/D < 2$ and is dominated by higher frequencies and smaller amplitudes. The second group is characterised by lower frequencies and larger amplitudes that characterise wake meandering for $x/D > 2$.

Field data has been acquired using LiDAR to verify the numerous numerical

and wind tunnel studies investigating a wind turbine's wake (Garcia et al., 2019). The authors find the measured mean flow and turbulent values, as well as wake meandering characteristics, to be in line with other literature. An unexplained deviation from the expected behaviour is the asymmetric distribution of the turbulence intensity.

With a greater understanding of the quantities governing the wake and certain behavioural characteristics of the wake it is possible to predict wake meandering. An early stochastic model is suggested by Larsen et al. (2007) with their Dynamic Wake Meandering (DWM) model. Building on the DWM model, Muller et al. (2015) propose a predictive model. The authors suggest using the lateral loads encountered by the rotor to predict the position of the wake in real-time. The lateral loads show the highest correlation with instantaneous wake position, especially when considering the presence of an upstream turbine. Muller et al. (2015) argue that the lateral loads are a spatially averaged quantity impacting the rotor, leading to a correlation with the wake position.

On the basis of our current understanding of wakes it is possible to imagine that a wake might, to some meaningful degree, be controllable. Together with wake prediction methods, wake steering can be used to optimise a wind park's power output by minimising losses in power production due to the presence of turbine wakes. Wake steering is achieved through wind turbine control mechanisms (as mentioned in section 2.2.1). In the context of a wind farm the wake can be steered away from the downstream turbine by yawing the upstream turbine (e.g. Bastankhah and Porté-Agel, 2016). This operation can lead to overall increased power output of a given wind farm.

Looking into more advanced control and optimisation strategies is a further field of research, mostly in the numerical domain. Yılmaz and Meyers (2018) impose a periodic oscillation at a reduced frequency of $f_{red} = 0.38$ on the blades of the NREL 5MW turbine. In realistic inflow conditions the overall power output is increased by up to 9.7% (Yılmaz and Meyers, 2018). The authors observe that a large vortex ring develops periodically behind the first turbine. This vortex ring increases the entrainment of energy from the free stream to the wake, thus increasing the overall energy available. Building on this, Munters and Meyers (2018) found that the optimal control frequency is $f_{red} = 0.25$. A combined numerical and experimental study carried out at Politecnico de Milano also indicates the optimal frequency to be in the range of $f_{red} = 0.3$ (Frederik et al., 2020).

The current scientific understanding of a wind turbine's wake can be described as comprehensive. Different factors affecting the wake's development and its behaviour have been extensively studied. The effects of the inflow conditions as well as the central effects governing the turbine's wake are understood. Ways of using the interactions between a turbine and its wake are being studied to optimise wind farm power production. But, so far all the above mentioned studies have only dealt with fixed turbines, either onshore or offshore. The following section will present

the general ideas behind floating turbines and discuss the current state of the art regarding the wake of FOWTs.

2.3 Floating Offshore Wind Turbines

Floating offshore wind turbines (FOWT) pose new questions regarding the turbine's wake. The main question is to what extent induced motion on the turbine leads to modifications of the wake. As there are currently only a very limited number of FOWTs installed around the world and due to the hostility of their environments there is currently no field data available. Therefore all studies to date deal with either numerically or physically modelled data. This section will first present the historical context of FOWTs. Then an overview of current literature on FOWT wakes will be given, followed by a brief presentation of possible control operations for FOWTs. Finally, a brief discussion of the present literature is presented.

Historical Context

Professer William E. Heronemus of the University of Massachusetts Amherst was the first to propose the concept of commercial FOWTs in 1972 (Heronemus, 1972). The concept was not followed up on for several decades. First studies regarding the general feasibility of FOWTs were published early in the 2000s (Musial et al., 2004; Sclavounos, 2008, for example). The authors focus on the general business case of FOWTs and present different floaters that might be used. Figure 2.4 shows these principal floater types. These are the spar buoy (ballast stabilised, left hand tile), the barge and the semi-submersible (both buoyancy stabilised, middle tile), and the tension-leg platform (mooring line stabilised, right hand tile). Each floater has their own characteristic motion frequency range, as indicated by the grey bar in figure 2.4. These different types of floaters have been employed reliably in the oil and gas industry for decades and are thus a low risk approach for the development of FOWTs. However, many technical challenges remained (and still remain) to be overcome.

Butterfield et al. (2007) formulated challenges facing FOWTs which include mooring technology, turbine control, generator fatigue as well as the development of an analytical tool to simulate an FOWT. As this thesis focuses on the characterisation of the wake of an FOWT, the above mentioned engineering aspects will not be discussed here. The focus will be on wake development and meandering. Fatigue loads and overall energy production will be presented in a limited fashion given their close relationship with flow characteristics. Figure 2.5 shows the definition of each Degree of Freedom (Dof). The longitudinal, lateral and vertical translations are referred to as surge (D_x), sway (D_y) and heave (D_z). The rotational motion around the longitudinal axis is referred to as roll (R_x), motion around the lateral axis as pitch (R_y). Yaw refers to the rotational movement around the vertical axis (R_z).

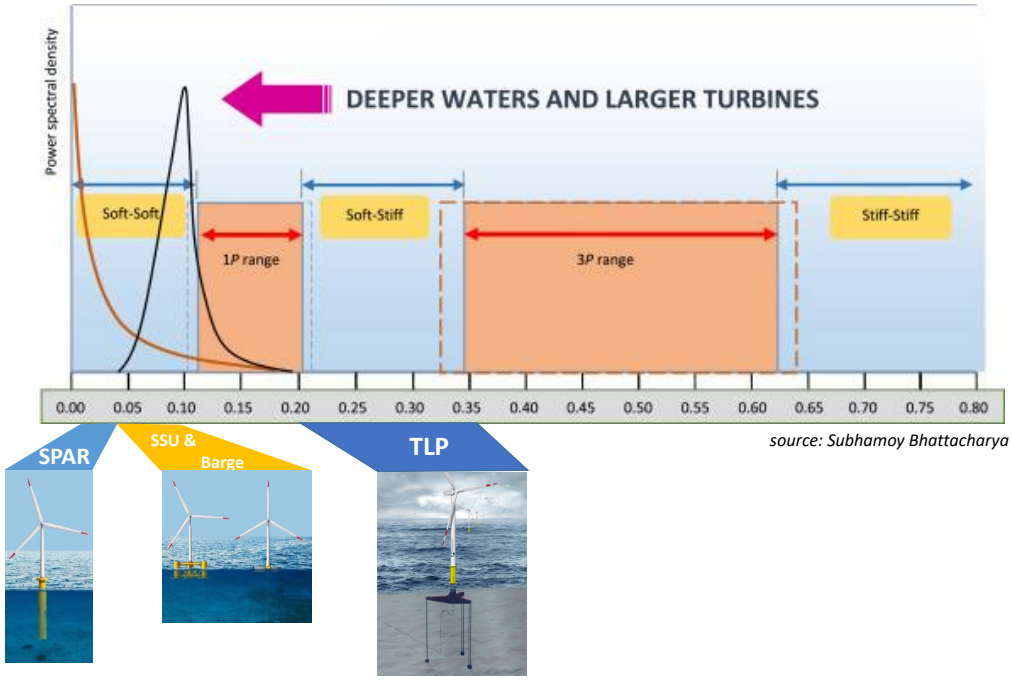

Figure 2.4 – The different types of floaters used for FOWTs and their corresponding characteristic frequencies. Used with permission from Jean-Christophe Gilloteaux.

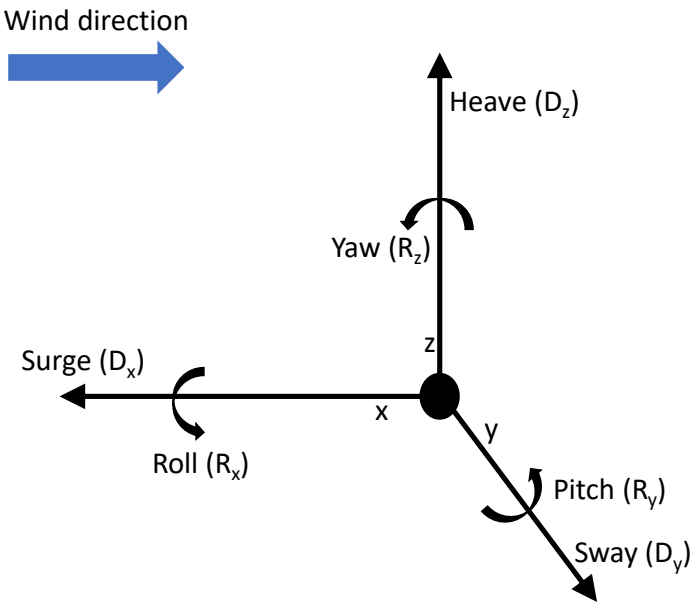

Figure 2.5 – Sketch of Degrees of Freedom (Dof) as used in this thesis. Longitudinal (x-axis), lateral (y-axis) and vertical (z-axis) translations are referred to as surge (D_x), sway (D_y) and heave (D_z). The rotations around the longitudinal, lateral and vertical axis are referred to as roll (R_x), pitch (R_y) and yaw (R_z).

FOWT's Wakes

The need for a dedicated numerical wake model adapted to an FOWT was first formulated by Sebastian and Lackner (2012a). The authors identify the need for more rigorous modelling as the highly unsteady aerodynamic load conditions that are linked to the platform's motions, could not be accurately captured by momentum balance approaches. In a later publication the authors present a free vortex method (FVM) to calculate the wake of an FOWT (Sebastian and Lackner, 2012b). The FVM model proposed by the authors is in agreement with experimental data. As the authors focus on a good balance between computational cost and precision the FVM presented in Sebastian and Lackner (2012b) has since evolved into a widely cited study when numerically investigating wakes of FOWTs (e.g.: Tran and Kim, 2015; Liu et al., 2017).

Early experimental work was carried out by Rockel et al. (2014). To simulate the pitch motion of their turbine model the authors use a gimbal support, that allows pitching motion with an amplitude A and a reduced frequency f_{red} (A=16°-19°, $f_{red} = 0.05 - 0.07$). The free motion regime of the turbine model is thus dependent on the inflow conditions rather than the sea conditions. The authors employ stereoscopic particle image velocimetry (sPIV) to measure the flow velocity in the wake of the model turbine. Rockel et al. (2014) find that the wake recovery process is slowed down by pitch motion, their explanation being reduced downwards momentum transport from the flow above the wake. This, in turn, is caused by the turbine's reduced drag due to its ability to oscillate with the flow.

In a later experimental study Hu et al. (2015) observe reduced shear stress in the wake of an FOWT model subjected to imposed surge motion (A=0.133 D, $f_{red} = 0.18\,Hz$ [2]) compared to a fixed model. This implies that the wake will recover more slowly requiring larger distances between FOWTs. At the same time energy production of the turbine is increased by 1% (Hu et al., 2015).

Fu et al. (2019) investigate the effects of roll and pitch motion on an FOWT's wake and power production. The emulated motion has amplitudes between 5°and 20°with motion frequencies up to $f_{red} = 0.02$. Only the results for A=20°and $f_{red} = 0.02$ are presented as this motion regime shows the clearest results. The authors use PIV measurements to visualise the flow field at a selection of distances downstream. Inflow conditions represent a turbulent boundary layer with a rotating turbine model placed within it (Fu et al., 2019). The roll and pitch motions have clear signatures in the wake and power production fluctuations. With regard to the wake the authors point out that the motions investigated lead to increased turbulent kinetic energy (TKE) in the wake, likely leading to enhanced wake recovery but also higher load on any downstream turbines. Fu et al. (2019) state that at $x/D \approx 7$ the differences between the wake of a fixed turbine and an FOWT become minimal.

Lee and Lee (2019) conducted a numerical study investigating the near and

2. A value of U_{ref} is not given in Hu et al. (2015)

medium (or intermediate) wake regions of FOWTs using three different floaters (the ITI Energy barge, the OC3-Hywind spar-buoy and the MIT/NREL TLP) as well as their respective thrust and energy output. The NREL 5 MW turbine is placed on top of the respective floater. The authors use advanced nonlinear numerical methods (nonlinear vortex lattice combined with a vortex particle method) to simulate the wake. The aim of the study is to characterise the effects of each Dof separately. The authors conclude that streamwise motion, i.e. pitch and surge, dominate the thrust force and power output of an FOWT independently of the floater used. Lee and Lee (2019) also found that the oscillation frequencies in the thrust force and power output resemble those of the platform motion. Regarding the wake it was found that any induced motion leads to wake instability due to the development of unstable wake vortices (Lee and Lee, 2019). Further, the authors found the barge floater used in their study incurred the strongest platform motions, thus affecting the wake more than other floaters. The motion frequencies used in the study by Lee and Lee (2019) can be considered realistic. The authors investigate the floater's response for one set of sea conditions. The inflow is a shear-free uniform flow, as referenced in Sebastian and Lackner (2012a).

A comprehensive numerical study of the wake of an FOWT was recently carried out by Kopperstad et al. (2020). Employing Large Eddy Simulation (LES) and an actuator disc model (ADM), the authors analyse the development of the wake and the power extraction of a spar buoy and a barge platform. The numerical results are validated against wind tunnel data. Further they study the respective wakes in a laminar and slightly turbulent flow. Three sea conditions are employed to understand the dependence of the wake development on the given sea state. The authors find that there are significant differences in the wakes of an FOWT mounted on a spar buoy or on a barge platform in turbulent flow conditions. Though both platforms show accelerated wake recovery, the barge mounted FOWT shows faster recovery. This is attributed to the floater's motion being close to the natural frequencies of the wake, thus leading to greater instabilities in the wake's shear layer, which in turn lead to accelerated mixing and consequently faster wake recovery (Kopperstad et al., 2020).

So far only Rockel et al. (2016) studied the effects of the incoming wake of an FOWT on downstream FOWT. The experimental set-up is the same as presented in Rockel et al. (2014). The authors find that the oscillation of the downstream turbine is reduced compared to the upstream turbine. Rockel et al. (2016) attribute this to the reduced mean velocity and turbulent stresses in the far wake of the upstream turbine. As mentioned earlier, in this set-up, the turbine model is allowed to oscillate freely in the inflow.

Apart from the above mentioned study a more extensive study by Wise and Bachynski (2020) investigates the effects of wake meandering FOWTs. In order to test possible differences in behaviour between platform types, the authors, in their numerical simulations, employ a variety of different floating platforms. Wise and

Bachynski (2020) find that lateral wake meandering excites platform yaw motion on downstream FOWTs. Depending on the type of floater the standard variation increases between 20% and 40% (Wise and Bachynski, 2020). The authors note that pitch and surge motion are not affected by lateral wake meandering. With regard to fatigue Wise and Bachynski (2020) conclude that oscillations in the range of the turbine's resonance frequency are key to determining fatigue loads, not effects of wake meandering, as is the case for fixed turbines.

In a publication currently under review Li et al. (2021) investigate the onset of wake meandering when the turbine is subjected to sway and roll motion. The numerical study is set up using an actuator surface, similar to an actuator disc, to model the wind turbine. An LES model is employed to simulate the flow. The inflow is characterised as a uniform low turbulence and shear-free flow. Linear stability analysis (LSA) reveals the most unstable frequencies to be in the range of $f_{red} = 0.1$ to $f_{red} = 0.8$. The authors find that lateral motion of the FOWT can trigger wake meandering. They attribute this to the overlap between the wake's unstable frequencies and the floater's natural frequencies. Li et al. (2021) state that the wake recovery is increased, while mechanical loads on downstream FOWTs are also increased.

A recent study by Fontanella et al. (2021) employed PIV and hot-wire anemometry to investigate the near wake of a rotating wind turbine model in a low turbulent and uniform inflow. The authors conclude that there is a clear signature of the motion frequency in the power spectrum of the wake when the model is subjected to surge motion. The clearest response can be found at the lateral edges of the wake. Further, Fontanella et al. (2021) find that the mean values of the flow are only marginally affected by surge motion. The imposed surge motion adds energy to the wake. These results appear to contradict the results by Rockel et al. (2014).

Control & Optimisation

Rodrigues et al. (2015) suggest taking advantage of a floater's ability to move on the sea's surface to dynamically adjust an FOWT park. The aim is to optimise a farm's power output. The approach is twofold: the turbine's location within the park are optimised and each turbine's position is optimised relative to the wind direction. This is done in order to reduce power losses due to wake effects on downstream turbines. The authors find that the park's overall power output can be increased by up to 4.4% using the proposed control method. In this context Rodrigues et al. (2015) also state the importance of having accurate (and fast) wake models.

Wang et al. (2018) study the wake of two connected modelled FOWTs in a hardware-in-the-loop approach. The aim of the study is to present a closed loop controller to maintain a constant power output. The $1.1\,m$ diameter models are placed in a turbulent boundary layer flow. The experimental data is used to validate the LES model developed in the scope of the study. Wang et al. (2018) find that

the LES model reproduces the validation data to a satisfactory point. The control software developed compensates the periodic platform motion well in both the LES simulation and the wind tunnel test. The authors thus demonstrate that sophisticated turbine control on an FOWT is possible, allowing the turbine to maintain a constant power output.

Concluding Remarks

It can be concluded that previous work on FOWT's wakes can be classified into two opposing groups. The first group (Rockel et al. (2014) and Hu et al. (2015)) state that wakes would replenish slower due to decreased shear. The second group (Fu et al., 2019; Kopperstad et al., 2020; Fontanella et al., 2021) find that the wake recovery is enhanced. Fu et al. (2019) and Kopperstad et al. (2020) argue that this is due to increased shear production in the wake of an FOWT, thus contradicting the first group. This may be due to a number of fundamental differences between the studies. The most notable difference is whether, or not, the motion of the model is induced by the flow or externally. This alone will result in very different motion regimes as the characteristic lengths and times are very different between the air and water. Another important difference is the variation of inflow conditions, as these significantly affect the wake (see section 2.2.2). A brief summary of the varying test conditions used in the literature presented here is shown in table 2.1. It should be pointed out that pitch motion greater than 10° appears to be well outside the operational boundaries of any current FOWT design. Since the other motion regimes are more or less realistic, a faster wake recovery might be observed in an operational array of FOWTs depending on the met-ocean conditions. Regarding the unsteady behaviour of the wake, Fontanella et al. (2021) find that the motion frequency can be identified in the power spectrum of the wake.

With these two sets of observations prevalent in the literature, more research is necessary with conditions as close as possible to those encountered by a real FOWT to determine which case is more likely to be encountered. Both trains of thought have positive and negative implications on the overall performance of an FOWT array or park. Either the mean flow velocity and the turbulent quantities in the wake of an FOWT are increased, thus increasing energy production and fatigue at the same time, but allowing for a tighter packing of the given area. Or the opposite could be the case, i.e. slower wake recovery, reduced turbulence, thus less fatigue, but also a less densely packed FOWT farm area. The main research questions resulting from the current state of the art regarding FOWT wakes are presented and discussed in section 2.4.

Table 2.1 – Summary of the literature presented in this section. The reduced frequencies, normalised amplitude, the inflow conditions used and the Dofs investigated in the respective studies are summarised. The reduced frequency is calculated using the rotor diameter and the reference wind velocity. The amplitude is normalised using the rotor's diameter, except for pitch.

Publication	f_{red}	**Amplitude**	**Inflow**	**Dof**
Rockel et al. (2014)	0.05-0.07	16°-19°	ABL	R_y
Hu et al. (2015)	0.18Hz	0.133 D	ABL	D_x
Lee and Lee (2019)	0.2-0.8	0.07 D/6°	shear-free	all
Fu et al. (2019)	0.02	20°	TBL	R_x, R_y
Kadum et al. (2019)	0.04-0.05	15°	shear-free	R_y
Kopperstad et al. (2020)	0.31-1.15	0.03 D/0.9°	lam./turb.	D_x, R_y
Wise and Bachynski (2020)	0.1 - 0.2	no mention	TBL	D_x, D_z, R_y, R_z
Fontanella et al. (2021)	0.07-0.8	0.008-0.125	low. turb.	D_x
Li et al. (2021)	0.1-1	0.04/2.88°	uniform	D_y, R_x

2.4 Research Questions

This section identifies the two central research questions, as well as the reasoning behind them, to be addressed in this thesis. Each question will have its own subdivision. The central research questions are subdivided into more explicit sub-questions for improved clarity.

While knowledge of the wake of fixed-bottom or land-based wind turbines is very useful as a reference case for this thesis, not all conclusions may hold true for the case of FOWTs due to the imposed motion and resulting effects of entrainment on the wake. To date there is limited literature on the topic of FOWT wake development and meandering (e.g.: Rockel et al., 2014; Kopperstad et al., 2020). Most studies regarding FOWTs focus on aerodynamic and mechanical loads (for example Sebastian and Lackner, 2013) or the near wake (Wang et al., 2018). There is thus a gap in the understanding of the far wake of FOWTs. Further, most studies to date use either idealised inflow conditions (Lee and Lee, 2019) or large motion frequencies and amplitudes, that do not necessarily represent those of an FOWT (Rockel et al., 2014). Consequently there is limited data against which to verify wake models. This thesis seeks to provide evidence and data that will help to further understand the implications of the motion of each FOWT for the wake, and thereby contribute to the development of reliable wake models. The first research question is:

How does turbine motion affect the development of the wake?

The aim of this question is to identify differences, or the lack thereof, in mean and turbulent quantities in the wake of a modelled FOWT with imposed motion. The vertical profiles and the downstream development of mean and turbulent quantities

are of particular interest in this context. The resulting sub-questions are:

— How are mean and turbulent quantities affected by imposed motion?
— Are there differences when compared to a stationary model?
— Are the results dependent on the motion's frequency and amplitude?
— What are the physical explanations for any potential differences?

Answering these questions will enable the further development of modified wake models for FOWTs. The physical processes affected by imposed motion can be identified, leading to an overall better understanding of the wake of an FOWT. Further, the question of wake lengthening (Rockel et al., 2014) or shortening (Kopperstad et al., 2020) might be answered.

It is not enough to solely investigate the mean and turbulent quantities, as wind turbine wakes also show unsteady behaviour in reality. It is therefore also necessary to study the wake's spectral content. Hence the second research question:

Is there an identifiable spectral signature of the turbine's motion on the wake?

The question of the unsteady behaviour of the wake of an FOWT is nearly nonexistent in the current literature. The question is of utmost importance for the modelling of the flow field encountered by a downstream FOWT, since the inflow conditions affect power production and fatigue loads. In order to correctly project the costs of operating an FOWT park it is thus necessary to gain more knowledge on the effects of motion on the unsteady behaviour of an FOWT's wake. The sub-questions in this case are:

— How does the unsteady response of the wake develop laterally?
— Are all flow components affected equally by the imposed motion?
— Is the wake's unsteady response dependent on the motion's frequency and amplitude?

Responding to the sub-questions above will allow modellers to more accurately model the turbulent content of incoming flow fields, thereby improving load and fatigue calculations on FOWTs. The data can also be used in future work when studying, in more detail, the unsteady behaviour of the wake in more detail. Such studies may involve intermittency analyses and other advanced times series analysis techniques.

In order to answer these questions wind tunnel experiments are carried out. A maritime atmospheric boundary layer is modelled at the Centrale Nantes atmospheric wind tunnel facility. Different measurement technologies are employed to address the varying sub-questions, as no single measurement technology can deliver the wide range of data required. The model is subjected to varying degrees of one and three dimensional motion, using a bespoke motion system.

Chapter 3

Methodology

In this chapter the measurement concept devised to characterise the far wake of an FOWT in a wind tunnel is outlined. First the measurement concept is presented. Insight into the different technologies used to acquire the data necessary for the different parts of the investigation is provided. This part includes the development and capabilities of the different motion systems used in the scope of this thesis. The quality checks imposed upon the boundary layer flow as well as the measured data are also discussed. Finally, the test set-ups and the corresponding measurement plans are detailed.

3.1 Measurement Concept

3.1.1 Scaling

The principal factors driving the choice of scaling factors are the size and power of the wind tunnel. In order to understand the limitations imposed by the wind tunnel, it will be described in the following. Then the scaling factors will be derived.

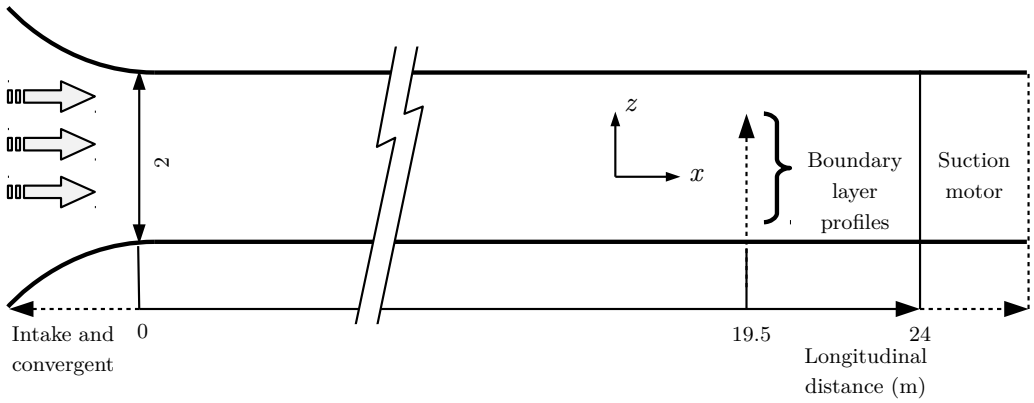

Figure 3.1 – Sketch of the wind tunnel facility at LHEEA/Centrale Nantes. All measurements in m. Based on a sketch provided by L. Perret.

The atmospheric wind tunnel at LHEEA/Centrale Nantes has a length of $24\,m$ and a cross-section of $2\,m \times 2\,m$. An intake with a settling chamber, a honey-comb

web and a convergent are situated at the front of the wind tunnel facility. The test section is located about $19\,m$ from the intake, allowing for a long area of natural boundary layer growth. A motor drives a bucket rotor at the suction end of the tunnel. The wind tunnel can achieve free stream velocities of up to $10\,ms^{-1}$. Figure 3.1 shows a schematic of the wind tunnel facility at LHEEA.

It is necessary to avoid any blocking effects in the wind tunnel, as the blockage can lead to unwanted speed-up effects in the flow around the model, thus falsifying the results. According to VDI guideline 3783 (VDI, 2000) a model may not block more than 5% of the wind tunnel's cross-section. A maximum area of $0.2\,m^2$ can thus be blocked by the model. This results in a diameter of $0.5\,m$ for the model. Given FLOATGEN's the full-scale rotor diameter of $80\,m$, this results in a maximum length scale of $\Lambda_L = 160$. The boundary layer is expected to have a maximum height of around $0.6\,m$. In order to properly replicate the interaction between the turbine model and the boundary layer, the model must be immersed entirely in the boundary layer at all times. Thus the scaling factor must be reduced further. Assuming a natural boundary layer height of $300\,m$ and considering FLOATGEN's height of $100\,m$, the FOWT covers the bottom third of the boundary layer. Applying the same ratio to the expected BL height in the wind tunnel, a maximum height of the model in the range of $0.2\,m$ to $0.25\,m$ is necessary. This results in a geometric scaling factor of about $\Lambda_L = 400$. The corresponding diameter of the turbine model is thus $200\,mm$ with a blockage factor of around 0.75%, therefore safely within the VDI's criteria.

Field data measured at Cardinaux lighthouse near FLOATGEN's location shows the average wind velocity at hub height ($\approx 60\,m$ full scale or $150\,mm$ model scale) to be around $8.6\,ms^{-1}$. The wind tunnel is not capable of reproducing this speed at the desired height, thus a velocity scaling factor of $\Lambda_v = 2$ is applied. This means that the target velocity in the wind tunnel at $150\,mm$ height is $4.3\,ms^{-1}$, thus allowing for the highest velocity, while not imposing additional constraints on the design of the motion system.

According to Strouhal similarity theory, the following is valid to retain unsteady aerodynamic similarity between flows:

$$S_t = \frac{L_{model}}{t_{model} \times U_{model}} = \frac{L_{full\,scale}}{t_{full\,scale} \times U_{full\,scale}} \tag{3.1}$$

From the scaling factors mentioned above, the time scaling factor can be derived as follows:

$$\Lambda_t = \frac{\Lambda_L}{\Lambda_v} = 200 \tag{3.2}$$

A time scaling factor of 200 implies that all processes in the wind tunnel flow happen 200 times faster than at full scale. This has serious implications for the motion system as it must be capable of reproducing high frequency motions.

After developing the boundary layer in the wind tunnel a geometric scaling factor of $\Lambda_L = 500$ and a velocity scaling factor of $\Lambda_v = 2.5$ were chosen. This allows $\Lambda_t = 200$ to remain unchanged, thus not imposing new constraints on the motion system. These modifications were necessary because it became clear during the development of the boundary layer that is was not possible to increase the integral length scale sufficiently at a geometric scale of $\Lambda_L = 400$ (see section 3.3.1 for more information). This leads to a model diameter of $D = 160\,mm$, a nacelle height of $h_{hub} = 120\,mm$ and a target velocity of $3.4\,ms^{-1}$ at hub height. All other scaling factors can be derived from the three factors mentioned above (see table 3.1). With the scaling factors determined, the technical capabilities of the motion system can be defined. The measurement technology is chosen accordingly.

Table 3.1 – Table of all relevant scaling factors used in the scope of this study.

Scaling factor	**Value**
Geometric	$\Lambda_L = 500$
Velocity	$\Lambda_v = 2.5$
Time	$\Lambda_t = 200$
Frequency	$\Lambda_f = 0.005$
Angular acceleration	$\Lambda_{aa} = 2.5 \cdot 10^{-5}$
Acceleration	$\Lambda_a = 0.0125$
Force	$\Lambda_F = 1562500$
Mass	$\Lambda_M = 125000000$

3.1.2 Designing The Motion System

A significant portion of the ground work with regard to the motion system was conducted by G. Tarpin (Tarpin, 2018). In his internship report he describes the steps taken to model the floater's motion, the necessary scaling factors, and some of the complexities regarding the implementation of the motion system.

The geometric scaling factor is set to $\Lambda_L = 500$, the velocity scaling factor is $\Lambda_v = 2.5$ and the resulting time scaling factor is $\Lambda_t = 200$. The desired technical capabilities of the motion system are prescribed by FLOATGEN's operational boundaries and the expected sea states in the area where FLOATGEN is located. Figure 3.2 shows these boundaries as a function of wind speed imposed on a probability plot of a wave-height/wave-period chart. The data is measured at FLOATGEN's

location on the test site. The red dashed line indicates the operational boundaries of FLOATGEN. The red diamonds show a variety of different sea states that are of interest in the design process of the motion system. Low and high wave-height cases are selected to define the upper and lower operating boundaries ideally required to properly model FLOATGEN's motion. Analysing each degree of freedom and its contribution to the overall movement of FLOATGEN, Tarpin finds that surge, heave and pitch are the relevant degrees of liberty to be modelled. This reduces the complexity of the motion system significantly. The reference sea state is defined as $H_s = 4.6\,m$ and $t_p = 11\,s$. These conditions represent rough seas at the test site near FLOATGEN's operational boundary. This case is selected for dimensioning the motion system as it induces the largest motions at frequencies that can be safely modelled at scale.

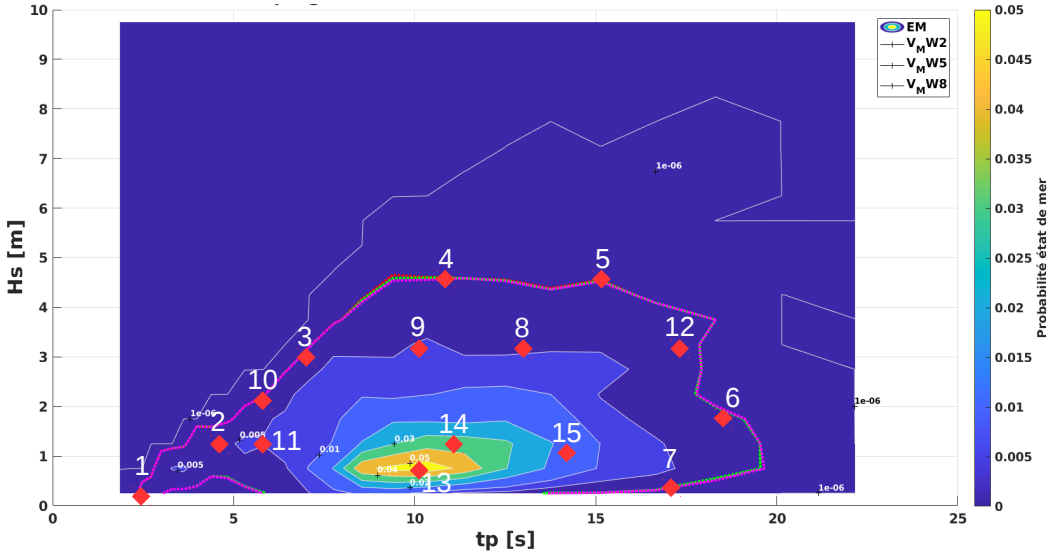

Figure 3.2 – Probability chart of sea states at the SEM-REV test site. tp is the characteristic wave period, Hs is the characteristic wave height. Together tp and Hs describe a sea state. The colorbar shows the probability of a given sea state. The red dotted line marks the operating bounds of the wind turbine as a function of wind speed. As certain wind speeds correspond to a certain sea state the wind speed is used as a boundary to identify sea states of interest. The red dots mark sea states of preliminary interest. Based on an image from Tarpin (2018).

Using the scaling factors shown in table 3.1 and the numerically simulated platform motion data provided by BW Ideol for the given sea state, a characteristic amplitude and frequency are calculated for each degree of freedom. The resulting values are shown in table 3.2. As a reminder of the definition of the Dof's orientation the reader is referred to figure 2.5 in the previous chapter.

The main challenge arises when the modelled motion time-series are scaled down to the required size. First order motion frequencies quickly reach several hundred Hz while distances travelled are in the sub-millimetre range. The low-frequency motion components govern the maximum distances travelled. These are several centimetres

Table 3.2 – Table showing the demanded maximum values of distance, velocity and acceleration calculated that the 3D motion system should be able to achieve.

Dof	**Distance**	**Velocity**	**Acceleration**
$\underline{D_x}$	50 $[mm]$	6 $[m/s]$	9 $[m/s^2]$
$\underline{D_y}$	50 $[mm]$	6 $[m/s]$	9 $[m/s^2]$
$\underline{D_z}$	8 $[mm]$	5 $[m/s]$	8 $[m/s^2]$
$\underline{R_x}$	10 $[mm]$	1000 $[m/s]$	95000 $[m/s^2]$
$\underline{R_y}$	10 $[°]$	1000 $[°/s]$	95000 $[°/s^2]$
$\underline{R_z}$	180 $[mm]$	50 $[m/s]$	800 $[m/s^2]$

at frequencies of a few Hz. The order of magnitude of this characteristic motion requires high precision components that can reliably operate at high and controlled frequencies over different length scales. Several different designs were considered over time, from electric motors to camshaft-driven movements but discarded either due to lack of precision or due to control issues.

To create a system capable of achieving the desired motions, a design using linear motors is developed. Each motor operates as one axis of one degree of freedom. These magnetically controlled motors allow short distances to be travelled at high frequencies and with high precision. As an option these motors can be controlled using LabView, thus allowing integration into the existing control software infrastructure. Further, the software allows personalised time-series to be imported, which makes the system very versatile with regard to modelling the motion of other floater types.

As the linear motors create magnetic fields, the motors must be shielded from their surroundings. The magnetic fields may pose a non-negligible, but controllable risk for the measurement technology. It is currently thought that a system capable of modelling all the motions as required in the scope of this thesis, would be one of very few such systems in use anywhere. Section 3.1.2 will give a more detailed and technical description of the two motion systems used in this study.

It is now necessary to take a closer look at the equipment used to measure the data required. The actuator disc, the acquisition technology and the motions systems are described in the following section. Also the steps taken to achieve the best quality data possible are presented.

3.2 Measurement Technology

3.2.1 The Motion Systems

In the following section the technical aspects of the two motions systems used in this study are presented. As described in section 3.1.2, some technical challenges

are present such as the high frequency and short range motions. First the 1 degree of freedom (Dof) system is presented, followed by the 3 Dof system.

1 Dof Motion System

First a 1 Dof motion system is installed. A linear motor (LinMot P01-23x160H-HP) capable of moving the additional mass of the model and the connecting piece at the desired frequencies and accelerations is installed. A linear motor consists of a stator and a rotor. The magnetic fields generated by the current applied to the magnets in the stator control the rotor with its static magnets. It is thus possible to apply high frequency and high precision linear motion on the rotor.

A series of tests are carried out to test the linear motor's usefulness given the aims of this thesis. The impact of the magnetic field is investigated by running the linear motor and acquiring data at the same time, while not running the wind tunnel. If there were to be interference from the linear motor's magnetic field it would be visible in the spectrum of the acquired data. No interference has been be detected. Another test is carried out to check for the effects of vibrations on the measurement technology. Here, the model wind turbine is replaced by an equivalent weight and the hole in the wind tunnel floor is sealed. The linear motor is operated at a given motion frequency, while the wind tunnel is running. Then the measurement is repeated with the linear motor off. The spectra of the two measurements are compared. The vibrations have no effect on the measurement equipment, if the spectra of the measurement with motion does not show any additional peaks compared to the spectra of the reference case. No effects of vibrations can be found for the first campaign. Tests with the motion system confirmed the linear motor's sufficient capabilities regarding the desired motion regimes, but showed a constant offset of the real position of the model to the commanded position of $1\,mm$ or $0.00625\,D$. As the model's dynamic behaviour is of principal interest in this study, the offset can be neglected.

Figure 3.3 shows the model mounted on to the linear motor before being placed in the air tight box (figure 3.4). The box containing the linear motor is then attached to the underside of the wind tunnel floor. A special floor piece with a $147\,mm$ by $16\,mm$ hole allows the model to move freely along the hole's axis in the wind tunnel. The model deviates by about $0.57°$ (or $0.5\,mm$ over $70\,mm$ maximum travel distance) from the wind tunnel axis in the "surge" configuration. Regarding the "sway" configuration it is aligned in a $90°$ angle to the wind tunnel walls. The box is tested for its air tightness on a regular basis.

The linear motor is controlled by the software provided by the manufacturer (LinMot Talk 6.5 Build 20170116). The software allows the user to create time series of positions, accelerations or velocities. It is also possible to load custom time series of positions into the programme. A built-in oscilloscope function allows tracking of the motor's parameters (demanded position, real position, offset).

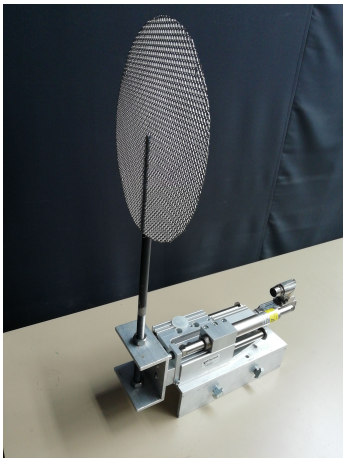

Figure 3.3 – The linear motor used for 1 Dof tests. The actuator disk model is fixed using the two holes in the front. A thread secures the mast's position using countered nuts to avoid any movement.

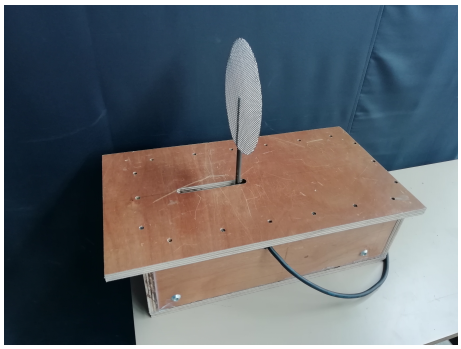

Figure 3.4 – The air tight box containing the linear motor used for 1 Dof tests. The joints are sealed using silicone and glue where necessary. The hole for the cable is sealed using a sponge-type material.

3 Dof Motion System

In the course of the work a 3 Dof motion system is developed. The 3 Dof motion system can reproduce all motions in the X-Z plane (surge, heave and pitch). An image of the installed 3 Dof motion system can be found in the appendix (see figure A3). The x axis actuator is an AFAG PDL40-01170-D27 linear motor. The z axis actuator is an AFAG ES30-100-SL model actuator. The rotational motion is produced by an RE-75 brushless motor. All elements used can be used modularly. A control unit guides each Dof with a temporal resolution of $1\,ms$. The motion system is controlled by Motion Perfect v5.0.3 software. The software has an interface allowing for its integration into the overall wind tunnel control software. It provides the same functionality as the software used for the 1 Dof motion system but can also return the real position of each axis. The demanded and achieved stroke lengths and rotations as well as the necessary velocities and accelerations are presented in table 3.3.

Table 3.3 – Table showing the demanded values (left) of distance and velocity with their corresponding values that the 3 Dof motion can achieve (right).

Dof	**Distance**	**Velocity**
Dx	50 | 170 $[mm]$	2 | 3 $[m/s]$
Dy	2 | 100 $[mm]$	0.3 | 3.2 $[m/s]$
Ry	4 | 360 $[°]$	50 | 1200 $[°/s]$

The motion system is capable of reproducing all travel distances as determined

to be characteristic for FLOATGEN. The x axis has a travel distance of 170 mm and the z axis of 100 mm. Rotation can be achieved in any desired range. It is expected that the system can not meet the maximum accelerations initially demanded but gets sufficiently close. Figure 3.5 shows a comparison between the commanded position (blue) the instantaneous position of each axis (coloured points) as returned by the motion system. Five repetitions of each run are displayed. The x axis has an average error of ±1% between the commanded and real positions. The real position of the z axis diverges by ±2% from the command. The average error between the real and commanded angle is ±1%. The slight shift in between the reference line and the data highlights these small shifts in figure 3.5. An average temporal offset of 4 ms is present. More tests are necessary to determine if this offset is constant or can also fluctuate. The same tests for effects of vibrations and the magnetic field are carried out for the 3 Dof system as for the 1 Dof system. No adverse effects on the measurement technology are found.

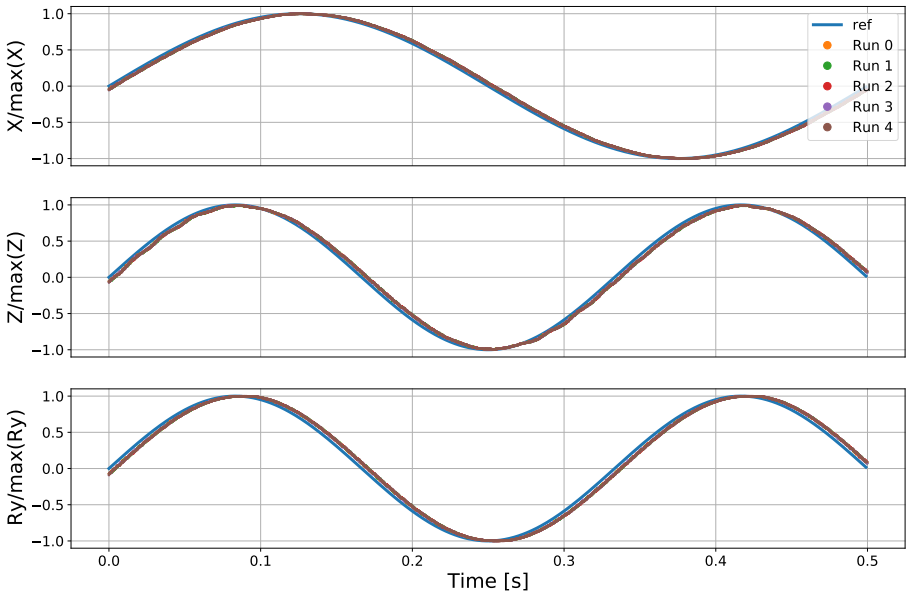

Figure 3.5 – The instantaneous deviation of the commanded position (blue) and five repetitions of a sinus curve (coloured points) for the x (top), z (middle) and R_y components of the 3 Dof motion system. Each curve is normalised by the respective maximum position for better comparability.

The linear motor technology employed in the scope of this thesis proved to be reliable and well suited for the tasks at hand. Care must be taken however when locating measurement equipment in the immediate vicinity of the motion system as vibrations may have an effect on the measurement. The magnetic field is found to be of no risk for the equipment used. With its elaborate control system the 3 Dof motion system is very versatile and can be used in other experiments.

3.2.2 The Actuator Disc

As discussed in section 2.2.2, the actuator disc (or porous disc) concept can be used to study wind turbine wakes further downstream than x/D=3 in turbulent boundary layers. The porous disc is made of the same mesh used in an earlier study (Aubrun et al., 2019). The disc has a uniform solidity of 57%. The disc is fixed on to a mast ($r = 5\,mm$) using two screws to avoid any unwanted motion of the disc while the model is subjected to motion. The mast is fixed to the motion system beneath the wind tunnel floor. The porous disc in the present study has a diameter D of $160\,mm$ and a hub height of $h = 120\,mm$. The thrust coefficient C_t is estimated to be approximately 0.65 (Aubrun et al., 2019). Figure 3.6 shows the actuator disc used.

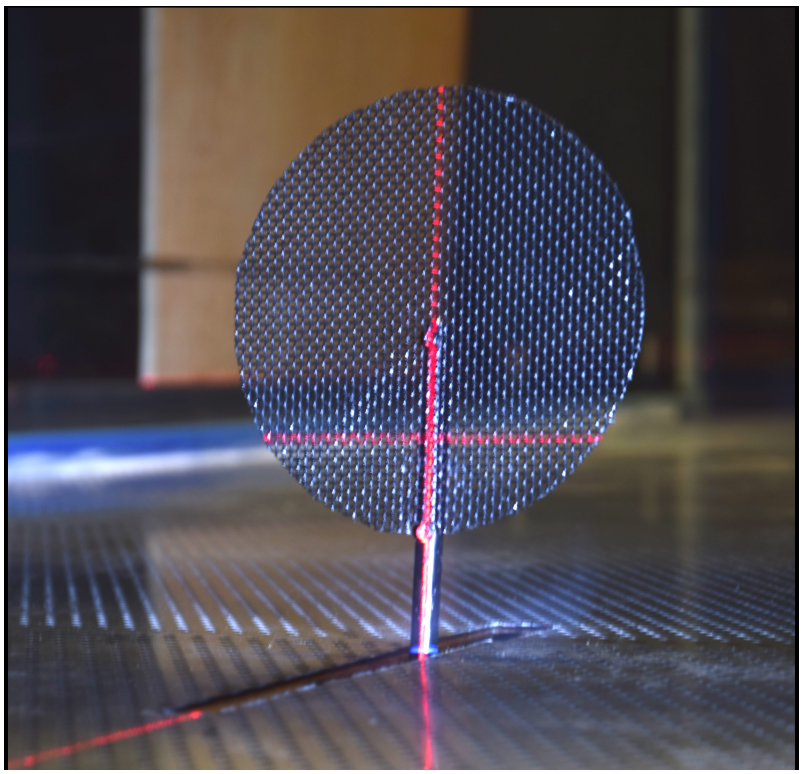

Figure 3.6 – Photo of the porous disc model mounted in the wind tunnel at a pitch angle. **Credit: Thibaud Piquet, CNRS, LHEEA**

The actuator disc has been proven to be a reliable approach to modelling the far wake of a wind turbine. It has also been demonstrated that wake meandering can be reproduced, as the meandering is governed by large scale turbulence present in the ABL (see section 2.2.2). When using the actuator disc concept it is assumed that the turbine's induction factor a, the power coefficient C_p and the thrust coefficient C_t are constant. As fluctuations are expected to be more significant when studying FOWTs, this assumption is tested in the following using numerically simulated data for an FOWT similar to FLOATGEN provided by D-ICE Engineering using the NREL's FAST model. A selection of different sea conditions are tested as shown

in table 3.4. These are equivalent to a fixed turbine, the most frequent sea state encountered at the SEM-REV test site and the operational limit of FLOATGEN. Each configuration is seeded four times, leading to a total of 12 simulations. The turbine is the NREL 5 MW with a diameter of 125 m and a hub height of 90 m. The associated floater is the ITI Energy Barge with a moon pool. The barge's dimensions are 40 m by 40 m by 10 m (width/length/height). The moon pool is 10 m long, 10 m wide and also 10 m deep. The turbulence levels (8%) in the inflow are set according to the VDI guideline 3783 for an offshore atmospheric boundary layer. The inflow conditions are identical for all simulations. The average over the four time series with different seedings is calculated for a, C_t and C_p, respectively.

Table 3.4 – Table showing the inflow conditions, sea states and the equivalent meaning of each configuration used for simulating an FOWT using FAST.

U_{inf}	I_{inflow}	**hs**	**tp**	**Equivalent**
12.5	8.0	0.00	1.00	fixed turbine
12.5	8.0	4.25	11.37	operational limit
12.5	8.0	0.80	10.10	most frequent

Figure 3.7 shows the induction factor a (left hand panel), the thrust coefficient C_t (central panel) and the power coefficient C_p (right hand panel) as a function of the sea state. The error bars show the standard deviation. All three mean values are dependent on the sea state. The standard deviations of a and C_t also depend strongly on the sea conditions. Regarding C_p the standard deviation is not as clearly affected as for the other quantities.

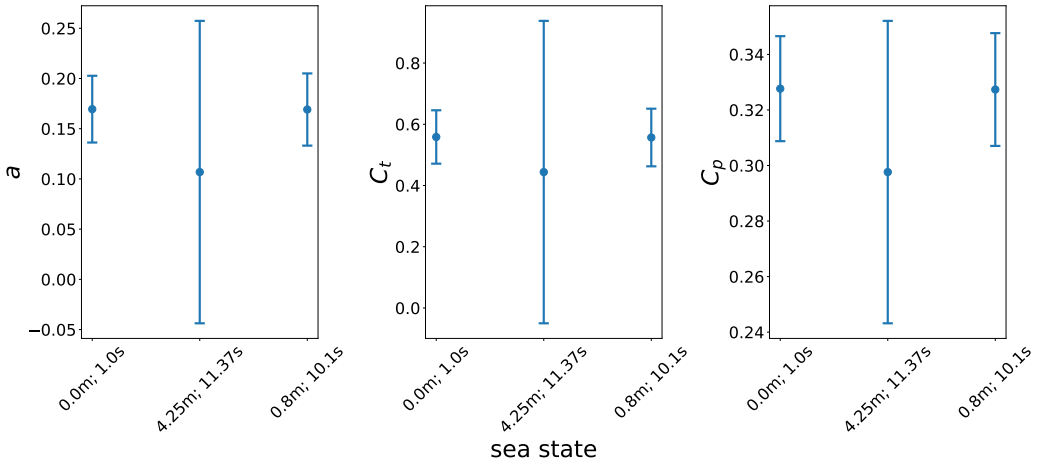

Figure 3.7 – Means of the induction factor a, the thrust coefficient C_t and the power coefficient C_p as a function of the sea state. The error bars indicate the standard deviation.

From the information presented above, C_t, C_p and a vary significantly, especially when the sea is rough ($H_s = 4.25\,m$, $T_p = 11.37\,s$). Yet the porous disc concept

implies that these quantities are constant. This assumption cannot be confirmed at this point, thus limiting the applicability of the porous disc to FOWT investigations using calmer sea conditions. The porosity of the disc could be varied according to the sea state, yet this would only reflect the modified mean values of C_t, C_p and a and not their increased variability.

3.2.3 Measurement Technology

This section gives a brief overview of the instrumentation used in the course of this investigation. The instrumentation consists of a Cobra probe, hot-wire anemometers and a PIV system. Each instrument and the corresponding data processing will be explained below.

The Cobra Probe

The following information is summarised from the Cobra probe's manual (Turbulent Flow Instruments, 2015). The Cobra probe (TurbulentFlow Instrumentation Series 100) is a "multi-hole pressure probe that provides dynamic, 3-component velocity and local static pressure measurements in real-time" (Turbulent Flow Instruments, 2015). At acquisition frequencies up to $2\,kHz$ it can be used in a wide velocity range, depending on the model (up to $10\,ms^{-1}$ in the case of this work). The acquisition frequency is set to $1250\,Hz$. According to its manual the data measured by the Cobra probe can be used to measure velocities in a cone of $\pm 45°$ around the probe's head, including all Reynolds stresses and higher order turbulent quantities.

The probe measures the incoming flow at its head. The pressure measured at the head is always relative to the pressure measured at the reference pressure port (see figure 3.8). The registered voltage signal is passed on to the "TFI Device Control" software where it is processed and converted to velocity data. This software is a black box for the user, as there is no precise description available of the signal processing, conversion and compensation methods applied to the data. The behaviour of the

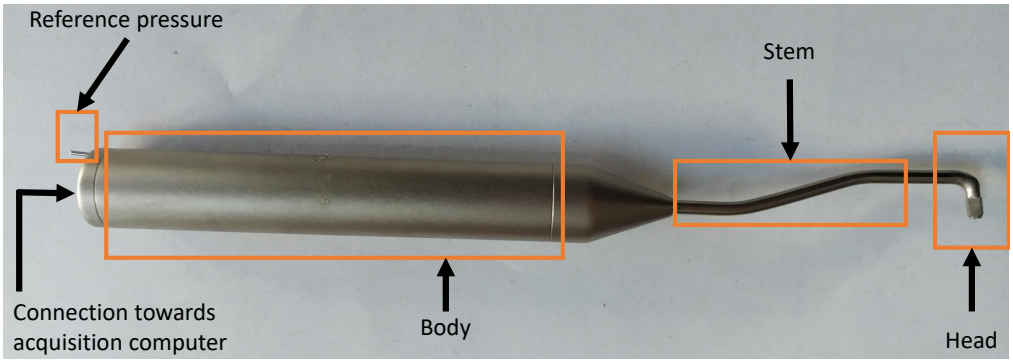

Figure 3.8 – A Cobra probe. It is composed of a head with four holes, a stem connecting the head to the body. The top end of the body houses the connections to the reference pressure and the acquisition technology.

probe corresponds to what would be expected from the Boyle-Mariotte law for air density (equation 3.3) when compensating velocity calculations for changes in air density:

$$\rho = \frac{1.293}{1 + 0.00367\,T} \frac{H}{101300} \tag{3.3}$$

where ρ is given in $kg\,m^{-3}$, H (pressure) in Pa and T (temperature) in $°C$.

It is known that temperature and pressure corrections are made, as this data is needed as input when converting the raw data to velocities. A proper conversion is assured by calibrating the membranes within the probe. The only calibration required to be carried out by the user in an interval of six months is a static calibration. This calibration assures that the voltage to pressure conversion factors are correct. The static calibration process requires the application of a series of stable pressures to the reference pressure port. The calibration process is highly automated using the software delivered with the probe. The software only needs to be given the applied pressure.

Regarding the installation of the Cobra probe at the LHEEA atmospheric wind tunnel facility, it is necessary to connect the reference pressure port of the probe to a static pressure probe, as the whole Cobra probe is in the flow at all times. The connection to the static pressure probe in the tunnel assures that the velocity data is not distorted by pressure variations outside of the wind tunnel. Furthermore, the probe is "zeroed" before every measurement. This short measurement of $40\,s$ conducted in a stationary flow is used to estimate an offset by the data conversion software. The Cobra probe is controlled using "external" triggers in the wind tunnel control software to assure that there is no overlap between positioning motion and measurement. The Cobra probe is used for measuring vertical profiles of velocity and turbulent quantities as well as spectra.

The data measured with the Cobra probe is read and analysed using pandas 1.0.1 in Python 3.7 (Hunter, 2007). Zeros are removed from the time series as these values result from a potential saturation of the probe. No more than 0.14% of data points are removed. After applying these steps the data is used to calculate the turbulent quantities and spectra as desired. The spectra are calculated using the Welch method as implemented in scipy 1.4.1 (Virtanen et al., 2020). A Hann window of 4096 points is applied to the Welch method. This corresponds to roughly $3.3\,s$. The overlap is 50%. The acquisition time is $300\,s$ for vertical profiles and $1800\,s$ for spectra measurements. The frequency response of the Cobra probe is approximately $200\,Hz$.

Hot-wire Anemometry

A hot-wire anemometer (Dantec Type 55-P11 probe) is used to deliver complementary data to the Cobra probe. The probe is also capable of delivering high

frequency flow data, though only regarding the effective flow velocity normal to the wire. The basic principles of hot-wire anemometry will be explained in the following. The source of the information is Bruun and Bruun (1995) unless otherwise noted.

Hot-wire anemometry has been used extensively in turbulence research in the past (e.g. Aubrun et al., 2015; Muller et al., 2015). The measurement principle is based on maintaining the temperature or the current of a heated wire constant while it is immerged in to a flow. As only constant temperature anemometers (CTA) are used in the scope of this thesis, only these will be presented. For more information on constant current anemometers the reader is referred to Bruun and Bruun (1995).

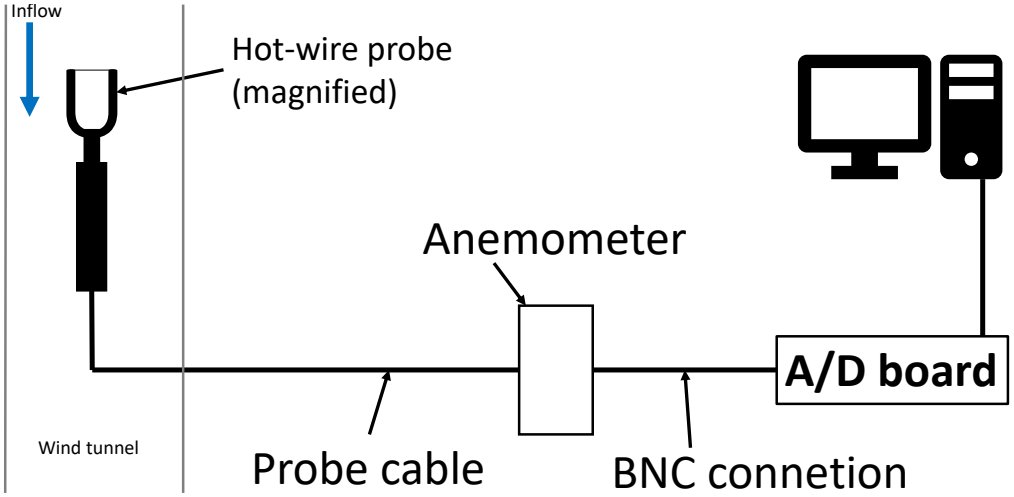

Figure 3.9 – Sketch of the principle set-up of a hot-wire measurement. The hot-wire probe is placed in the flow. The probe is connected to the anemometer which in turn is connected to the A/D board. The A/D board delivers the digital signal to the measurement computer.

A typical set-up of a hot-wire measurement is depicted in figure 3.9. The hot-wire probe is placed in the flow. It is then connected to the anemometer that is usually located outside of the wind tunnel. The anemometer measures and processes the signal before transferring the data to an analog-digital (A/D) board for conversion to a digital signal. The digital signal is then saved on the measurement computer.

The wire has a diameter of $5\,\mu m$ and a length of $1.25\,mm$. Tungsten wires are used here. As the velocity of the medium flowing around the wire changes, so does the heat transfer coefficient of the wire, thus changing its temperature. To maintain the temperature, or rather the electrical resistance, of the wire a CTA changes the current applied to the probe. The changes in current are registered and allow a conversion to a velocity (equation 3.4):

$$R_w I_w^2 = (T_w - T_a)\Phi conv(U) \tag{3.4}$$

with R_w being electrical resistance of the wire, I_w the current in the wire, T_w is the wire's temperature, T_a is the applied temperature and $\Phi conv(U)$ is the U-dependent

transfer function.

As the hot-wire anemometers are sensitive to changes in the surrounding conditions it is necessary to calibrate the probes once or twice a day. The aim of the calibration is to attain reliable coefficients using King's law (King, 1914) to calculate the velocity from the measured electrical data:

$$E^2 = A + BU^n \tag{3.5}$$

where E is the CTA output voltage, A, B and n are coefficients, U is the velocity. The coefficients calculated using equation 3.5 describe the interaction between the probe and the CTA.

Given, as in this study, only single wire probes are used, only the flow velocity needs to be modified for calibration purposes. The reference velocity is measured by a pitot tube near the hot-wire probe. The flow velocity is systematically varied and the data of the pitot tube and the hot-wire anemometer are measured. The data is fed to an in-house Python programme that determines the coefficients for King's law. The programme determines the coefficients by using a best-fit approach to the velocity profiles measured. These coefficients are then applied to the transfer function to determine the flow velocity from the voltage measured by the CTA. Pressure and temperature corrections are applied to the data in order to account for variations in these quantities during measurements conducted after the calibration. The quality of the calibration is measured by the χ^2 error of the fitted curve through the different velocities. The χ^2 error is in the range of from $4 \cdot 10^{-4}$ to $1 \cdot 10^{-6}$ for all probes. The majority of the fits have a χ^2 error around $4 \cdot 10^{-5}$. Inherent to this estimation is the error of the pitot which is estimated to be $\pm 1\%$.

The hot-wire data is of high quality, with only single outliers removed. The data is read using pandas version 1.0.1 (Hunter, 2007). As with the Cobra data the spectra are calculated using Python 3.7 with scipy 1.4.1 and the Welch method included therein (Virtanen et al., 2020). The applied window size is set to 65536 points or approximately $4.4\,s$ with a 50% overlap. The acquisition frequency is $15\,kHz$ with an acquisition time of $1800\,s$. The frequency response of the hot-wires is in the range of $1\,kHz$.

Particle Image Velocimetry

In order to gain an understanding of the spatial development of the wake a stereoscopic Particle Image Velocimetry (S-PIV) system is employed. This system can extract all three velocity components from the images taken. In the following the basic function of an S-PIV system is described, including the specifics used in the scope of this thesis. Unless noted otherwise, the information presented in this section is based in Raffel et al. (2007).

Generally, PIV measurements involve several systems. These include a particle

source, a laser and high speed cameras as well as a powerful computer. The reflecting particles, either theatre smoke or dispersed olive oil in this case, are injected into the flow. The particles function as a tracer in the flow. In the area of interest the particles are illuminated by two pulses from the laser. The high speed cameras capture the scattered light from the particles. One image is taken for each laser pulse. These images are transferred to the computer for evaluation. At this point the necessity for powerful computing power becomes evident as large amounts of data need to be treated. The laser and the cameras are centrally triggered by a control unit.

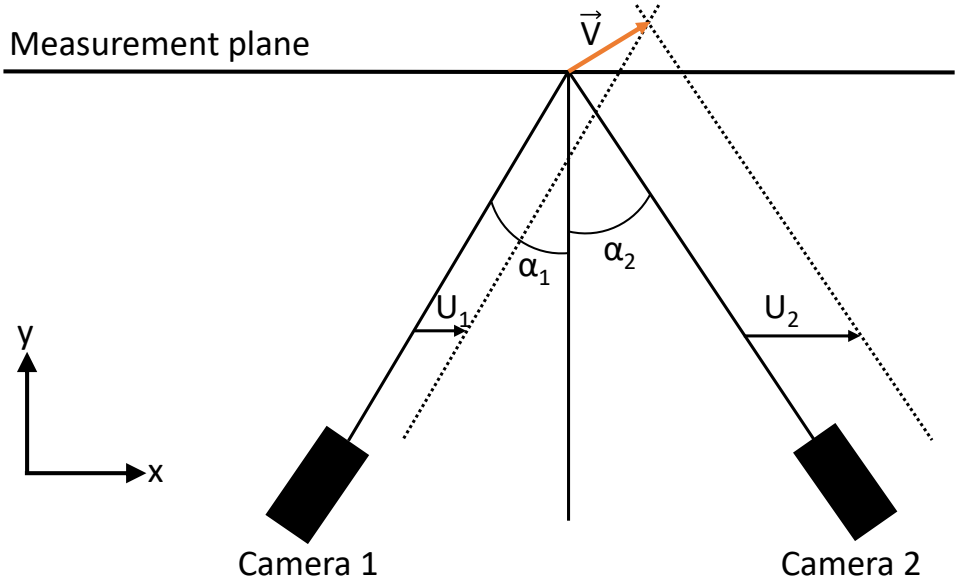

Figure 3.10 – The geometric relations required to reconstruct the out-of-plane velocity component using S-PIV. $\vec{V}$ is the out-of-plane velocity vector with the components U, V and W, and α is the angle between the reflected ray of light and the y axis. The subscripts attribute the variables to the cameras.

The images are evaluated by the PIV system's developers proprietary software. Basically, the distance travelled by a particle between the pulses is estimated using cross-correlation algorithms. The images are transformed to a grey scale. The images are reduced to interrogation windows of a given size. As the images from each camera come in pairs, the displacement of a given particle in an interrogation window can be traced using correlation functions. These cross-correlation algorithms can detect corresponding particles in back-to-back images. Given that the time between the pulses is known, the in-plane velocities U and W can be calculated. The out-of-plane velocity component V can be estimated using stereoscopic PIV.

In order to measure the out-of-plane velocity, the S-PIV analysis software exploits the geometry between two cameras pointed at a mutual area of interest. These geometric relations are visualised in figure 3.10. The three velocity components can

be reconstructed using the following relations:

$$U = \frac{U_1 \cdot \tan\alpha_2 + U_2 \cdot \tan\alpha_1}{\tan\alpha_1 + \tan\alpha_2} \tag{3.6}$$

$$W = \frac{W_1 \cdot \tan\beta_2 + W_2 \cdot \tan\beta_1}{\tan\beta_1 + \tan\beta_2} \tag{3.7}$$

$$V = \frac{U_1 - U_2}{\tan\alpha_1 + \tan\alpha_2} = \frac{W_1 - W_2}{\tan\beta_1 + \tan\beta_2} \tag{3.8}$$

where U, V and W are the velocity components. α is the angle between the reflected ray of light and the lateral plane. β is the angle between the reflected ray of light and the camera's line of sight in the vertical plane. The subscripts attribute the variables to the cameras. As there are three variables and four measured values, the system can be solved.

In order to correctly measure all velocity components in the area of interest a calibration of the cameras is necessary. This is achieved by using a dot marked plane, where the distance between the dots is known. Using this raster as reference, a mapping algorithm can transfer the raw images to reconstructed images in the correct reference system, thus allowing for the calculation of the velocity components in the wind tunnel's coordinate system. For S-PIV purposes the calibration has to be carried out at systematically varied distances from the cameras. When calibrating, special attention must be given to aligning the calibration target correctly with the measurement plane. An offset between the two during calibration will lead to incorrect reconstruction of the velocity components.

Specifically, the system used in the scope of this thesis is a Dantec High Power Nd:YAG laser (wavelength: $532\,nm$) in combination with two HighSense Zyla cameras with $60\,mm$ lenses. Dantec Dynamic Studio 6 is used for the set-up process, the acquisition and the processing of all S-PIV data used. A calibration target with evenly spaced points is used. The points have a distance of $12\,mm$ and a diameter of $6\,mm$. The target is mounted to a support structure that enables a precise alignment with the laser sheet. Optical displacement equipment allows for the precise adjustment of the target's distance from the cameras for S-PIV calibration.

The acquisition frequency when using the S-PIV system is set to $7.1\,Hz$ to avoid being in-phase with the motion frequency as much as possible. 9999 image pairs are taken per data-set resulting in a measurement time of roughly 24 minutes. A delay of $500\,\mu s$ between two images of the same pair is chosen. The raw images are processed by applying a two-pass cross-correlation with a final interrogation window size of $32\times$ 32 pixels and an overlap of 50% both horizontally and vertically. This results in a resolution of $2.6\,mm \times 2.5\,mm$ for the final vector field. The vector fields

have a size of $300\,mm \times 280\,mm$.

3.3 Quality Checks

This section presents the quality checks imposed on both the measurements and the flow conditions themselves. First the work conducted to improve the flow conditions within the wind tunnel is presented. These represent a significant part of the total work carried out in this study to guarantee high quality data. The modelled boundary layer is then presented (section 3.3.1). Sufficient convergence times (section 3.3.3) and Reynolds Number independence (section 3.3.4) are checked to verify that each measurement's data is representative and coherent. The uncertainty estimation indicates the overall quality of the data and is presented in section 3.3.5.

3.3.1 Flow Conditions

A considerable challenge in the context of this study are the flow conditions in the wind tunnel. As a low turbulence atmospheric boundary layer is required by VDI guideline 3783 for modelled maritime boundary layers, the flow in the wind tunnel needed optimisation. The reasoning for the steps taken and the resulting improvements will be briefly outlined.

All tests outlined in this section are carried out in the LHEEA atmospheric wind tunnel. The wind tunnel is empty to limit unforeseen interactions between different elements. Three steps proved to be the most important when understanding and improving the flow in the wind tunnel. Three steps proved to be of the most importance for understanding and improving the flow in the wind tunnel: the installation of corner fillets, the reduction of pressure loss at the intake, and, the investigation of the sensitivity of the Cobra probe. Apart from these three steps routine maintenance is performed on the wind tunnel itself and its motor.

The theory behind corner fillets is that they diminish corner vortices in a square duct (for example Johl, 2010) by removing the right angles in the corners (see figure 3.11). According to Mehta and Bradshaw (1979) the pressure gradient within the wind tunnel can be influenced positively with properly designed corner fillets.

Light weight polystyrene panels serve as low-cost and easy to handle corner fillets. Their light weight is an advantage when handling the material and, especially, when fixing the corner fillets to the wind tunnel walls. Derived from the geometry of the wind tunnel, the exposed side of the fillets has a length of $212\,mm$. A combination of double-sided tape and duct tape holds the fillets in place. This combination allows for a secure hold while also allowing for easy removal of the fillets, should that become necessary. Potential gaps between the single polystyrene panels are covered using normal tape. The tape also ensures that the joints are sealed in an air-tight manner avoiding unwanted injections into the boundary layer flow.

The installation of the corner fillets already improves the overall flow in the wind

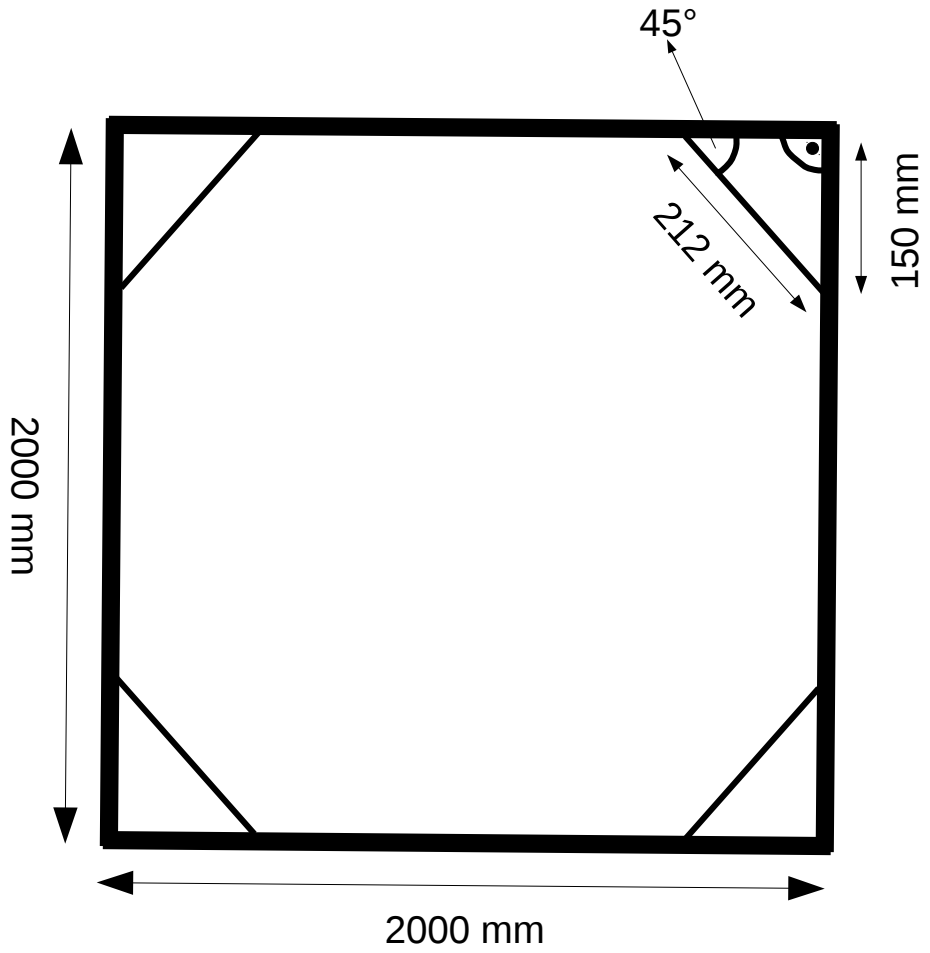

Figure 3.11 – Cross-section of the wind tunnel with corner fillets and their dimensions.

tunnel (see figure A1). In the course of the verification measurements, a pressure differential of $\Delta p \approx 2\,Pa$ at a free-stream velocity of $4\,ms^{-1}$ is detected between the centre and the sides of the wind tunnel. Considering that the wind tunnel is empty at this stage, it is unlikely that the disturbance is caused by elements within the wind tunnel. An inhomogeneous flow intake is considered as the origin of the pressure differential. The inhomogeneity is linked to the use of the space around the wind tunnel facility. In order to counteract the inhomogeneous inflow conditions a second layer of filter material is added to the wind tunnel's intake. The pressure differential is measured again. The resulting data shows a pressure differential $\Delta p \approx 0.2\,Pa$ at a free-stream velocity of $4\,ms^{-1}$, within the measurement uncertainty of the set-up. The filter material increases the pressure loss at the intake, thus slowing the inflow further and reducing the impact of an externally inhomogeneous flow.

To be sure to gain the best understanding possible of the Cobra probe's behaviour and to be sure to be dealing with high quality data a test of different offset (or zero) conditions is conducted (see figure A1 in the appendix). Each offset measurement is applied to the same base data set. The tests reveal that the zeroing process is

relatively insensitive to blocked probe entries or minimal flow disturbances. Yet TurbulentFlow's data processing software is sensitive to changes in pressure and, even more so, temperature. This can be expected when considering equation 3.3 in section 3.2.3 for calculating air density as a function of pressure and temperature.

The measures taken (installation of corner fillets, improved inflow conditions and understanding the probe's sensitivity) to improve the flow conditions in the wind tunnel are successful. The difference between the first profile measured and the final configuration is significant and warrants the efforts put into improving the flow (see figure 3.12). The final boundary layer configuration is characterised in the following section.

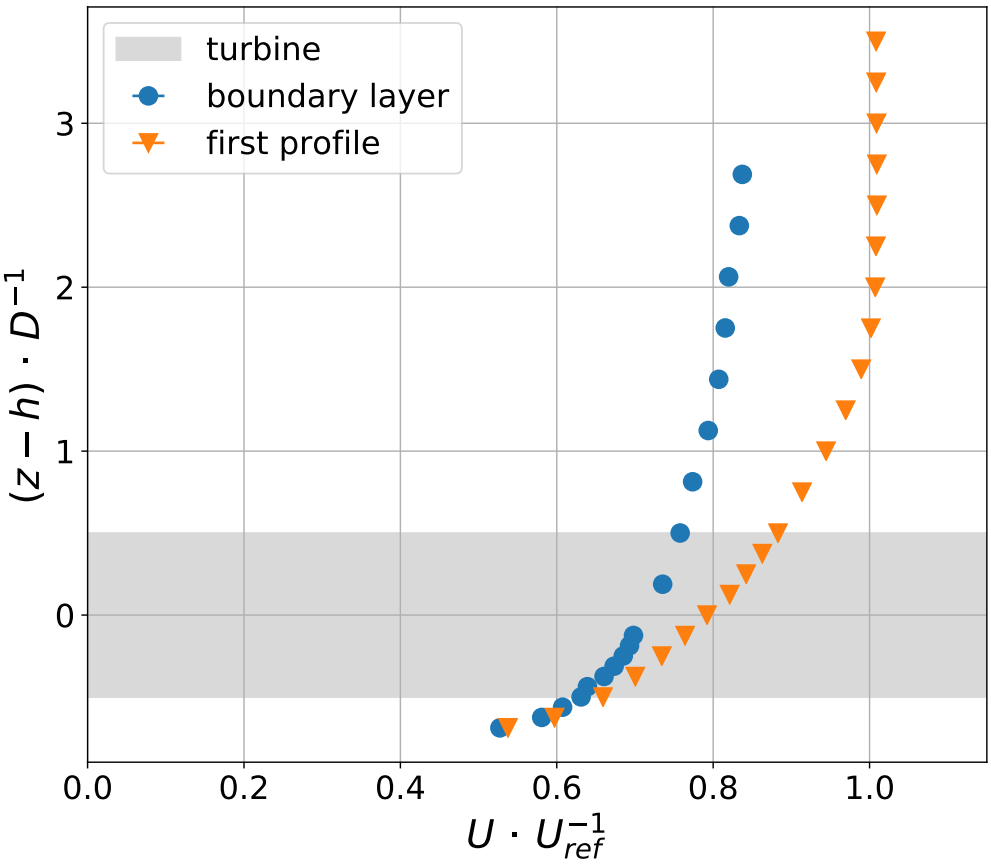

Figure 3.12 – Profiles of the first normalised mean velocity profile (orange) and the final boundary layer profile (blue).

3.3.2 The Modelled Boundary Layer

As has been shown in section 2.2.2, the inflow conditions have a significant impact on the development and characteristics of the wake of a wind turbine. The ABL's turbulence intensity and integral length scales play important roles. It is thus necessary to correctly model the atmospheric boundary layer as well as possible.

The boundary layer is developed in the wind tunnel using established practices. A 36 mm high trip and spires (base width= 100 mm, height= 1250 mm) placed at

the end of the wind tunnel's convergent are used to generate the larger turbulent scales in the boundary layer flow. Perforated metal plates ($1980\,mm \times 1000\,mm$, hole diameter $d = 5\,mm$) generate small scale turbulence in the near-ground area of the boundary layer (see figure 3.13). After a development fetch of $\approx 18\,m$, the turbulent boundary corresponds to a scaled maritime boundary layer according to the VDI guideline 3783 (VDI, 2000). These reference values will now be shown and compared to those calculated or measured in the boundary layer flow.

The final set-up described above delivers a slightly rough boundary layer at the upper end of the category as put forth by the VDI (see table 3.5). The surface roughness z_0 is calculated at $5.5 \times 10^{-6}\,m$ just below the reference value of $10^{-5}\,m$. The velocity profile's power law α is 0.11, within the VDI's limits of 0.08 and 0.12 for a flow above a slightly rough surface. The displacement height is 0, in line with the reference data.

Figure 3.14 shows the mean flow magnitude (left hand panel) which follows the expected exponential profile of an atmospheric boundary layer flow. The mean longitudinal flow component U follows the mean magnitude's profile (centre left panel). Both the mean lateral flow component V and the vertical flow component W are near zero, as expected. W is slightly negative, as theory suggests and V is slightly positive. This indicates that there is a limited amount of lateral flow present. The mean values are averages over $600\,s$.

As figure 3.15 indicates the turbulence intensities of all flow components are within the VDI guideline's boundaries. The longitudinal turbulence intensity I_u (left hand panel) is at the upper limit of the suggested boundaries. The lateral and vertical turbulence intensities (central and right hand panel, respectively) are in the middle of the boundaries within the rotor swept area (grey surface). Overall, the turbulence intensity profiles suggest that the boundary layer flow is of good quality. Boundary layer theory suggests that the ratios between I_v/I_u and I_w/I_v is 0.75. The ratio I_w/I_u is expected to be 0.5. At hub height the ratio between I_v/I_u of the modelled BL is 0.73, while it is 0.59 for the ratio I_w/I_u. The ratio between the measured I_w and I_v is 0.8. The ratios between the respective I indicate that the turbulence intensities are well reproduced in the modelled BL.

Table 3.5 – Adaptation from VDI Guideline 3783. z_0 is the roughness length, α the exponent coefficient and L_u^x the integral length scale. Added values for the modelled boundary layer.

Roughness class	Target values	**Modelled**
Type of terrain	ice, snow, water surface	**water surface**
$z_0\ [m]$	10^{-5} to 5×10^{-3}	$\mathbf{5.5 \times 10^{-6}}$
α	0.08 to 0.12	**0.11**
$d_0\ [m]$	≈ 0	**0**

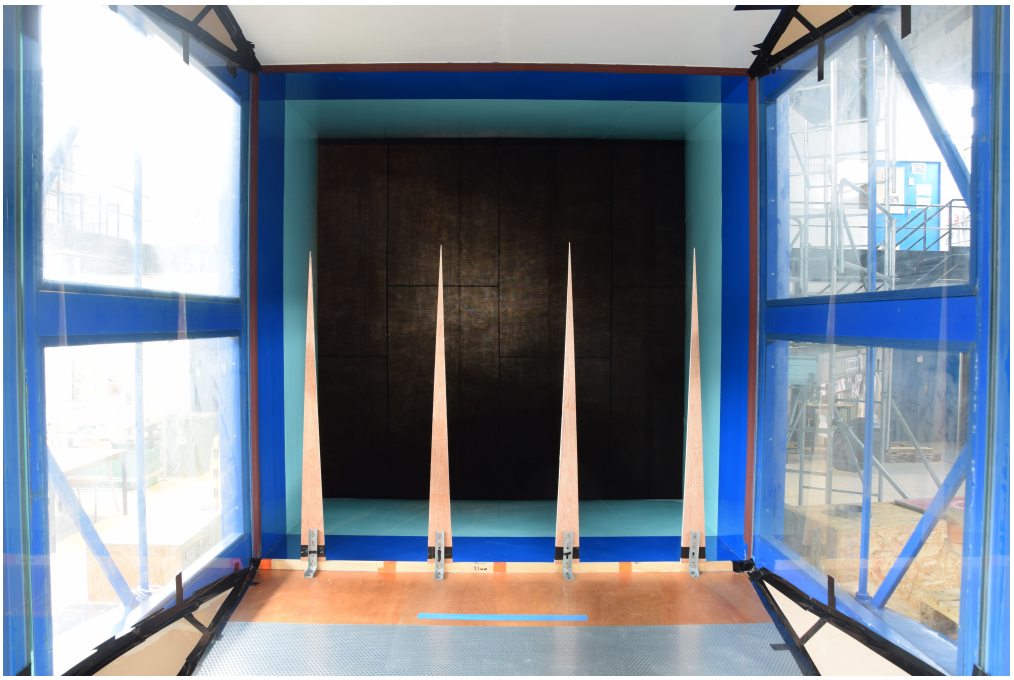

Figure 3.13 – Turbulence generation at the LHEEA atmospheric wind tunnel facility. A trip and spires placed at the end of the wind tunnel's convergent are used. Perforated metal plates are placed on the ground to enhance small scale turbulence development. The beginning of the corner fillets are also visible in the corners of the wind tunnel.

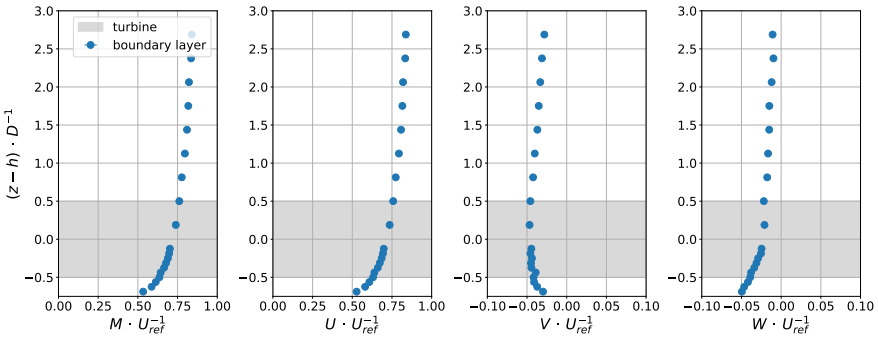

Figure 3.14 – Velocity profiles of the mean magnitude M (left), the mean longitudinal flow component U (centre left), the lateral flow component V (centre right) and the vertical flow component W (right). All velocities are normalised using the reference mean magnitude U_{ref} measured outside of the boundary layer. Error bars are added, but not visible due to their small values.

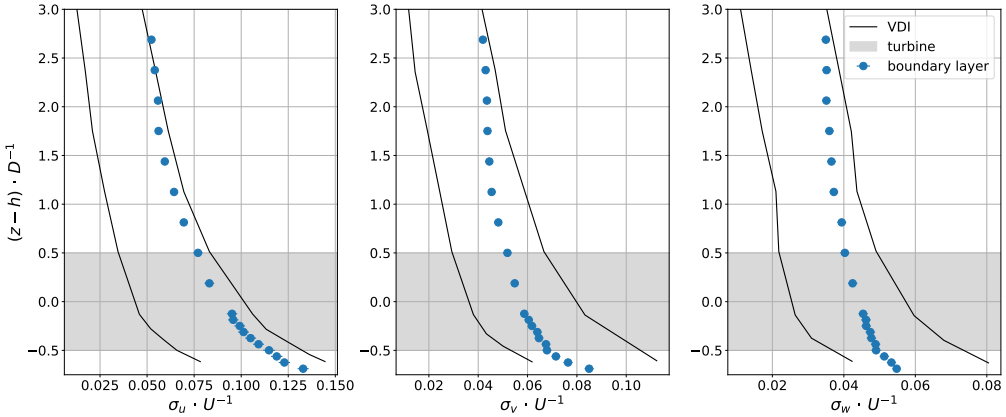

Figure 3.15 – Turbulence intensity profiles of the longitudinal flow component $\sigma_u \cdot U^{-1}$ (left), the lateral flow component $\sigma_v \cdot U^{-1}$ (centre) and the vertical flow component $\sigma_w \cdot U^{-1}$ (right). Error bars are added, but not visible due to their small values.

The integral length scale (L_u^x) is calculated at all profile positions (figure 3.16) according to Counihan (1975):

$$L_u^x = U \int_0^\tau R(\tau)\, d\tau \tag{3.9}$$

where $R(\tau)$ is the autocorrelation of the time series. L_u^x is in line with a L_u^x profile for very small z_0, as calculated for this boundary layer ($z_0 = 5.5 \times 10^{-6}$ m). The VDI guidelines suggests $200\,m < L_u^x < 250\,m$ at $z = 100\,m$ (full scale). The modelled boundary layer delivers $L_u^x \approx 200$ m here, matching the VDI's references. As the reference data in figure 3.16 (black lines, triangles, crosses and lines, from Counihan (1975)) suggests that large variations in L_u^x are possible, thus the results are satisfactory with regard to the integral length scale.

To further assess the boundary layer's quality, the TKE and Reynolds stresses are checked. The left hand panel in figure 3.17 shows that the TKE is more or less constant within the BL, as theory prescribes. In the natural ABL the Reynolds stresses can be considered constant within the Prandtl layer. The Reynolds stresses (figure 3.17, right hand panel) are near zero and nearly constant in the lower part of the profile up to roughly the top tip. The Reynolds stresses vary minimally in absolute terms in this area. The profile is thus close to what would be expected in the natural ABL.

Finally, the dimensionless power spectral density (PSD) of the boundary layer flow is compared to a range of reference data from Kaimal et al. (1972) and Von Karman (1948). Figure 3.18 depicts the premultiplied PSD of the longitudinal flow component U (left hand panel), the lateral flow component V (central panel) and the vertical component W (right hand panel). The dimensionless spectra are plotted

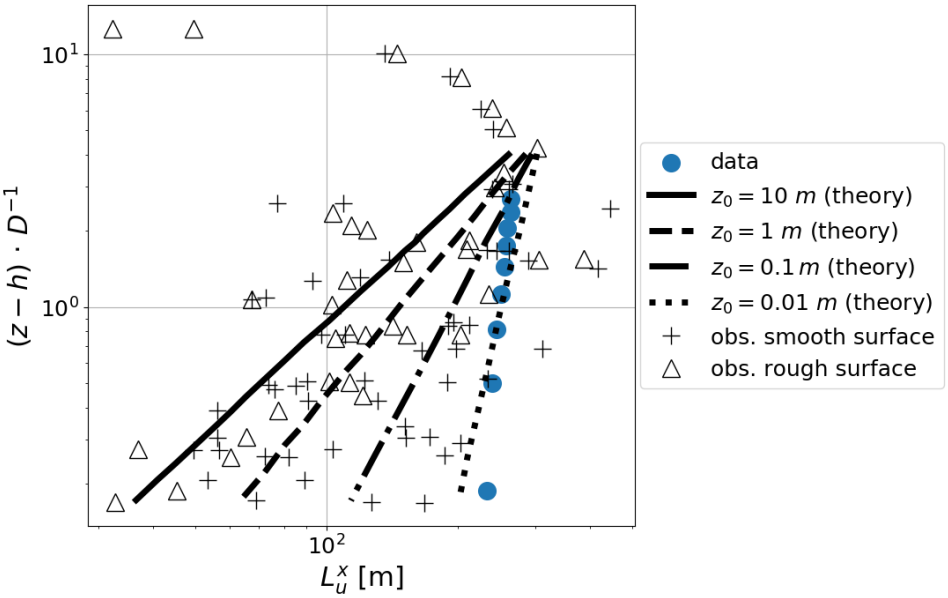

Figure 3.16 – Profile of the integral length scale L_u^x in $[m]$ (blue points). Reference data from Counihan (1975) presented for orientation (black lines show theoretical values, crosses and triangles represent field data). Error bars are added, but not visible due to their small values.

against reduced frequencies:

$$f_{red} = \frac{f \cdot z}{U^{-1}} \tag{3.10}$$

where f is the frequency, z is the height of the measurement above ground and U is the mean velocity of the flow. It is not realistically possible to realise a flow that matches the Kaimal spectrum exactly. The aim is thus to match the shape and the slope of $-5/3$ of the reference spectrum. This is achieved for all flow components as the measured spectra have a declining slope parallel to the Kaimal spectrum. In all cases the measured spectra are shifted towards higher frequencies, implying that smaller eddies play a more important role in the boundary layer.

The modelled atmospheric boundary layer presented here fulfils the VDI guideline's requirements (VDI, 2000). The boundary layer modelled in the wind tunnel is sufficiently similar to a full-scale maritime boundary. Representative and up-scalable measurements are thus possible. The following sections will describe further measures taken to assure representative data such as the convergence times and Reynolds number independence of the wake flow as well as an uncertainty estimation for the data used in the analysis.

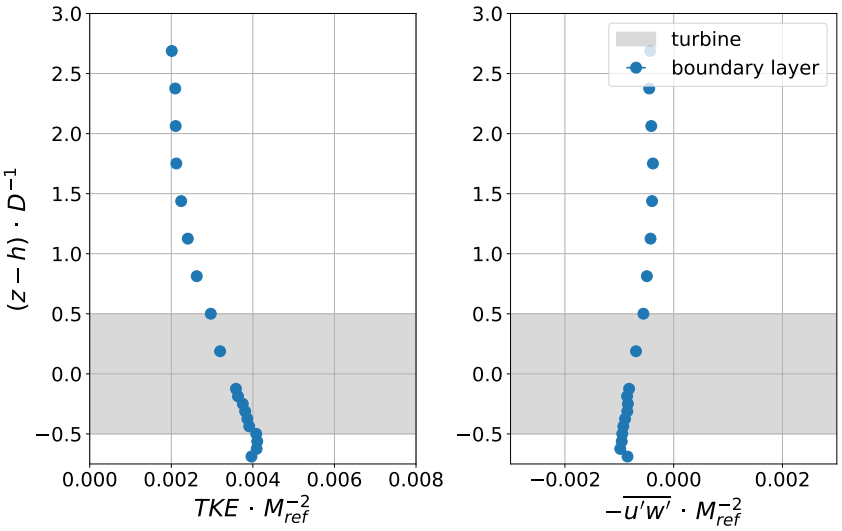

Figure 3.17 – Profiles of the turbulent kinetic energy TKE (left hand panel) and the Reynolds stresses $-u'w'$ (right hand panel). All velocities are normalised using the reference mean magnitude U_{ref} measured outside of the boundary layer. Error bars are added, but not visible due to their small values.

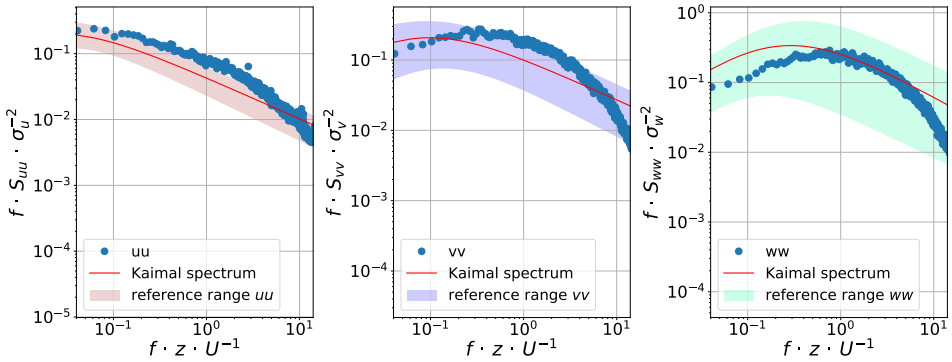

Figure 3.18 – Pre-multiplied power spectral density of U (left hand panel), V (central panel) and W (right hand panel). The shaded areas show the range of available reference spectra provided in VDI (2000). All spectra are shown against a reduced frequency.

3.3.3 Convergence Time

In order to achieve representative measurements, the convergence time of all relevant quantities must be determined. Long measurements are undertaken in the boundary layer flow and in the wake of the moving actuator disc. These measurements are typically taken over a period between 30 and 45 minutes to ensure that low frequency events in the flow are also captured. The time series is averaged over gradually increased subsets of the data. The maximum time step is half the length of the entire time series. This approach is applied to the velocity, the turbulence intensities of each flow component (I_u, I_v and I_w) and the skewness as well as the kurtosis of the flow's longitudinal component u.

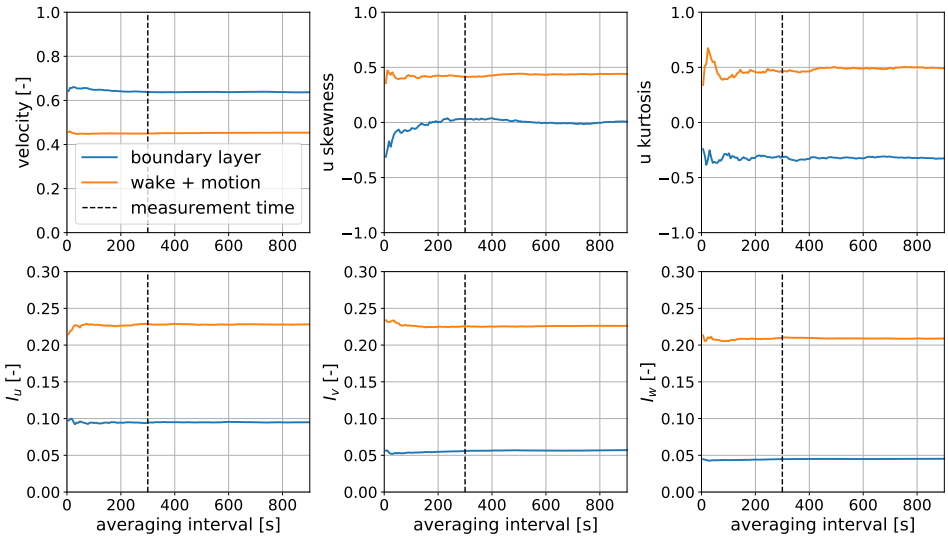

Figure 3.19 – Convergence measurements used to find sufficiently long measuring times. From top left to bottom right: the normalised velocity, u skewness, u kurtosis, I_u, I_v and I_w. The blue line shows measurements made in the boundary layer. The orange data was measured in the wake of a moving actuator disc model at $4.6\,D$ downstream. The dashed black line depicts the limit of an averaging interval of $300\,s$ considered to be sufficient for all values to be converged.

In figure 3.19 the calculated convergence tests are shown. From top left to bottom right the panels depict the normalised velocity, skewness, kurtosis, I_u, I_v and I_w. The measurement time is dictated by the quantity that takes the longest time to converge, kurtosis (upper right hand panel) in this case. As indicated by the dashed black line the kurtosis has converged sufficiently close to its mean values after an averaging interval of $300\,s$. No measurement in this thesis is thus shorter than the indicated $300\,s$. The mean velocity with a sampling time of $300\,s$ varies by 1.1% from the overall mean both in the BL and the wake. The kurtosis is estimated to be within 4.6% of the overall kurtosis for the BL measurement. In the wake this difference increases to 7.2%. Consequently each measurement point in a vertical profile represents a time series of $300\,s$, each spectral measurement, with either the Cobra probe or the hot-wires, is $1800\,s$ long. PIV data is collected

over a time of roughly 1400 s for measurements of the wake and 915 s for boundary layer measurements. These measurement times assure that all relevant quantities are representative of the flow conditions being investigated.

3.3.4 Reynolds Number Independence

Reynolds Number independence is a corner stone of wind tunnel modelling (see 2.1.3). In the case of a wind turbine modelled by an actuator disc two pieces of literature are of special interest. On the one hand, Chamorro et al. (2012) state that a Reynolds Number (Re) of around 48000 is necessary to achieve Reynolds Number independence in the wake of a rotating modelled wind turbine. The authors use a scaled wind turbine model with three blades. They find that the critical Re (i.e. the Re required to achieve Reynolds Number independence) decreases with increased distance from the wind turbine model. On the other hand Mohamed and Larue (1990) postulate that all turbulence generated by a grid is Reynolds Number independent. Even so, it is prudent to conduct a Reynolds Number independence test to clarify in which regime the experiments will be carried out.

In the following the results of a basic Reynolds Number independence test are presented. Several profiles of a wind turbine's wake are measured at varying Re. The Reynolds Number is defined as stated in equation 3.11:

$$Re = \frac{u_{hub} \cdot D}{\nu} \tag{3.11}$$

where u_{hub} is the velocity at hub height, D is the diameter of the wind turbine and ν is the dynamic viscosity. This is the same definition as used by Chamorro et al. (2012). The quantities investigated being the same as those presented in this publication (U, I, TKE, $-\overline{u'w'}$ and u_{skew}). The lowest $Re\,(\approx 15300)$ is dictated by the operational range of the Cobra probe. The highest $Re\,(\approx 28500)$ is at a characteristic velocity used at the LHEEA atmospheric wind tunnel.

Figure 3.20 shows the normalised mean velocity profile for all the Re numbers investigated here. No Reynolds Number effects can be observed as all profiles are sufficiently close and have the same shape. The velocity profiles are normalised using U_{ref}, the flow velocity at the highest point of each profile. Similarly, figure 3.21 shows no large deviations in turbulence intensity for any of the tested scenarios. The profiles for each velocity component are similar. These are primary indicators of Reynolds Number independence for the flow behind a modelled wind turbine when using an actuator disc model.

A more detailed look into the data reveals that the TKE and Reynolds stresses (figure 3.22) further confirm Reynolds Number independence. A slight spreading of the TKE profiles can be observed. This is not associated to increasing Reynolds Numbers. The $Re = 23428$ is the outlier across the profile. It is known that the

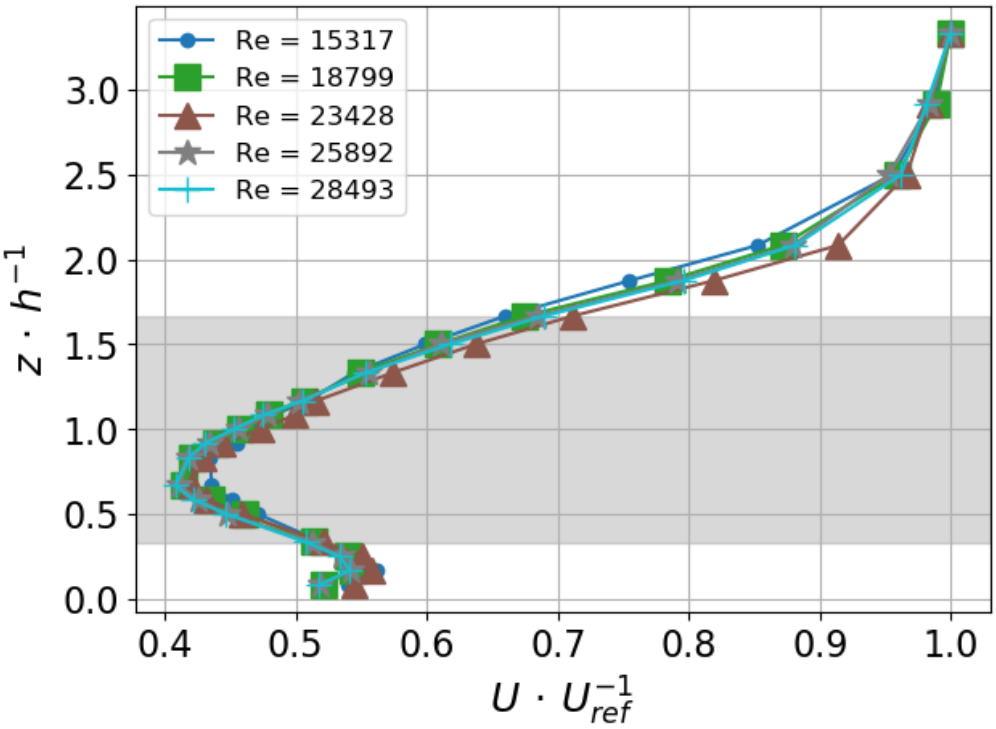

Figure 3.20 – Vertical profile of the normalised velocity $U \cdot U_{ref}^{-1}$ at different Reynolds Numbers (Re). U_{ref} is the highest point measured in the profile. The height z is normalised around hub height h. The grey area indicates the rotor-swept area.

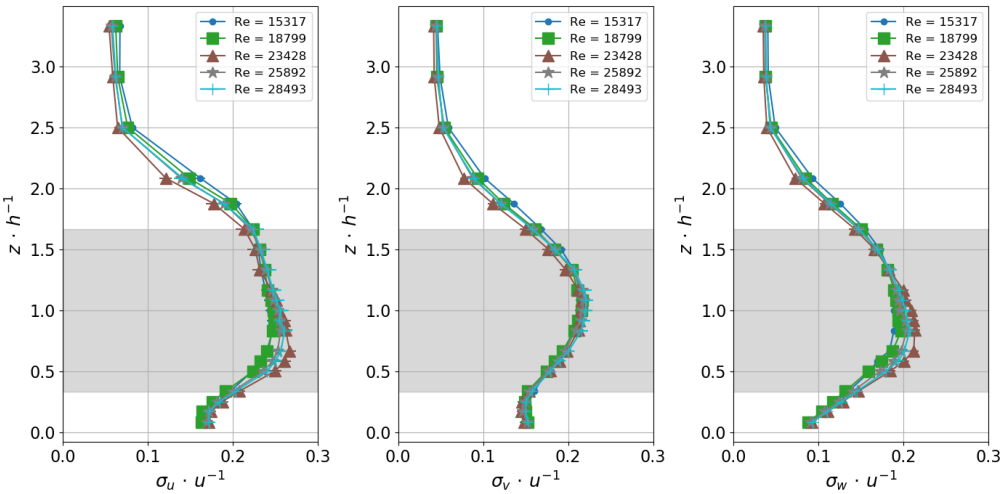

Figure 3.21 – Vertical profile of the turbulence intensity ($\sigma_i \cdot U^{-1}$) of each flow component (i) at different Reynolds Numbers (Re). u is the mean velocity at a given height. The height z is normalised around hub height h. The grey area indicates the rotor-swept area.

LHEEA wind tunnel has elevated vibrations in this operational range, though the origins of which are not known for certain. Regarding the Reynolds stresses the profiles are close above z > 1. A slight spreading of the $-\overline{u'w'}$ can be seen around z = 0.5, where velocities are low due to the nature of an atmospheric boundary layer. Nonetheless, these small deviations still allow for the assumption of Reynolds Number independence.

The skewness of the u-component distributions (u_{skew}) is displayed in figure 3.23. In line with the results presented above, all profiles are very close. As observed for TKE the profile corresponding to $Re = 23428$ shows slight deviations from the other profiles. Again the same explanation can be applied.

A normalised mean squared error is used to quantify the differences between the profiles (equation 3.12). The highest velocity is used as the reference case.

$$NMSE_{\hat{X}} = \frac{100}{N \cdot \sigma_{\hat{X}}} \sum_{i=1}^{N} (\hat{X} - X)^2 \tag{3.12}$$

where $\hat{X}$ is the data and X represents the reference data, N is the sample size, $\sigma_{\hat{X}}$ is the standard deviation of the data and i is a running index. The result is given in % of the reference data.

Figure 3.24 below shows clearly that the turbulence behind an actuator disc model of a wind turbine is Reynolds Number independent for the tested range of Reynolds numbers, as the deviations are never greater than 0.3%. Even at low Reynolds numbers there are no significant deviations. This is in line with other literature (Mohamed and Larue, 1990) regarding Reynolds number independence of grid induced turbulence. An implication of this result is that Re can be varied as necessary when using an actuator disc model, giving more freedom for planning wind tunnel experiments.

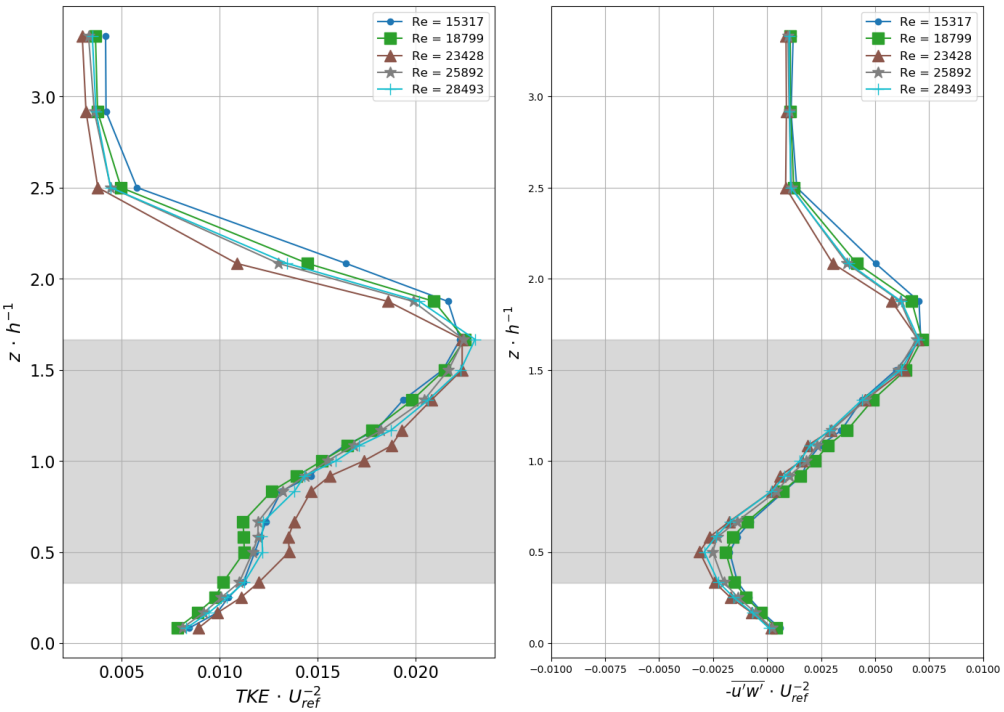

Figure 3.22 – Vertical profile of the turbulent kinetic energy (TKE, left) and the Reynolds stresses ($-\overline{u'w'}$, right) at different Reynolds Numbers (Re). U_{ref} is the highest point measured in the profile. The height z is normalised around hub height h. The grey area indicates the rotor-swept area.

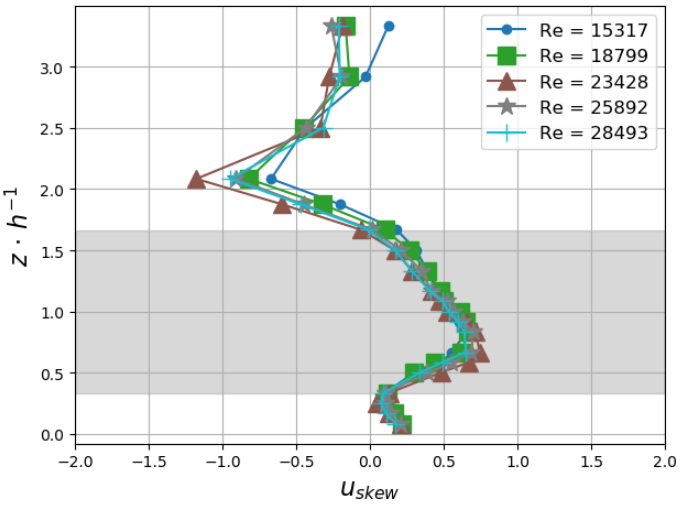

Figure 3.23 – Vertical profile of the skewness of the u-component at different Reynolds Numbers (Re). The height z is normalised around hub height h. The grey area indicates the rotor-swept area.

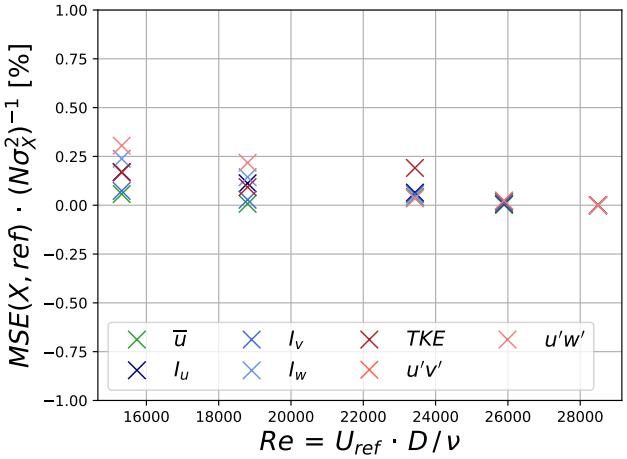

Figure 3.24 – Relative deviation measured using NMSE for all quantities tested for Reynolds number independence.

3.3.5 Uncertainty Estimation

This section discusses the uncertainty estimations for each measurement instrument. The underlying variability of inflow conditions is estimated using the reference wind velocity gathered during the PIV campaign as an example. To maintain a certain level of comparability between the respective uncertainties of the different measurement technologies, the standard error (SE) of the statistic x is calculated:

$$SE_{mean} = \frac{\sigma_x}{\sqrt{n}} \tag{3.13}$$

where σ is the standard deviation of the quantity x and n is the number of independent data points in equation 3.13. Extending this estimation to the standard deviation, assuming a normal distribution, results in the following:

$$SE_{\sigma} = \sqrt{\frac{\sigma_x}{\sqrt{n}}} \tag{3.14}$$

In order to indicate the range of accepted values the 99% confidence interval ($3\sigma_x$) is calculated and shown. To further maintain comparability the values for the standard deviation of the statistic are presented for boundary layer measurements only. The boundary layer is chosen as the reference case because it indicates the base uncertainty in the undisturbed flow. To gain a more complete image of the uncertainty of a given measurement the measurement uncertainty of the respective measurement technology is also given.

The Cobra probes measurement uncertainty is $\pm 0.3\, ms^{-1}$ and $\pm 1°$ according to the manual (Turbulent Flow Instruments, 2015). Considering the range of Cobra probes available this is acceptable when using top-of-the-range equipment capable

of measuring up to $100\,ms^{-1}$. At low velocities of around $2\,ms^{-1}$, or the bottom of the range, $\pm 0.3\,ms^{-1}$ seems excessive, as it represents a relative uncertainty of 15%. There is no mention of a relative error in the documentation. The standard error for the means and standards deviations measured with the Cobra probe are small (see table 3.6). These statistical uncertainties show that the Cobra probe delivers reliable data, despite its significant measurement uncertainty at the expected velocities of between $2\,ms^{-1}$ and $4\,ms^{-1}$.

The PIV system delivers similarly reliable data to the other measurement technologies presented here (table 3.6). The standard errors are in the same order of magnitude for the mean quantities ($\pm 0.004\,ms^{-1}$). The corresponding standard deviations vary between $\pm 0.016\,ms^{-1}$ and $\pm 0.037\,ms^{-1}$. Both standard errors are small, thus indicating reliable data sets.

The hot-wire anemometers deliver equally reliable data. The measured mean velocity has a standard error of $\pm 0.002\,ms^{-1}$. The SE_σ is calculated to be $\pm 0.046\,ms^{-1}$. This is in line with the values calculated for the other measurement technologies used in the scope of this thesis.

The variability of the inflow conditions is discussed based on the data gathered during the PIV campaign because it spanned two distinct seasons, summer and autumn. The effect of varying weather conditions is thus clearer than for the other campaigns that were carried out in one season. For the variability of the inflow conditions for the PIV measurements a total of 12 reference measurements are used for the following calculations. The mean inflow velocity for all measurements is $3.74\,ms^{-1} \pm 0.09\,ms^{-1}$. The maximum reference velocity measured is $3.89\,ms^{-1}$ or 4% above the mean. The minimum value is $3.63\,ms^{-1}$ or 3% below the mean. As the variability of the reference velocities is around 7%, the same level of variability can be assumed when comparing PIV data-sets.

To conclude, all three measurement technologies deliver reliable data with comparable standard errors. The variability of the inflow is larger than any of the measurement uncertainties. As this is the largest uncertainty, the variability of the inflow is taken as the measure for uncertainty in this thesis. Using the knowledge of uncertainties related to the acquired data and having demonstrated the quality of the inflow conditions, it is now possible to prepare a detailed measurement plan with the respective test set-ups.

Table 3.6 – The standard error for the statistics measured by the Cobra probe, PIV system and hot-wires used in this thesis (U, V, W σ_u, σ_v, σ_w). n is the number of independent samples and x/D indicates the location of the measurement. The standard deviation of the respective statistic is calculated. All standard deviations are estimated at hub height.

x/D	**n**	**U** $[ms^{-1}]$	**V** $[ms^{-1}]$	**W** $[ms^{-1}]$	σ_u $[ms^{-1}]$	σ_v $[ms^{-1}]$	σ_w $[ms^{-1}]$
Cobra							
4.6	1579	±0.015	±0.009	±0.007	±0.004	±0.002	±0.001
PIV							
3.5	4499	±0.004	±0.003	±0.002	±0.035	±0.026	±0.019
4.6	4499	±0.004	±0.003	±0.002	±0.037	±0.028	±0.021
7.0	8999	±0.003	±0.002	±0.001	±0.029	±0.021	±0.016
Hot-wire							
4.6	13592	±0.002	-	-	±0.046	-	-

3.4 Measurement Plan & Test Set-ups

This section describes and motivates the measurement plan designed to study the far wake of an FOWT in an atmospheric boundary layer wind tunnel. Information about turbulent quantities, spectra as well as spacial and temporal characteristics of the far wake is sought. As it is complicated to measure highly resolved temporal and spacial characteristics at the same time, the measurement plan is comprised of three parts.

To gain a first understanding of which Dof to investigate, numerically modelled motion data of FLOATGEN is studied. The data is provided by BW Ideol. To choose the Dof to investigate first, the respective motion's amplitudes are analysed. As surge, or longitudinal, motion has the largest amplitudes, it is selected to begin the investigation. This case represents head-on wind and waves. The other Dofs of significance in this thesis are heave (D_z) and pitch (R_y), which also represent cases of head-on wind and waves. Sway (D_y, non-aligned wind and waves) is also investigated, but in less detail.

As the motion systems do not limit the modelling of the FOWT's motion significantly, a wide range of motion regimes can be determined. The motion's amplitude and frequency are set in the order of single digit Hz and double digit mm (see section 3.1.2). The characteristic frequency of surge motion is determined to be $2\,Hz$ with an amplitude of $20\,mm$. Expressed as a reduced frequency (see equation 2.14) this equates to $f_{red} = 0.1$ and a normalised length $0.125\,D$.

The frequency is varied systematically from $1\,Hz$ to $7.5\,Hz$., while keeping the amplitude constant. The frequencies at $3.75\,Hz$, $5.5\,Hz$ and $7.5\,Hz$ result from an estimation of the characteristic frequency of the boundary layer flow ($\approx 7.5\,Hz$). The aim is to establish whether excitation at fractions of or at the characteristic

frequency leads to additional instability in the wake. The approach is similar for heave and pitch motions. These Dofs have characteristic frequencies of $3\,Hz$ and $2.5\,Hz$ and amplitudes of $2\,mm$ and $2°$, respectively. The frequencies are only varied at higher than characteristic frequencies, as the lower than characteristic frequencies have little measurable effects on the wake.

In order to isolate the effects of varying the amplitude on the wake, several steps are necessary. The process is most easily described using the reduced frequency. The goal is to keep f_{red} constant while varying the amplitude of the motion. As the travel speed of the mast must not be changed to avoid possible additional effects of the modified velocity of the model (like modified energy entrainment), the frequency of the motion must be adapted as a function of the amplitude. To maintain f_{red} constant the ratio of f and U_{ref} must be maintained. This implies that a larger amplitude requires a higher frequency and a higher flow velocity, thus limiting the largest amplitude that can be studied. Respecting these relationships, amplitudes of $30\,mm$ and $40\,mm$ are selected to be investigated. The corresponding frequencies are $3\,Hz$ at $U_{ref} = 6.9\,ms^{-1}$ and $4\,Hz$ at $U_{ref} = 8.4\,ms^{-1}$, respectively.

3.4.1 1^{st} Measurement Campaign - Cobra Probe

The first part is a parametric study investigating the effects of imposed surge motion. The parameters that are varied are the frequency and the amplitude of the motion (see table 3.7). The reference case is a fixed turbine model. Profile and spectra measurements are conducted. Each point in a profile is measured for five minutes as dictated by the convergence time (see section 3.3.3). The measurement time for spectra is set to 30 minutes to capture low frequency events reliably. The profiles and spectra are measured $4.6\,D$ downstream of the model using the Cobra probe exclusively.

The Dofs investigated are surge (D_x) and, to a lesser extent, sway (D_y). Sway, or lateral, motion is studied by turning the motion system by 90° and applying the same motion characteristics as for surge. This emulates conditions where wind and waves are offset by 90°. The waves come from a side, while the wind blows head-on. Sway motion can be also encountered by an FOWT because marine waves tend to be three dimensional and interactions between currents, the floater and the mooring lines are possible. Figure 3.25 shows the test set-up for the surge campaign. The wake can be measured up to a height of $z/h \approx 3$.

Table 3.7 – Measurement plan for the parametric study where the amplitude and frequency of the motion are varied. Profiles and spectra are measured $4.6\,D$ downstream from the model using the Cobra probe.

Dof	**Frequency/f_{red}**	**Amplitude**
no disc		
fixed	$0\,Hz$	$0\,mm$
D_x	$1\,Hz/0.05$	$20\,mm/0.125$ D
D_x	$2\,Hz/0.1$	$20\,mm/0.125$ D
D_x	$3\,Hz/0.15$	$20\,mm/0.125$ D
D_x	$3.75\,Hz/0.18$	$20\,mm/0.125$ D
D_x	$5.5\,Hz/0.27$	$20\,mm/0.125$ D
D_x	$6\,Hz/0.29$	$20\,mm/0.125$ D
D_x	$7.5\,Hz/0.36$	$20\,mm/0.125$ D
D_x	$3\,Hz/0.1$	$30\,mm/0.1875$ D
D_x	$4\,Hz/0.1$	$40\,mm/0.25$ D
D_x	real	real
D_y	$1\,Hz/0.05$	$20\,mm/0.125$ D
D_y	$2\,Hz/0.1$	$20\,mm/0.125$ D
D_y	$3.75\,Hz/0.18$	$20\,mm/0.125$ D
D_y	$5.5\,Hz/0.27$	$20\,mm/0.125$ D
D_y	$7.5\,Hz/0.36$	$20\,mm/0.125$ D
D_y	$1\,Hz/0.1$	$40\,mm/0.25$ D
D_y	$1.33\,Hz/0.1$	$40\,mm/0.25$ D

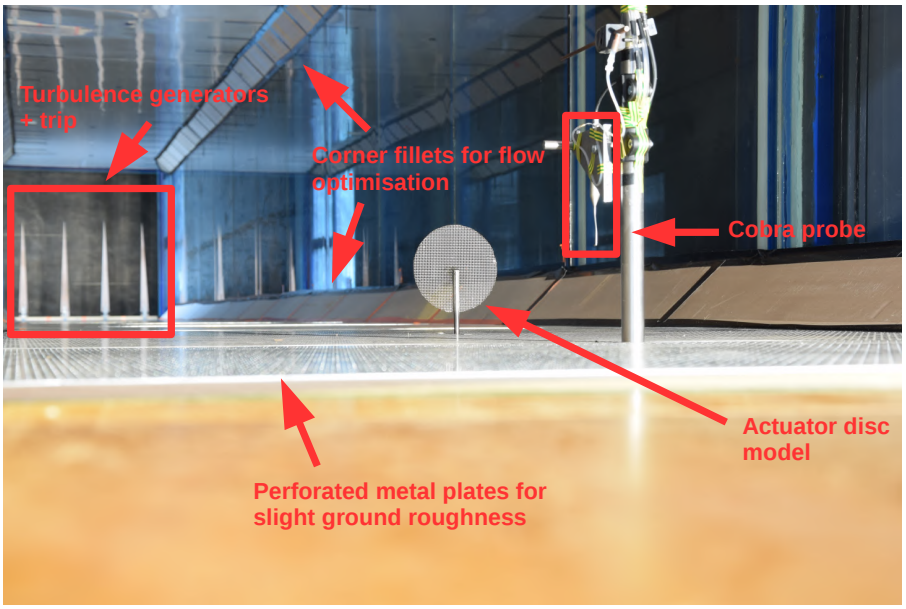

Figure 3.25 – Photo of the set-up in the Centrale Nantes atmospheric wind tunnel for all vertical profiles.

3.4.2 2^{nd} Measurement Campaign - S-PIV

The second measurement campaign is designed to gather information on the spatial development of the wake. To achieve this S-PIV is employed. The overall area in the wake covered by PIV measurements is between $0.5\,D$ and $8\,D$, while the area analysed is between $3\,D$ and $8\,D$. This is done to be able to visualise the development on the wake from the earliest possible state. The data is used to calculate the turbulent kinetic energy (TKE) budget in the turbine's wake. A boundary layer measurement and the reference case measurement are carried out. Using the knowledge gained from the first parametric study three motion regimes are investigated. These are chosen to be as realistic as possible with idealised motion in D_x (see table 3.8). The cases have to be limited due to the large amount of data generated when using S-PIV technology.

As figure 3.26 shows, the wake is investigated up to a distance of $\approx 8\,D$ from the actuator disc. As the entire distance cannot be covered by one pair of cameras the area is split into four sections, each roughly $2\,D$ wide and $1.75\,D$ high. This results in separate measurements for $0.5\,D - 2.5\,D$, $2.5\,D - 4.5\,D$, $4.5\,D - 6.5\,D$ and $6.5\,D - 8.0\,D$. As a certain amount of overlap is incorporated into the positioning, the actual locations vary marginally. The entire area covered is indicated by the green dashed line in figure 3.26. The laser illuminates the flow along the centre line of the actuator disc. The cameras are mounted at an angle so that they can be placed on the same side of the wind tunnel, simplifying the calibration process, as they can use the same calibration target, thus saving time. Calibration is necessary every time the cameras are moved. The cameras used are mounted on a rail next to the wind tunnel to facilitate moving the cameras to the positions required for each

Table 3.8 – Measurement plan for the S-PIV measurements. Three surge motion regimes are investigated. The spatial wake development is studied between $0.5\,D$ and $\approx 8\,D$.

Dof	**Frequency/f_{red}**	**Amplitude**
BL		
fixed	$0\,Hz$	$0\,mm$
D_x	$1\,Hz/0.05$	$20\,mm/0.125$ D
D_x	$2\,Hz/0.1$	$20\,mm/0.125$ D
D_x	$3.75\,Hz/0.18$	$20\,mm/0.125$ D

measurement. The laser is moved to provide the best illumination possible at each position. The laser is mounted to a traverse system. The traverse system can move the laser precisely along the wind tunnel's longitudinal axis, following the actuator disc's centre line. A Cobra probe and a pitot tube measure wind velocity at hub height.

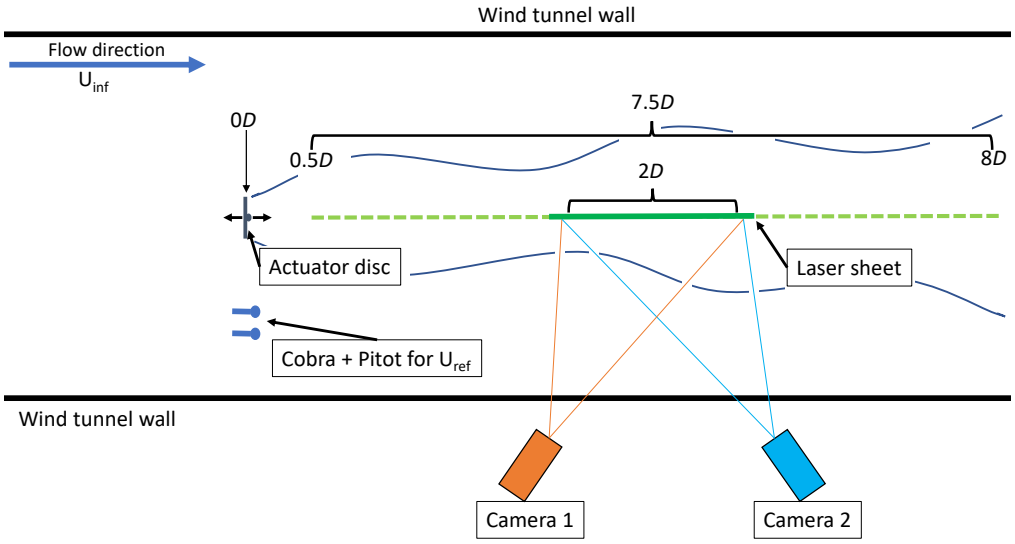

Figure 3.26 – Sketch of an example test set-up for S-PIV measurements. The green dashed line represents the entire length of the area investigated using the stated technology. Two cameras are necessary to reconstruct the third velocity component (y in this experiment).

3.4.3 3^{rd} Measurement Campaign - Hot-wire Anemometry

The third measurement campaign aims to characterise the unsteady wake characteristics when the model is subjected to several degrees of freedom. In order to keep the analysis as straight forward as possible, each Dof (surge, heave, pitch) is analysed separately before they are combined. Idealised and "real" motion profiles

are applied for the single and multiple Dof motion regimes (see table 3.9). A notion of such a "real" motion profile can be gained from figure 3.27.

Table 3.9 – Measurement plan for the second parametric study investigating single and three Dof motion. The aim is to investigate unsteady phenomena in the wake at $4.6\,D$ and $8\,D$. Hot-wire anemometry is used. The $\sum$ indicates that the 3 Dof motion is comprised to the three preceding entries in the table. All values are shown with their dimensions and the corresponding non-dimensional values.

Case	**Surge**	**Heave**	**Pitch**	**3 Dof**
1	$0.1/0.125\,D$	$0.14/0.0125\,D$	$0.12/2°$	$\sum$
2	$0.18/0.125\,D$	$0.19/0.0125\,D$	$0.18/2°$	-
3	$0.27/0.125\,D$	$0.28/0.0125\,D$	$0.24/2°$	-
4	$0.1/0.25\,D$	$0.14/0.03125\,D$	$0.12/5°$	-
5	-	$0.14/0.0625\,D$	$0.12/8°$	-
"real"	X	X	X	$\sum$

The measurements are conducted using hot-wire anemometry. The Cobra probe is employed to measure the undisturbed flow at hub height outside of the wake. A pitot tube measures the flow velocity in the free flow. Apart from the motion regimes, data on the boundary layer and the reference case is acquired.

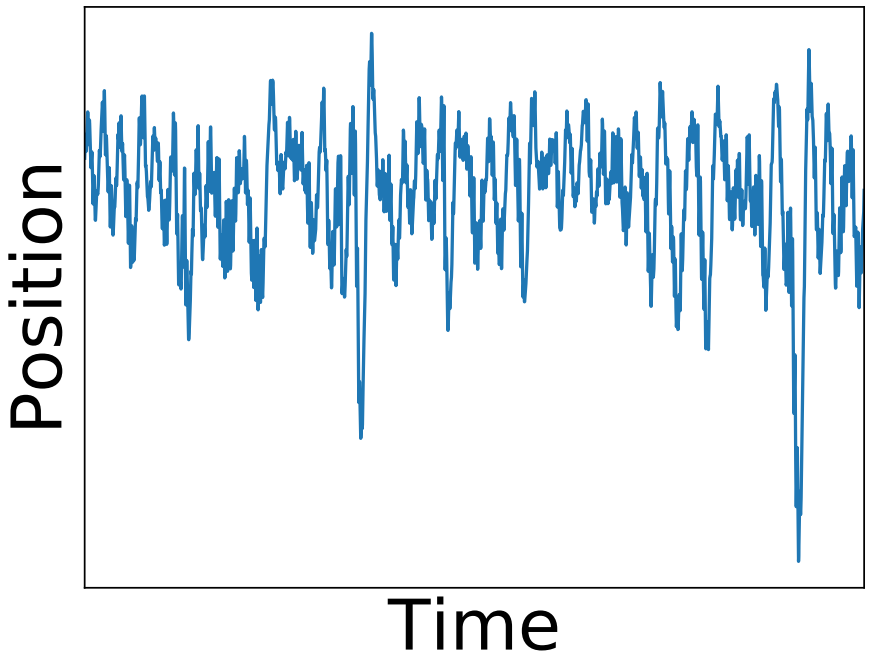

Figure 3.27 – Sketch of a "real" motion series as used in this work.

The set-up of the 3 Dof campaign uses a rake of 10 hot-wire anemometers,

arranged in a cross. A Cobra probe functions as a reference measurement to the right of the rake, facing downstream. The rake is positioned $4.6\,D$ and then $8\,D$ downstream of the actuator disc (see figure 3.28). The hot wires are calibrated regularly in the free stream of the wind tunnel using a special support put in place specifically for this purpose. The box holding the 3 Dof motion system is tested for air-tightness on a regular basis.

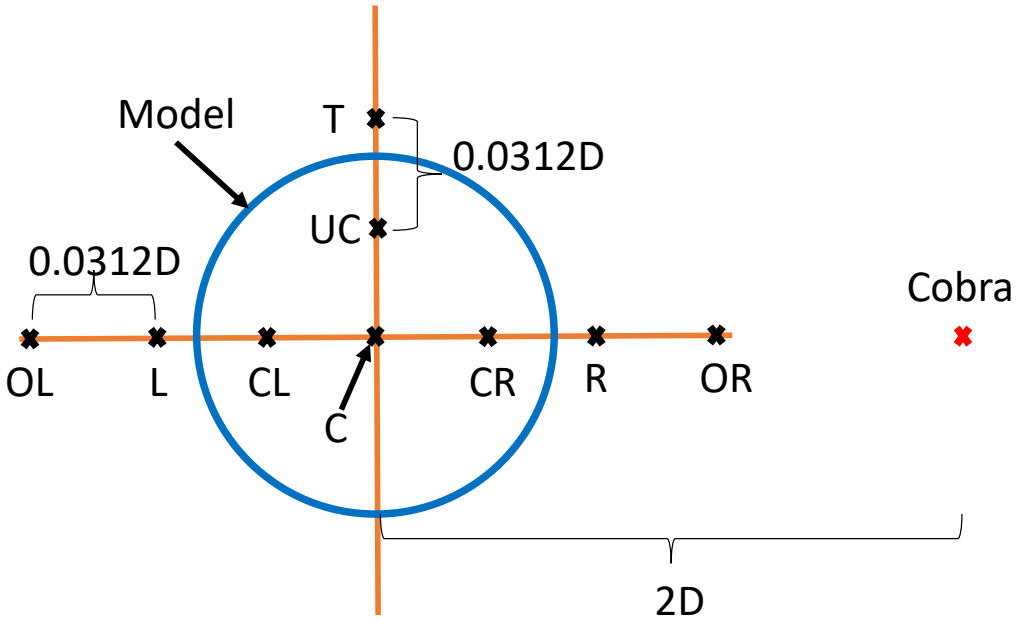

Figure 3.28 – Sketch of the set-up used during hot-wire measurements. The letters indicate the measurement positions for future reference. OL: outer left, L: left, CL: centre left, C: centre, CR: centre right, R: right, OR: outer right, UC: upper centre, T: top.

3.4.4 Preliminary Conclusions

Representative results can be assumed when taking into account all the above mentioned tests and processes. The quality checks presented in this chapter serve the purpose of ensuring representative and good quality data. The statistical uncertainty of the wind tunnel data is estimated at $\pm 0.015\,ms^{-1}$ for data measured with the Cobra probe, $\pm 0.004\,ms^{-1}$ for the S-PIV data, and $\pm 0.002\,ms^{-1}$ for the data acquired with the hot-wire anemometers. The overall variability of the inflow conditions is estimated to be around 7%. This uncertainty of results is shown for each result originating from the respective equipment used in this study. The results of the methodology described here are presented in the next chapter.

Chapter 4

Discussion of Results

In this chapter the results of three measurement campaigns presented in section 3.4 are discussed. First, vertical profiles of mean and turbulent quantities in the wake of an FOWT model under imposed surge motion are presented at a downstream distance of 4.6 D. Second, the analysis is extended downstream up to $8\,D$ in order to assess the effects of imposed surge motion on the wake's development. This part includes a discussion of the TKE budget in the wake of the FOWT model. A brief discussion of the effects of sway motion follows. Finally, the unsteady wake characteristics are analysed. 1 Dof (surge, heave, pitch) as well as 3 Dof motion, which is composed of simultaneous surge, heave and pitch motion, is presented in detail. The impact of sway motion is also discussed, but to a lesser extent. To get an overview of the recurring quantities studied in the following, these will be presented first.

4.1 Mean and Turbulent Quantities

To understand the effects that imposed idealised surge motion has on the wake of a modelled FOWT, a selection of mean and turbulent quantities are employed. They are the mean flow velocity U, V or W, the turbulence intensity I, the turbulent kinetic energy TKE and the lateral and vertical shear stresses $\overline{u'v'}$ and $\overline{u'w'}$. These quantities are defined in the following. All these quantities are widely used in the field of fluid mechanics.

The turbulence intensity, a measure for the variability in the flow, is defined as:

$$I_x = \frac{\sigma_x}{U} \tag{4.1}$$

where σ_x is the standard deviation of the flow component x and U is the local mean flow velocity magnitude.

The TKE represents the amount of kinetic energy that can be attributed to

turbulent processes. It is defined as follows:

$$TKE = 0.5 \cdot \left(\sigma_u^2 + \sigma_v^2 + \sigma_w^2\right) \tag{4.2}$$

where σ is the standard deviation of the respective flow component.

Turbulent Reynolds shear stresses (τ) are generally defined as the mean product of the instantaneous deviation of the flow components:

$$\tau_x = \overline{x'y'} \tag{4.3}$$

where x' and y' are the instantaneous deviations from the mean of any of the flow components (u, v or w). The bar represents a temporal average. The shear stresses describe the strain induced by the surrounding flow on a given part of the flow.

Using these quantities, it is possible to obtain a first understanding of the processes affected by induced surge motion in the wake of an FOWT. To this avail vertical profiles of the different quantities measured at $4.6\,D$ are presented. A more in depth analysis of the physical processes follows, by means of a TKE budget analysis.

4.2 Effects of Surge Motion on the Mean Wake

In the following section, the effect of surge motion on the mean wind profile and turbulent kinetic energy (TKE) profile is described at $x = 4.6\,D$ downwind of the wind turbine model. Idealised sinusoidal motion at reduced frequencies (f_{red}) around $f_{red} = 0.10$ with amplitudes varied around $0.125\,D$ are imposed on the model. In order to test the effects of changes in frequency or amplitude on the investigated quantities, a parametric study with frequency and amplitude as variables is carried out. When the effects of frequency changes are investigated the amplitude is fixed at $A = 0.125\,D$ and the reduced frequency is varied. In the case of amplitude changes, $f_{red} = 0.10$ is not changed and the amplitude of the motion is varied. f_{red} is calculated using the following equation:

$$f_{red} = \frac{f \cdot D}{U_{ref}} \tag{4.4}$$

where f is the input frequency, D is the wind turbine model's diameter and u_{ref} is a reference wind velocity, in this study the highest point of each profile. Depending on the test set-up the reference wind velocity is

varied between $U_{ref} \approx 3.5\,ms^{-1}$ and $U_{ref} \approx 8\,ms^{-1}$. Turbulence intensity variations are calculated as follows:

$$\Delta I_x = I_{x_{motion}} - I_{x_{fixed}} \tag{4.5}$$

where $I_{x_{motion}}$ is the turbulence intensity calculated for a turbine subjected to motion and $I_{x_{fixed}}$ in the fixed turbine case.

4.2.1 Vertical Profiles

The introduction of idealised sinusoidal surge motion with varying amplitudes or frequencies to the wind turbine model does not significantly change the shape of the mean velocity profiles, compared to a fixed turbine's profile (figure 4.1 and figure 4.2, left hand panels). $f_{red} = 0.24$ delivers slightly increased mean velocity values beneath $z = 1$. With regard to TKE the characteristic motions ($A = 0.125\,D$, $f_{red} = 0.05$, $f_{red} = 0.10$ and $f_{red} = 0.18$) all show decreases compared to the fixed case (black line/crosses) in the area blocked by the turbine (grey area). In the more extreme cases of $A = 0.25\,D$ and $f_{red} = 0.24$, local increases in TKE can be observed (figure 4.1 and 4.2, right hand panels).

In order to understand the modified TKE profiles, the turbulence intensity I_x of each velocity component is studied. The variations of turbulence intensity ($\Delta\, I_x$) profiles for constant f_{red} are presented in figure 4.3. The turbulence intensity of the longitudinal component I_u displays an increased spread between the different cases beneath z=h, with $A = 0.125\,D$ showing minor losses, $A = 0.31\,D$ is mostly unchanged, $A = 0.25\,D$ displaying a slight gain compared to the reference case. This is in line with the observations made in the corresponding TKE profile. This pattern is inverted between $z = 1.5\,h$ and $z = 2.5\,h$. I_v shows a very similar behaviour to the reference case for all measurements. This is to be expected as the surge motion does not have a lateral component. The vertical turbulence intensity (I_w) profile shows losses throughout the profile. The highest losses of I_w are observed for $A = 0.125\,D$ below $z = 1$. Changes in the $A = 0.25\,D$ and $A = 0.31\,D$ profiles are minor compared to the reference case. The tendency to marginal losses in all components can be noted.

Varying f_{red} shows a similar trend to lower turbulence intensities for all velocity components for the characteristic cases ($0.05 \leq f_{red} \leq 0.15$). As can be seen in figure 4.4 the turbulence intensity profiles for all f_{red} for I_u, display losses. The largest reductions occur between $z = 0.5\,h$ and $z = h$. For I_v reduced frequencies below $f_{red} = 0.18$ lead to reduced turbulence intensities. $f_{red} = 0.24$ shows marginal increases in I_v. Similarly,

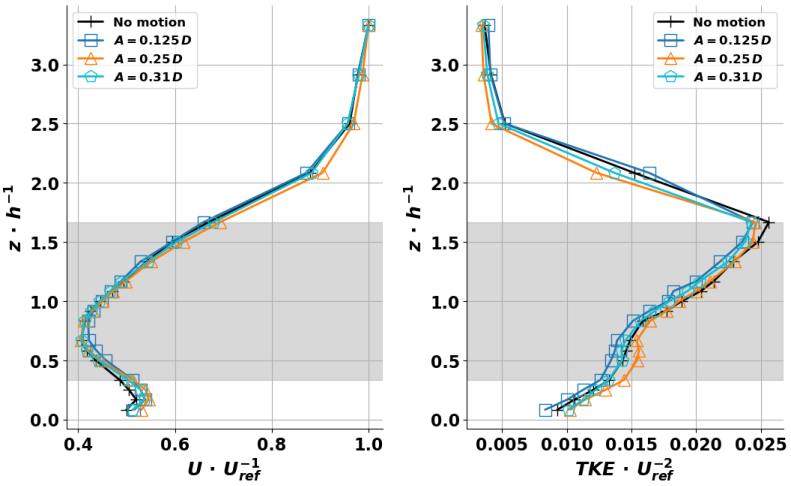

Figure 4.1 – Vertical profiles of the mean normalised velocity (U) and normalised turbulent kinetic energy (TKE). Case: Constant reduced frequency ($f_{red} = 0.10$), varying amplitudes. Measured $4.6\,D$ downstream of the actuator disc. Reprinted from Schliffke et al. (2020). ©The Authors.

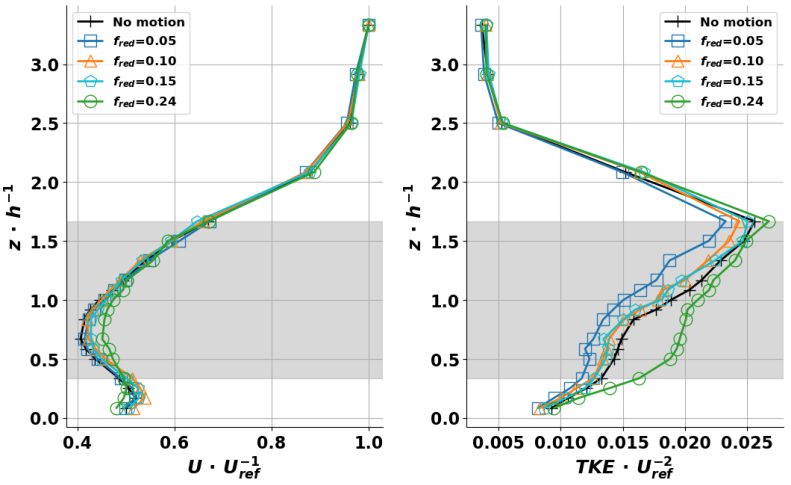

Figure 4.2 – Vertical profiles of the mean normalised velocity (U) and normalised turbulent kinetic energy (TKE). Case: Constant amplitude ($A = 0.125\,D$), varying f_{red}. Measured $4.6\,D$ downstream of the actuator disc. Reprinted from Schliffke et al. (2020). ©The Authors.

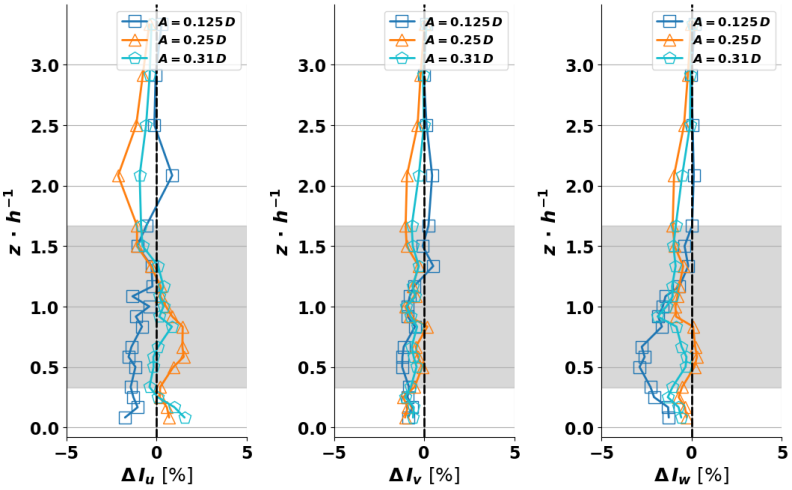

Figure 4.3 – Vertical profiles of the turbulence intensity of each velocity component. Constant reduced frequency (f_{red}), varying amplitudes. Measured 4.6 D downstream of the actuator disc. Reprinted from Schliffke et al. (2020). ©The Authors.

$f_{red} = 0.24$ shows increased I_w in the bottom half of the profile, whereas all other f_{red} show a decrease in I_w. Again, $f_{red} = 0.05$ displays the largest reduction in I_w compared to a fixed turbine. It can be concluded that the gains in the TKE profile observed for $f_{red} = 0.24$ in figure 4.2, can be related to the gains in the w component's turbulence intensity seen in figure 4.4. For the other cases, decreases in TKE and turbulence intensity do not affect the mean velocity in a discernible manner.

In addition to the results presented in Schliffke et al. (2020) the $\overline{u'v'}$ and $\overline{u'w'}$ stresses are discussed briefly here. The influence of varying f_{red} at constant amplitudes is studied first. $\overline{u'v'}$ is consistently near zero for all f_{red}, as expected. The Reynolds stresses ($\overline{u'w'}$) depicted in the right hand panel show decreased (i.e. closer to 0) stresses beneath hub height compared to the fixed turbine case. Above hub height all profiles are very similar.

When varying the amplitude of the motion, the $\overline{u'v'}$ and $\overline{u'w'}$ show inconsistent behaviour (figure 4.5). At $A = 0.125\,D$ $\overline{u'v'}$ (orange) is similar to the fixed turbine case. At $A = 0.25\,D$ $\overline{u'v'}$ is increased (red), while at $A = 0.312\,D$ it has changed sign (green, left hand panel). As depicted in the right hand panel of figure 4.5, $\overline{u'w'}$ displays a similar behaviour to $\overline{u'v'}$. One profile is similar to the fixed turbine case ($A = 0.312\,D$), while one shows increased stresses beneath hub height ($A = 0.25\,D$) and the other displays reduced $\overline{u'w'}$ in the same area ($A = 0.125\,D$). At the top tip, all motion regimes show marginally decreased values for $\overline{u'w'}$.

It can be concluded that imposed characteristic surge motion has limited effects on the mean and turbulent quantities in the wake at 4.6 D. In order to see any effects it is necessary to employ frequencies of $f_{red} = 0.24$ or greater. The reduced turbulence intensity and TKE found in the profiles described above, indicate that the wake recovery process is enhanced mildly. These findings have been confirmed

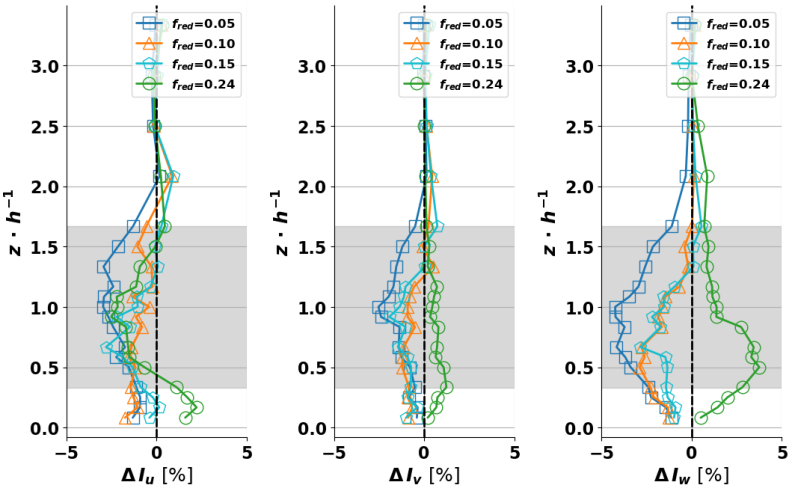

Figure 4.4 – Vertical profiles of the turbulence intensity of each velocity component. Constant amplitude, varying f_{red}. Measured 4.6 D downstream of the actuator disc. Reprinted from Schliffke et al. (2020). ©The Authors.

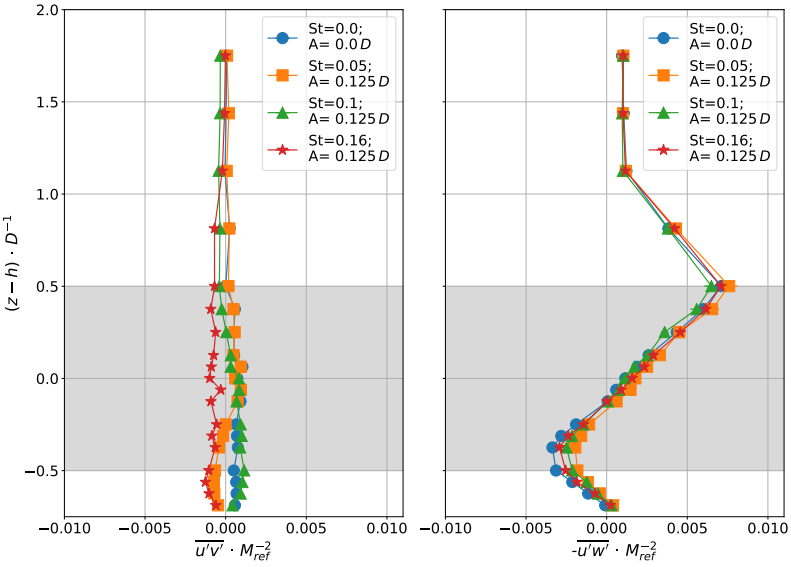

Figure 4.5 – Vertical profiles of the $\overline{u'v'}$ and $\overline{u'w'}$ stresses. Case: Constant travel velocity, varying amplitudes. Measured 4.6 D downstream of the actuator disc when subjected to surge motion.

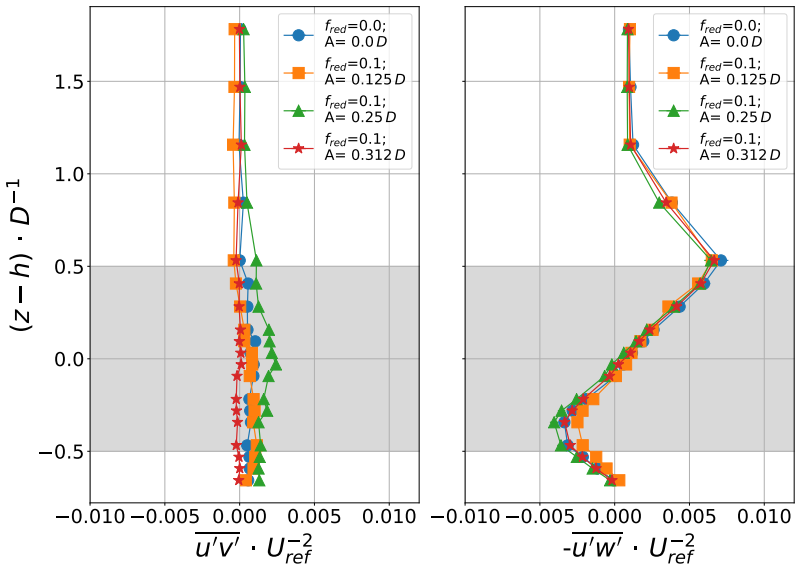

Figure 4.6 – Vertical profiles of the $\overline{u'v'}$ and $\overline{u'w'}$ stresses. Case: Constant travel velocity, varying amplitudes. Measured 4.6 D downstream of the actuator disc when subjected to surge motion.

by other studies using different test set-ups (Fu et al., 2019; Fontanella et al., 2021). Concerning the stresses investigated above, it is difficult to draw any meaningful conclusions as there are no significant or systematic changes for either $\overline{u'v'}$ or $\overline{u'w'}$ in any of the cases tested. In an attempt to explain these results PIV measurements of wake are carried out to gain a better understanding of the spatial characteristics of the wake of an FOWT. The corresponding results are presented in the next section (section 4.2.2).

4.2.2 The Wake's Spatial Characteristics

In this section the spatial characteristics of the wake of a modelled floating wind turbine are presented. The focus will be on the changes of a number of mean and turbulent quantities (velocity deficit, wake-added turbulence and TKE as well as changes in $-\overline{u'w'}$ compared to the BL) when the turbine is subjected to surge motion frequencies of $f_{red} = 0.05$, $f_{red} = 0.1$ and $f_{red} = 0.18$. Before looking into the results it is necessary to understand the limitations on the comparability of the S-PIV data. In order to keep the motion as close to the characteristic motion regime as possible $f_{red} = 0.25$ is not investigated any further, in the context of the PIV measurements.

A Note on Comparability

Figure 4.7 shows a comparison of the different BL measurements taken in the course of the S-PIV campaign. The orange ($x \cdot D^{-1} = 3$), blue ($x \cdot D^{-1} = 4.6$) and purple ($x \cdot D^{-1} = 7$) data show the mean normalised velocity profiles calculated from the respective S-PIV data sets (left hand panel). The right hand panel shows the corresponding standard deviation σ_u. Each profile represents a longitudinal average

over about $0.16\,D$. The red data is the BL measurement used to characterise the boundary layer. The shaded areas indicate the uncertainty of the respective data.

It is evident from figure 4.7 that the boundary layer flows vary significantly between the different measurements. While the velocity profiles at $x \cdot D^{-1} = 3$ and $x \cdot D^{-1} = 7$ are only offset from the Cobra data, the S-PIV velocity profile at $x \cdot D^{-1} = 4.6$ is markedly different. The profile at $x \cdot D^{-1} = 4.6$ appears to be in transition between the profiles at $x \cdot D^{-1} = 3$ and $x \cdot D^{-1} = 7$. These differences suggest a stronger dependence of the boundary layer flow on the ambient conditions than previously expected. This includes the layout of other equipment in the wind tunnel hall and the changing weather conditions. The turbulence intensity of the flow seems to be less affected considering the right hand panel in figure 4.7. Here the Cobra probe's underestimation of the variability at low flow velocities can most likely explain the consistently lower σ_u compared to the S-PIV data. The profiles are comparable above hub height. Solely the profile at $x \cdot D^{-1} = 4.6$ diverges between hub height and the bottom tip.

These observations lead to limitations in the comparability of the different data sets. The data measured between $x \cdot D^{-1} = 2$ and $x \cdot D^{-1} = 4$ can not necessarily be compared to the data measured between $x \cdot D^{-1} = 4$ and $x \cdot D^{-1} = 6$, which in turn can not be compared with the data from $x \cdot D^{-1} = 6$ to $x \cdot D^{-1} = 8$, i.e. the separate S-PIV measurement campaigns. The data not measured together, temporally, can not be compared in a reliable way as it is nearly impossible to normalise the data without severely modifying it. Practically, this means that the different motion frequencies at a given location can be compared, while any conclusions on the longitudinal evolution of the wake must be drawn with care, as the measurements at one location were made consecutively, thus limiting the effects of the varying ambient conditions. In the future, wind tunnel test campaigns at the LHEEA wind tunnel should take the seasonal variability of the BL flow into account and try to execute the campaigns in a timely compact manner.

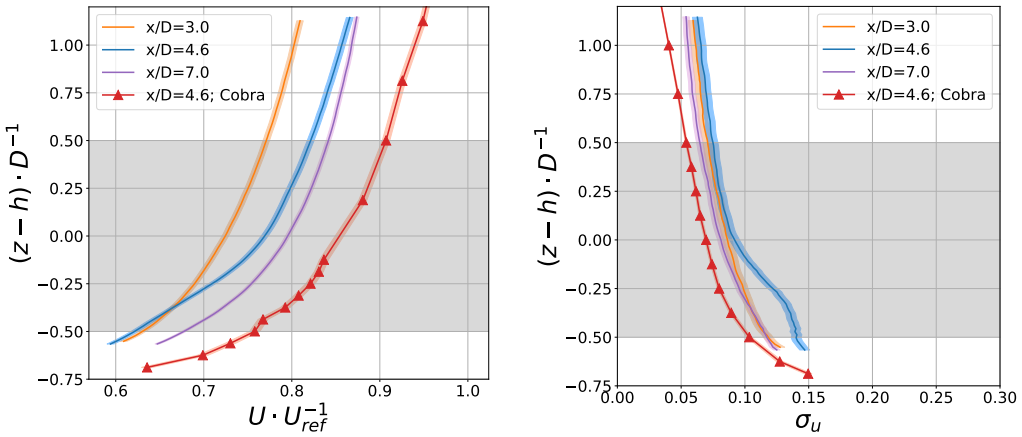

Figure 4.7 – Normalised mean longitudinal flow component U and its standard deviation in the BL flow measured during the PIV measurement campaign. The data acquired with the Cobra probe (red) is added for reference, measured in September. Orange: first measurement plane measured in September, blue: second measurement plane measured in mid October, purple: final measurement plane measured in late October. The shaded areas represent the statistical uncertainty for each measurement.

Results

Previous results showed that the mean values are not significantly influenced by the introduction of periodic surge motion on the porous disc (e.g. Schliffke et al., 2020; Fontanella et al., 2021). This tendency can also be seen in the stereoscopic PIV measurements presented below. Each panel in the following figures represents one S-PIV data-set. They are not combined to one large longitudinal figure due to the limitations described in section 4.2.2. The panels in the figures can thus only be compared within a given column. The x-axis represents the distance from the porous disc. This distance is normalised by D. The y-axis shows the height coordinates. These are given relative to the hub height and also normalised by D. The data is normalised using the mean velocity measured by the permanently installed pitot tube as the reference wind velocity (U_{ref}). The shaded area indicates the zone where the wake of a porous disc can not be assumed to be representative of a wind turbine wake ($x \cdot D^{-1} \leq 3$). The respective motion regime is noted in the right hand panel.

In figure 4.8 the wake deficit calculated for all motion regimes and the fixed turbine case is depicted. The wake deficit is the difference between the flow velocity in the wake and the undisturbed flow, in this case the boundary layer:

$$\Delta U = \frac{U_{motion}}{U_{ref}} - \frac{U_{BL}}{U_{ref}} \tag{4.6}$$

.

It can be observed that surge motion has little effect on the overall wake deficit. The maximum longitudinal expansion of the -0.25 wake deficit area varies between

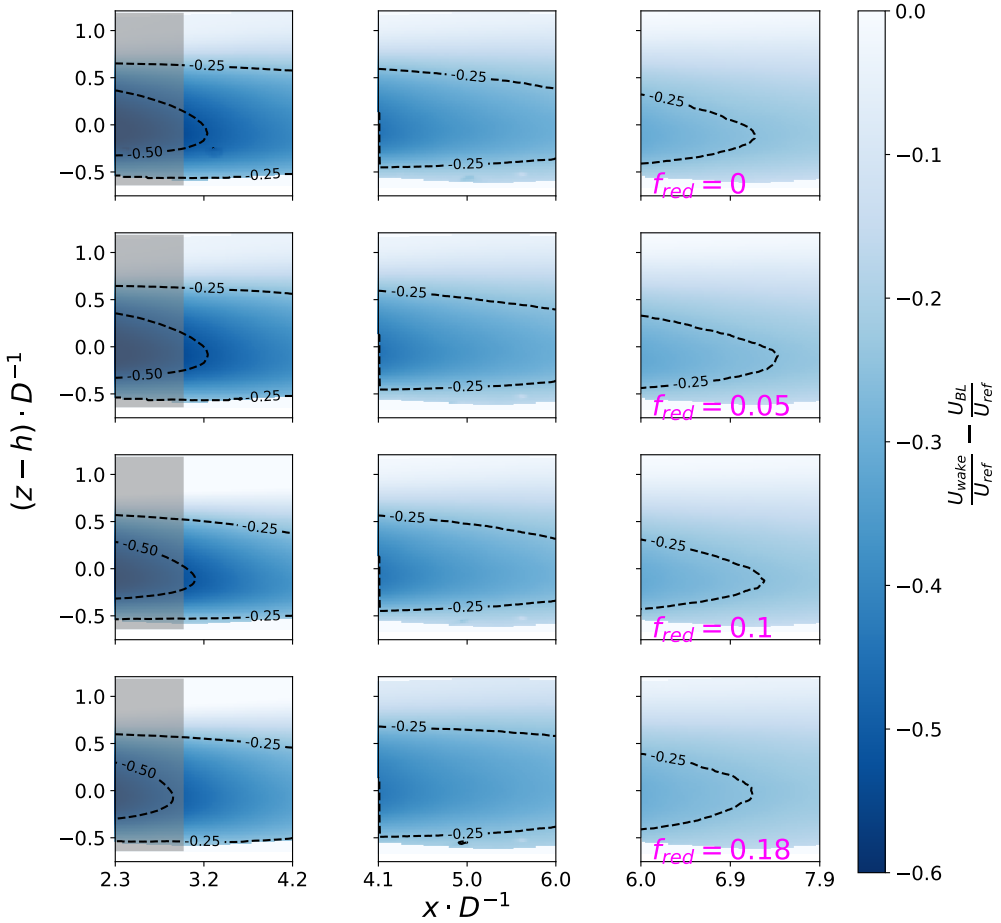

Figure 4.8 – Wake deficit of the model turbine. Each panel represents one S-PIV data-set. Rows show the longitudinal development of the wake for $2.3 < x \cdot D^{-1} < 7.9$, with different motion regimes imposed ($f_{red} = 0$, $f_{red} = 0.05$, $f_{red} = 0.1$, $f_{red} = 0.18$). The distance from the model is normalised by D (x-axis). The height coordinates on the y-axis are normalised around hub height relative to the disc diameter (D). Shaded area: $x \cdot D^{-1} \leq 3$.

$7.16\,D$ and $7.44\,D$ (right hand column). The maximum longitudinal extension of $7.44\,D$ is related to the $f_{red} = 0.05$ motion regime. With higher frequencies, the maximum longitudinal extension of the -0.25 wake deficit area retreats back to the initial range of $7.2\,D$ for the fixed turbine. In the near wake the -0.5 isoline retreats from $3.26\,D$ to $2.89\,D$ with increasing motion (left hand column). The central region of wake deficit between $4.1\,D$ and $6\,D$ (middle column) is not significantly affected by the introduction of surge motion.

Figure 4.9 shows the wake-added turbulence I_u (equation 4.1). The statistics of the data presented in top left panel have been found to be offset from all other data sets. This affects the turbulence intensity, TKE and the turbulent Reynolds stresses. Attempts to correct this by reprocessing the raw data did not lead to any significant improvements. The mean values and derivatives do not appear to be affected.

A slight shortening of the areas most affected by wake-added turbulence can be observed for $f_{red} = 0.18$. The longitudinal extent of the zone circumscribed by the 0.075 isoline is reduced by $0.42\,D$ compared to the fixed turbine (middle column). At the same time $f_{red} = 0.1$ delivers the largest area of wake-added turbulence, reaching to $5.11\,D$. The vertical thickness of the added turbulence layer above hub height increases from $0.63\,D$ for $f_{red} = 0.05$ to $0.78\,D$ for $f_{red} = 0.18$ for $x \cdot D^{-1} < 4.2$ (left hand column). The sum of I_u above $I_u = 0.075$ increases from 125 for $f_{red} = 0.05$ to 259 for $f_{red} = 0.18$. No clear effects of surge motion can be seen for $x \cdot D^{-1} > 6$ (right hand column).

The wake-added TKE is depicted in figure 4.10. The behaviour is similar to that described in figure 4.9. Surge motion appears to have limited effects on the overall extent of the wake-added TKE, though a slight shortening can be observed. The furthest longitudinal position of the 0.01 isoline moves back from $7.9\,D$ for the fixed turbine (so most likely outside of the measurement area) to $7.65\,D$ for $f_{red} = 0.18$ (right hand column). Similar behaviour to the development of the wake-added turbulence can be observed regarding the extent of the 0.015 isoline (middle column). The area extends longitudinally by $0.27\,D$ up to $f_{red} = 0.1$, while it is shortened by $0.46\,D$ for $f_{red} = 0.18$. The vertical extent of the added TKE within the 0.01 boundary also grows with increasing motion from 0.68 dimensionless units to 1.29 dimensionless units, most clearly seen for $f_{red} <= 0.15$ for $x \cdot D^{-1} < 4.2$ (left hand column). The sum of the wake-added TKE above 0.015 dimensionless units increases significantly from 13 dimensionless units at $f_{red} = 0.05$ to between 56 and 58 dimensionless units for $f_{red} = 0.1$ and $f_{red} = 0.18$, respectively. This is in line with observations made in Schliffke et al. (2020), where increased TKE was observed below hub height at a distance of $x \cdot D^{-1} = 4.6$.

In figure 4.11 the difference between the Reynolds stresses (equation 3.11) of the wake and the BL is shown. Imposed surge motion has some notable effects on the overall distribution of Re stresses within the wake. Surge motion of $f_{red} \geq 0.1$ leads to an increase in Reynolds stresses above 0.006 dimensionless units from 0.4 to 12

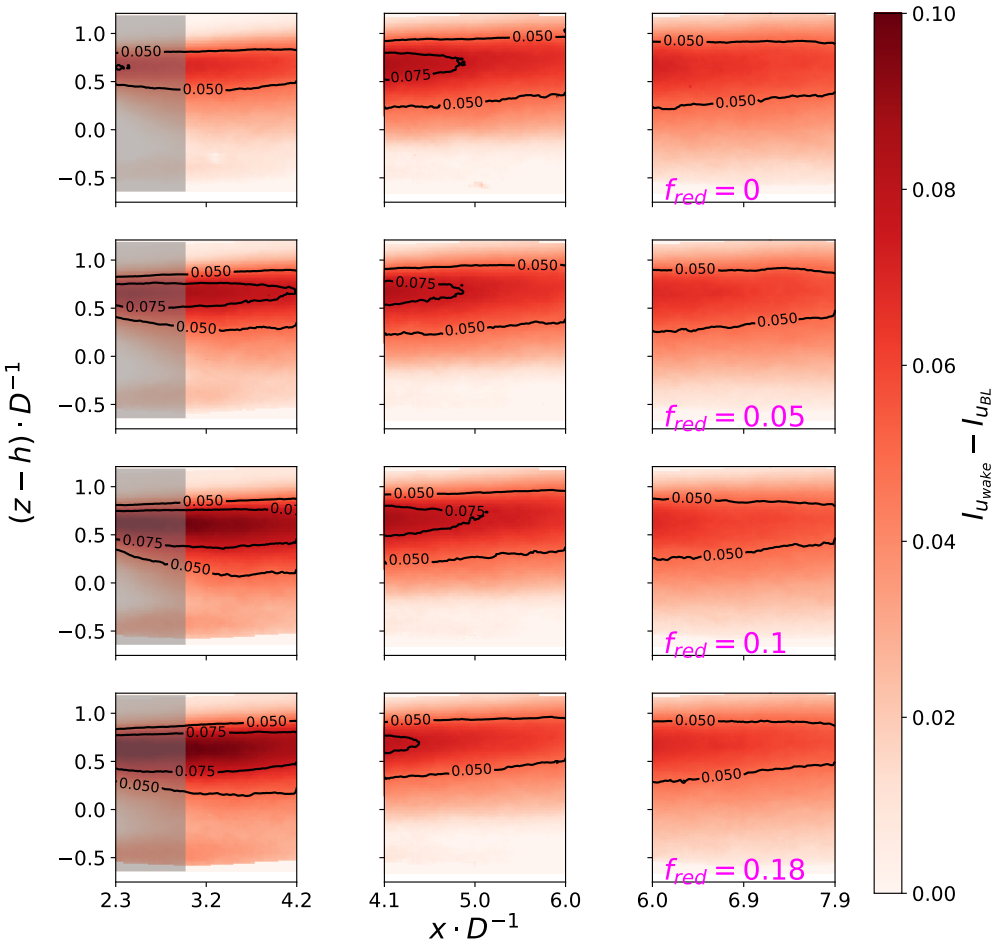

Figure 4.9 – Wake-added turbulence of the model turbine. Each panel represents one S-PIV data-set. Rows show the longitudinal development of the wake for $2.3 < x \cdot D^{-1} < 7.9$, with different motion regimes imposed ($f_{red} = 0$, $f_{red} = 0.05$, $f_{red} = 0.1$, $f_{red} = 0.18$). The distance from the model is normalised by D (x-axis). The height coordinates on the y-axis are normalised around hub height relative to the disc diameter (D). Shaded area: $x \cdot D^{-1} \leq 3$.

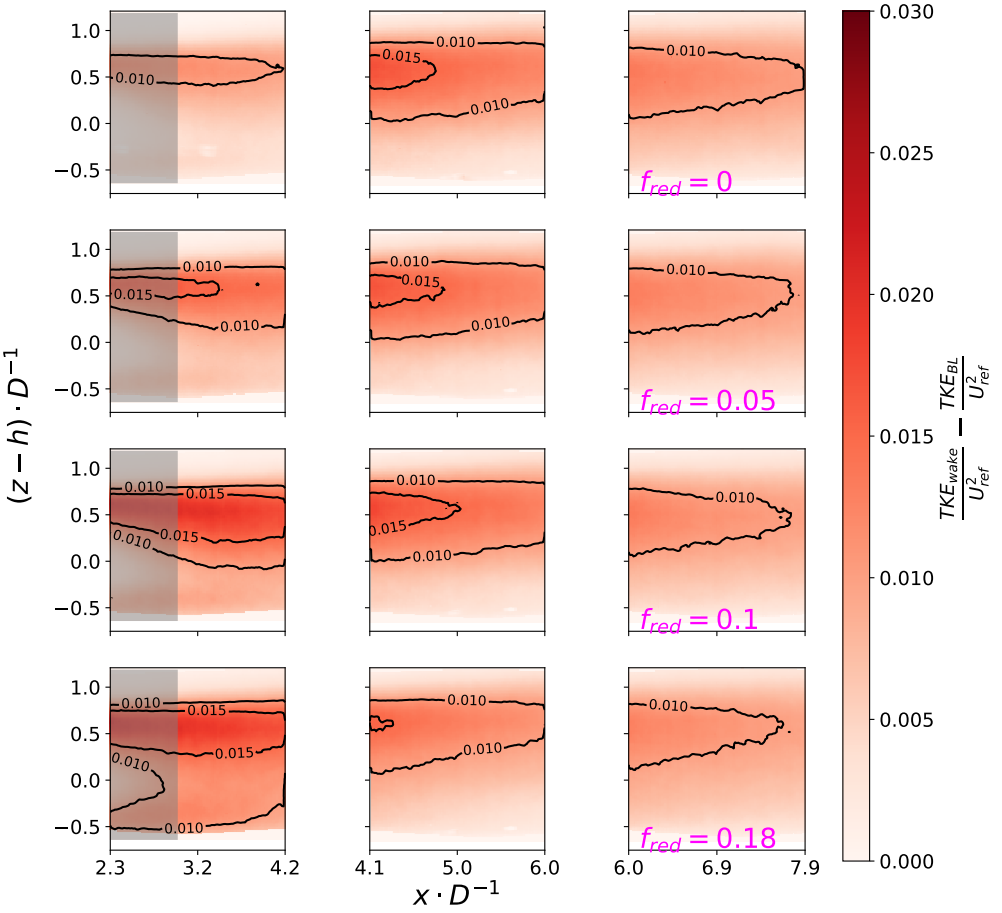

Figure 4.10 – Wake-added TKE of the model turbine. Each panel represents one S-PIV data-set. Rows show the longitudinal development of the wake for $2.3 < x \cdot D^{-1} < 7.9$, with different motion regimes imposed ($f_{red} = 0$, $f_{red} = 0.05$, $f_{red} = 0.1$, $f_{red} = 0.18$). The distance from the model is normalised by D (x-axis). The height coordinates on the y-axis are normalised around hub height relative to the disc diameter (D). Shaded area: $x \cdot D^{-1} \leq 3$.

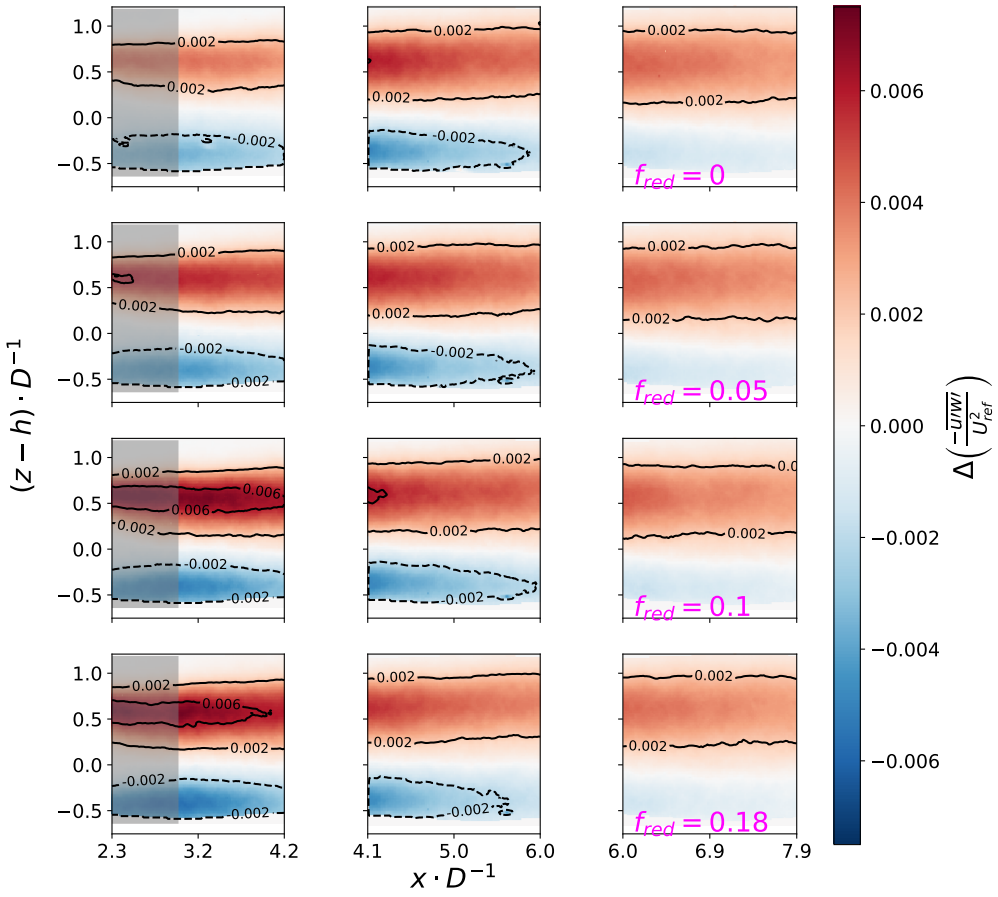

Figure 4.11 – *Re* stress changes in the wake of the model turbine compared to the BL. Each panel represents one S-PIV data-set. Rows show the longitudinal development of the wake for $2.3 < x \cdot D^{-1} < 7.9$, with different motion regimes imposed ($f_{red} = 0$, $f_{red} = 0.05$, $f_{red} = 0.1$, $f_{red} = 0.18$). The distance from the model is normalised by D (x-axis). The height coordinates on the y-axis are normalised around hub height relative to the disc diameter (D). Shaded area: $x \cdot D^{-1} \leq 3$.

dimensionless units just above top tip for $x \cdot D^{-1} < 4.2$. The maximum longitudinal expansion of these zones is marginally reduced with increased motion from $4.2\,D$ to $3.96\,D$. The thickness of the increased Re stress areas is approximately $0.7\,D$ for $f_{red} = 0.05$ and 0.76 for $f_{red} = 0.1$ and $f_{red} = 0.18$ (left hand column). Below hub height the Re stresses are reduced (dark blue areas) from -8 dimensionless units to -10 dimensionless units. The maximum longitudinal expansion decreases by $0.3\,D$ between $f_{red} = 0.1$ and $f_{red} = 0.18$ (middle column). The behaviour of the Re stresses in the far wake does not display any significant differences between the fixed turbine case and the motion regimes (right hand column).

Summarising the results presented above, it can be concluded that the effects of imposed surge motion on the spatial distribution of various wake quantities can be seen for sufficiently high motion frequencies. Indications of an accelerated wake recovery can be found in the increased levels of wake-added turbulence intensity, TKE and shear stresses for $f_{red} \geq 0.1$. Further, the results presented here confirm those discussed in section 4.2, namely, that the thicker shear layer and wider areas of increased TKE indicate enhanced mixing processes in the near and medium wake regions. In order to investigate the physical processes responsible for these results the TKE budget will be analysed next.

4.2.3 The Wake's TKE Budget

In an attempt to find a physical explanation for the observed behaviour a TKE budget analysis is conducted. The goal is to identify the process or processes responsible for changes in TKE. The TKE budget is calculated according to Blackman et al. (2017). Equation 4.7 describes the balance between the terms that compose the TKE budget:

$$\begin{aligned} 0 = &\underbrace{-\overline{u_j}\frac{\partial \overline{k}}{\partial x_j}}_{A} \underbrace{-\overline{u_i' u_j'}\frac{\partial \overline{u_i}}{\partial x_j}}_{P} \underbrace{-\frac{1}{2}\frac{\partial \overline{u_i' u_i' u_j'}}{\partial x_j}}_{T} \underbrace{-\frac{1}{\rho}\frac{\partial \overline{P' u_j'}}{\partial x_j}}_{\Psi} \\ &\underbrace{+\nu\frac{\partial}{\partial x_j}\left[\overline{u_j'\left(\frac{\partial u_i}{\partial x_j} + \frac{\partial u_j}{\partial x_i}\right)}\right]}_{D_\mu} - \varepsilon \end{aligned} \tag{4.7}$$

In equation 4.7 the first term, A, represents the advection, P is the turbulent production term, with T describing the turbulent transport. Ψ is the pressure and D_μ viscous transport, respectively. ε presents the dissipation estimation. Ψ and D_μ can not be calculated from PIV data and are thus referred to as the residual from here on. Note that the residual also contains any other contributions from derivatives that can not be calculated from the given data. This comprises most lateral derivatives, as the data is only resolved in the longitudinal-height plane, the exception being $\overline{v'v'}\frac{\partial \overline{V}}{\partial y}$ in T. This term can be calculated using the divergence free

condition for incompressible fluids (for more details see Blackman et al. (2017)).

The dissipation ε is estimated using the Large Eddy-PIV or LE-PIV approach (Sheng et al., 2000). Here the data is seen as a field with a given resolution, similar to an LES simulation. As dissipation is associated with very small scales it can not be completely resolved by PIV measurements because the resolution of the images is limited by the characteristics of the cameras used, the test set-up in general, and the post-processing of the data. In order to estimate the dissipation a sub-grid scale stress tensor is defined and calculated as an approximation of the energy being dissipated at small scales (for more details see Sheng et al. (2000)).

In the following the separate term of the TKE budget will be presented, starting with an overview of the longitudinal development of the budget in the wake of a fixed turbine. Here, the α on the x axis represents any of the quantities shown in a given figure. After that the effect of motion on the TKE budget at $x \cdot D^{-1} = 3.5$ is shown. The individual colours indicate the terms of the budget. The data is normalised by the disc's diameter D divided by the square of the mean magnitude in the undisturbed flow. The mean magnitude as calculated, is in the top left hand corner of each image.

Figure 4.12 depicts all TKE budget terms at $x \cdot D^{-1} = 3.5$ (left) and $x \cdot D^{-1} = 5.5$ (right). The blue profile represents the advection, orange is transport, green is production, red shows dissipation and purple depicts the residual. The profiles at $x \cdot D^{-1} = 3.5$ show the most notable behaviour, as to be expected. The advection has a positive contribution to the budget between hub height ($0\,D$) and $0.75\,D$ and acts as a sink above this height. Turbulent transport behaves inversely to the advection, being a sink below $0.75\,D$ and a gain above. The production term is the largest contributor to the budget across the entire profile, reaching its maximum between $0.5\,D$ and $0.75\,D$. Dissipation plays a minor role in the TKE budget in the wake of a fixed porous disc model. The budget equation has a significant residual close to the model. This can be attributed largely to pressure transport but also to other terms of the equation that can not be calculated with the data at hand. Downstream the different terms of the budget decrease in magnitude but maintain their behaviour, as the flow returns to a more undisturbed regime. The downstream behaviour of the TKE budget's terms is very similar for all motion regimes and will thus not be discussed further. The focus will be on differences at $x \cdot D^{-1} = 3.5$.

The left hand panel in figure 4.13 depicts the advection terms of all motion regimes at $x \cdot D^{-1} = 3.5$. The blue profile represents $f_{red} = 0$, orange is $f_{red} = 0.05$, green is $f_{red} = 0.1$, red shows $f_{red} = 0.18$. This colour code will be maintained for the remainder of the section on the TKE budget. The amplitude of variations of TKE advection in the profiles is slightly reduced with the introduction of motion. Overall, advection of TKE has a positive contribution to the budget between hub height and a height of $0.75\,D$. Above a height of $0.75\,D$ the advection functions as a sink in TKE at $x \cdot D^{-1} = 3.5$.

Regarding the turbulent transport term of the TKE budget (figure 4.13, right

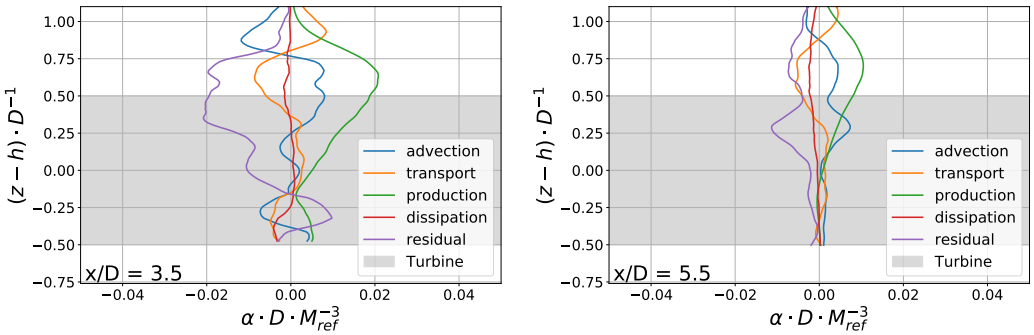

Figure 4.12 – Normalised TKE budget terms in the wake of a porous disc. Each panel represents one measurement. The images depict mean profiles (average over ± 5 rows left and right of indicated location) of each term of fixed turbine model at varying distances downstream ($x \cdot D^{-1} = 3.5$ (left), $x \cdot D^{-1} = 5.5$ (right)). The distance from the model is normalised by D. The height coordinates on the y-axis are normalised around hub height relative to the disc diameter (D). Each term of the budget is shown as one colour (blue: advection, orange: transport, green: production, red: dissipation, purple: residual).

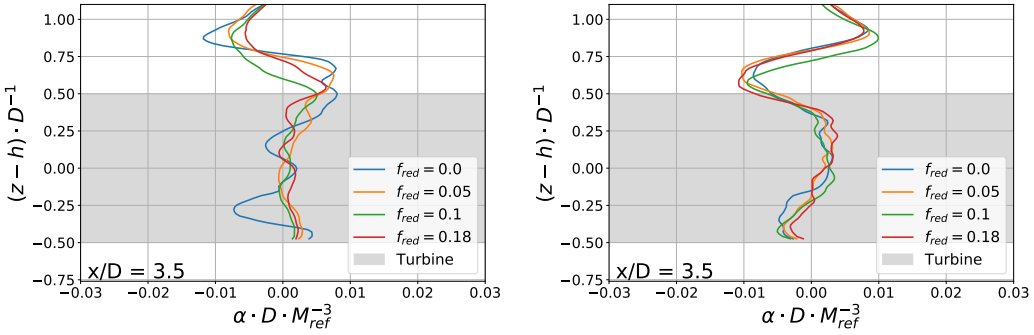

Figure 4.13 – Normalised TKE advection term (left hand panel) and normalised turbulent transport term (right hand panel) in the wake of a porous disc. The images depict mean profiles (average over a total of $0.18\,D$ around the indicated location) at $x \cdot D^{-1} = 3.5$ with different motion regimes imposed. Each motion regime has one colour (blue: $f_{red} = 0$, orange: $f_{red} = 0.05$, green: $f_{red} = 0.1$, red: $f_{red} = 0.18$).

hand panel), the shape of each profile is similar independently of the imposed motion regime. Turbulent transport acts as a sink in the TKE budget between a height of $0.25\,D$ and $0.8\,D$, where TKE is removed from the flow by means of turbulent transport.

The turbulent production at $x \cdot D^{-1} = 3.5$ downstream from the turbine is increased by the introduction of motion (cf. figure 4.14, left hand panel). It can be observed that the maxima of all production profiles with imposed motion are higher than the maximum of the fixed model's profile. The maxima are increased by 16% and 11% for $f_{red} = 0.1$ and $f_{red} = 0.18$, respectively, compared to a fixed turbine case. The turbulent production profile is weaker and wider for the fixed model case than the others at $x \cdot D^{-1} = 3.5$.

Introducing motion appears to lead to systematically increased dissipation, as can be observed in the right hand panel of figure 4.14. The profiles for $f_{red} = 0.05$, $f_{red} = 0.1$ and $f_{red} = 0.18$ have minima decreased between 148% and 324% compared to a fixed turbine case. It must be said that due to the small scales of dissipation processes and the comparatively coarse resolution of the PIV images, the associated error in the estimation of the dissipation has to be assumed to be significant. High frequency hot-wire measurements would deliver a verification of this observation.

The residual, shown in figure 4.15, or pressure transport, decreases with increasing motion. In the case of a fixed turbine (blue) the minimum of the residual is around -0.02 dimensionless units, about -0.15 dimensionless units for $f_{red} = 0.05$ and $f_{red} = 0.1$ and is roughly halved to ≈ -0.01 dimensionless units for $f_{red} = 0.18$.

As the residual captures all the processes not described above, a decreased residual term of the budget indicates that the flow is nearer to its unperturbed state, where the residual is minimal. This would imply that the wake recovers faster with imposed motion. The increased dissipation in figure 4.14 would also indicate an expedited wake recovery. In general the observed behaviour above the top tip is in line with literature regarding shear layers and introduced periodic perturbations. Tian and Xiao (2020) state find that the shear layer behind a step increases in strength when a periodic perturbation is introduced to the shear layer. To gain further understanding which processes are modified by the introduction of motion, the advection and production terms are decomposed into their respective components. The turbulent transport term can also be decomposed, but since it is not significantly affected by the introduction of motion it will not be presented here. All non-zero components, that can be calculated with the present data are discussed in the following section (section 4.2.4).

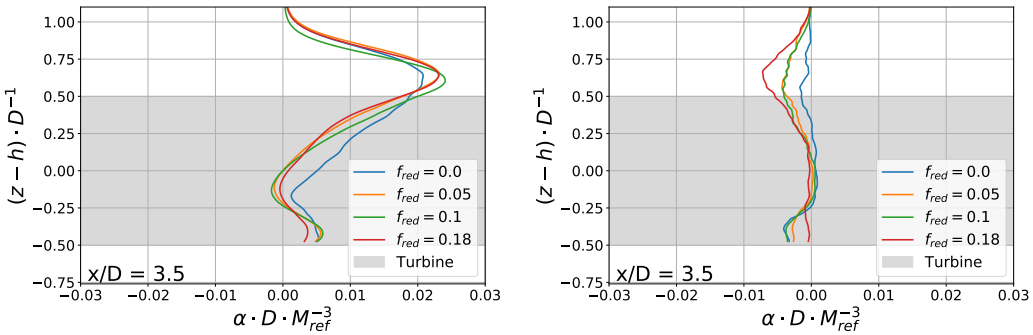

Figure 4.14 – Normalised TKE production term (left hand panel) and normalised turbulent dissipation term (right hand panel) in the wake of a porous disc. The images depict mean profiles (average over a total of $0.18\,D$ around the indicated location) at $x \cdot D^{-1} = 3.5$ with different motion regimes imposed. Each motion regime has one colour (blue: $f_{red} = 0$, orange: $f_{red} = 0.05$, green: $f_{red} = 0.1$, red: $f_{red} = 0.18$).

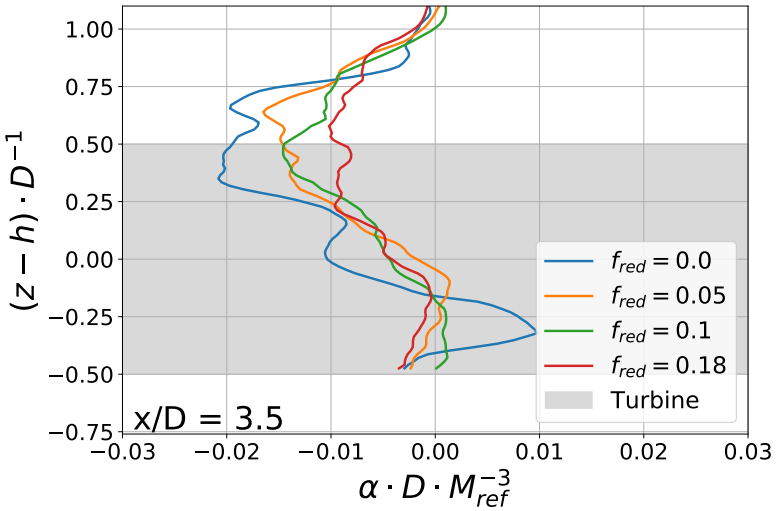

Figure 4.15 – Residual term in the wake of a porous disc. The images depict mean profiles (average over a total of $0.18\,D$ around the indicated location) at $x \cdot D^{-1} = 3.5$ with different motion regimes imposed. Each motion regime has one colour (blue: $f_{red} = 0$, orange: $f_{red} = 0.05$, green: $f_{red} = 0.1$, red: $f_{red} = 0.18$).

4.2.4 Decomposition of TKE Budget Terms

This section will focus on the effects that imposed motion has on a porous disc wind turbine model, when investigating the various components of the advection and production terms of the TKE budget. Components of the equations not shown in the following are either negligible or can not be calculated with the data at hand. Since the measurements are taken in the $x-z$ plane, this concerns most lateral gradients. For $\overline{v'v'}\partial v/\partial y$ in the production term of the budget the divergence-free condition for non-compressible fluids is invoked. This component can thus be calculated.

Figure 4.16 depicts the longitudinal (blue) and vertical (orange) advection of TKE at $x \cdot D^{-1} = 3.5$. Each column shows the evolution of the components for a given motion regime (from left to right: $f_{red} = 0$, $f_{red} = 0.1$, $f_{red} = 0.18$). The strongest component in TKE advection is longitudinal advection. In all cases, the maxima and minima of each profile can be found just below (maxima) or just above (minima) a height of $0.75\,D$. The introduction of motion does not change the general shape of the profile, but leads to a systematic weakening of the longitudinal advection (blue) at $x \cdot D^{-1} = 3.5$. The introduction of motion has minor, if any, effects on the vertical advection (orange).

In figure 4.17 the terms of the turbulent production term of the TKE budget are presented. Each column shows the evolution of the components for a given motion regime (from left to right: $f_{red} = 0$, $f_{red} = 0.1$, $f_{red} = 0.18$) at $x \cdot D^{-1} = 3.5$. An interesting observation is the negative contribution from $\overline{u'u'}\partial U/\partial x$, as negative production indicates that energy is transferred from turbulence to the mean flow (Pope, 2000). It is balanced by $\overline{v'v'}\partial V/\partial y$ for all motion regimes and distances. The driving component for changes in overall turbulent production is $\overline{u'w'}\partial U/\partial z$. Its maximum increases from 0.018 dimensionless units for $f_{red} = 0$ to 0.025 dimensionless units for $f_{red} = 0.18$. This is indicative of a stronger shear layer, when motion is introduced to the model wind turbine. The Reynolds stresses at the same location increase with increasing motion by 33% between $f_{red} = 0$ and $f_{red} = 0.18$ (see figure 4.18), while $U/\partial z$ remains constant. The reduced levels of TKE measured at $4.6\,D$, as described in section 4.2, could thus be explained by increased wake recovery upstream from that location. The enhanced momentum transport replenishes the energy of the wake faster upstream from $x \cdot D^{-1} = 4.6$, similar to observations in Yoshioka et al. (2001).

The results presented in this section indicate a slightly enhanced wake recovery, when introducing surge motion to a porous disc wind turbine model, in the range of frequency and amplitude ranges as considered in the scope of this thesis. The area of the highest wake deficit retreats from $3.29\,D$ to $2.84\,D$, while the wake deficit in the far wake remains largely unchanged, if not slightly extended. Thickened shear layers and larger areas affected by wake-added TKE point towards enhanced wake recovery processes. The TKE budget analysis shows that increased momentum transport, through increased Reynolds stresses, and increased dissipation are the

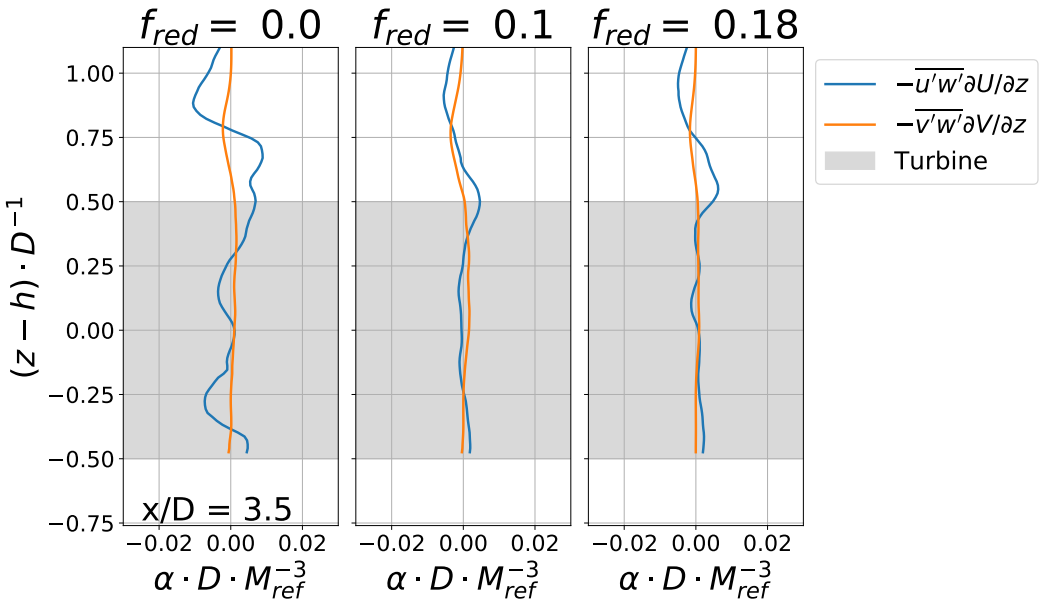

Figure 4.16 – Normalised TKE advection term components. The images depict mean profiles (average over $0.18\,D$ around indicated location) of the two advection terms that can be calculated.

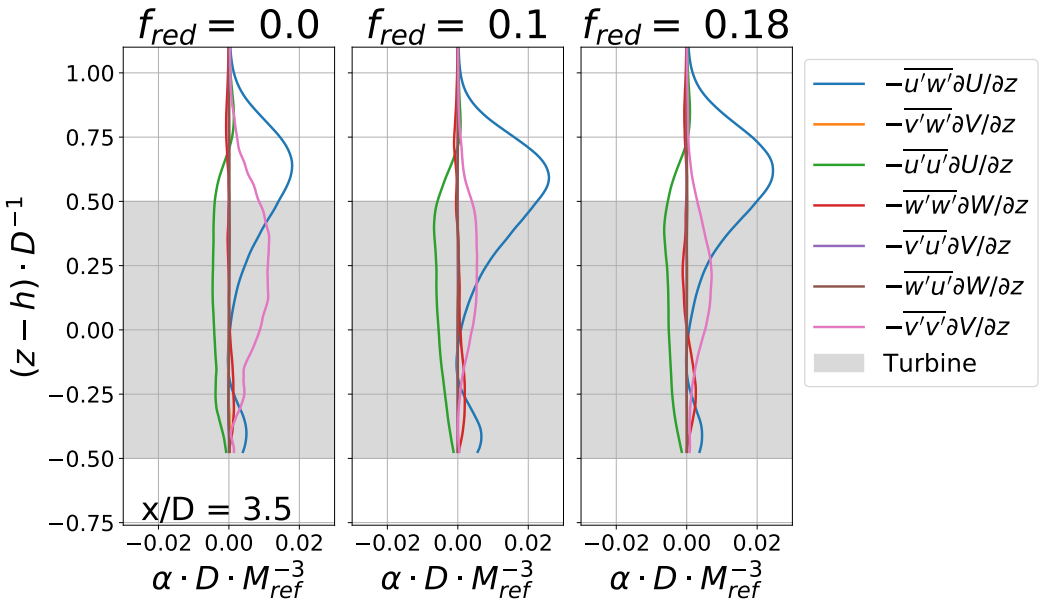

Figure 4.17 – Normalised TKE production term components. The images depict mean profiles (average over $0.18\,D$ around indicated location) of each component of the production term that can be calculated.

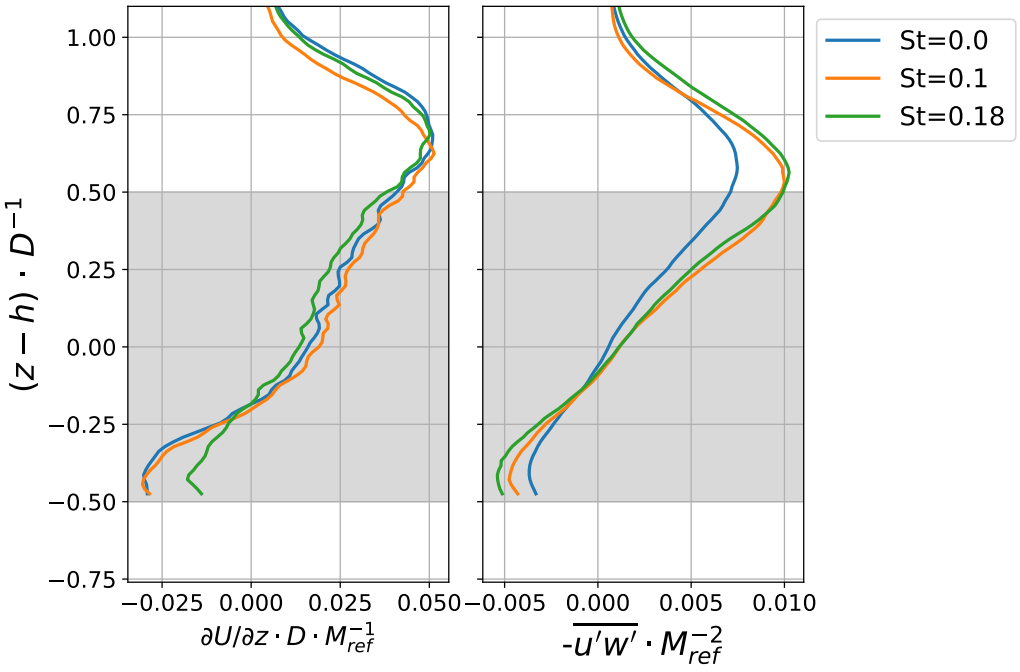

Figure 4.18 – Normalised $\partial U/\partial z$ (left) and Reynolds stresses (right). The images depict mean profiles (average over $0.18\,D$ around indicated location) of each quantity.

physical processes responsible for the faster wake recovery. It is possible that the values for the momentum transport are underestimated compared to a rotating model. In their comparative study between a porous disc and a rotating model Camp and Cal (2016) find that the wake of a porous disc has a less pronounced foot print in the TKE budget in the near wake of the model. They investigate the TKE budget up to $6\,D$ downstream using a similar experimental set-up to the one employed here. It is thus necessary to verify these results with a rotating model. Overall, the results discussed here appear to confirm those presented in Schliffke et al. (2020).

4.2.5 Effects of Sway Motion on the Wake

In this section the same analysis as above is applied to data gained when the model is subjected to sway (lateral) motion. Due to technical limitations it was not possible to reproduce the same f_{red} as in section 4.2. When investigating the effect of varying amplitudes, the travel velocity of the model is kept constant in order to avoid seeing potential effects of varying velocities on top of varying amplitudes. This leads to decreasing f_{red} for increasing amplitudes.

Idealised sinusoidal sway motion leads to a modified vertical normalised longitudinal velocity profile. The introduction of motion at varying frequencies leads to gains in the average velocity profile in the disc area. The largest deviations can be observed for the highest prescribed f_{red} (figure 4.19, left hand panel). The increased gains do not appear to be systematic as $f_{red} = 0.05$ (red) and $f_{red} = 0.2$ (orange)

deliver roughly the same gains, while $f_{red} = 0.1$ (green) shows an increased gain of the mean flow velocity. Similarly, $f_{red} = 0.24$ (purple) also produces the largest deviations in the TKE profile (right hand panel). Motion frequencies of $f_{red} = 0.05$ and $f_{red} = 0.2$ show little changes, or marginal losses, in TKE. The TKE profile for $f_{red} = 0.24$ shows slightly erratic gains in TKE below hub height, while the profile follows that of $f_{red} = 0.1$ otherwise (4.19, right hand panel).

Figure 4.20 shows vertical profiles of I_u, I_v and I_w for the different motion regimes tested. I_u is not significantly modified by sway motion compared to a fixed turbine (blue data). I_v is increased beneath hub height for $f_{red} = 0.18$. I_w is reduced for all motion regimes.

Considering the $\overline{u'v'}$ and $\overline{u'w'}$ stresses depicted in figure 4.21, $\overline{u'v'}$ is decreased for all motion frequencies (left hand panel). Regarding $\overline{u'w'}$, in the right hand panel, the profile is flattened compared to the fixed turbine case when introducing sway motion. This means the Reynolds stresses present gains around $h = -0.5\,D$ and losses around $h = 0.5\,D$ compared to the fixed turbine case.

When varying the amplitude of sway motion the effects on the wake are less clear than when varying the motion frequency. Uniform gains in the mean velocity can be observed in the disc area. These gains are independent of the applied amplitude (figure 4.23 left hand panel). The TKE is not affected by varying the motion's amplitude (right hand panel). Regarding the turbulence intensity, I_u is not affected, while I_v and I_w show mild losses compared to the fixed turbine's wake. This behaviour can be expected along the wake's centre line as varying the motion amplitude in the case of sway. It would be expected that the increased amplitude would lead to modified amplitudes of wake meandering, which can be distinctly observed at the wake's edges.

The Reynolds stresses show the same behaviour when the amplitude is varied as in the case of varying reduced frequencies. $\overline{u'v'}$ is decreased for all amplitudes investigated (figure 4.24, left hand panel). Similarly to the case of varying f_{red}, $\overline{u'w'}$, in the right hand panel, the profile is flattened relative to the fixed turbine case, with similar gains around $h = -0.5\,D$ and losses around $h = 0.5\,D$.

Regarding imposed idealised sway motion it may be concluded that the motion has some visible effects on the mean and turbulent quantities in the wake at $4.6\,D$. Generally, all the quantities indicate an accelerated wake recovery. As with surge motion, the reduced turbulence intensity and TKE support the hypothesis of enhanced wake recovery. The lower levels of turbulent shear stresses investigated above also indicate a faster recovery process. Fu et al. (2019) explain the enhanced wake recovery with the injections of undisturbed flow when the turbine model is at or near the extremes of its motion regime.

To conclude this section on mean and turbulent values as well as the TKE budget it can be stated that the overall effect of idealised surge or sway motion has limited effect on the mean and turbulent values. The general tendency of the mean and turbulent values points towards slightly accelerated wake recovery processes. This

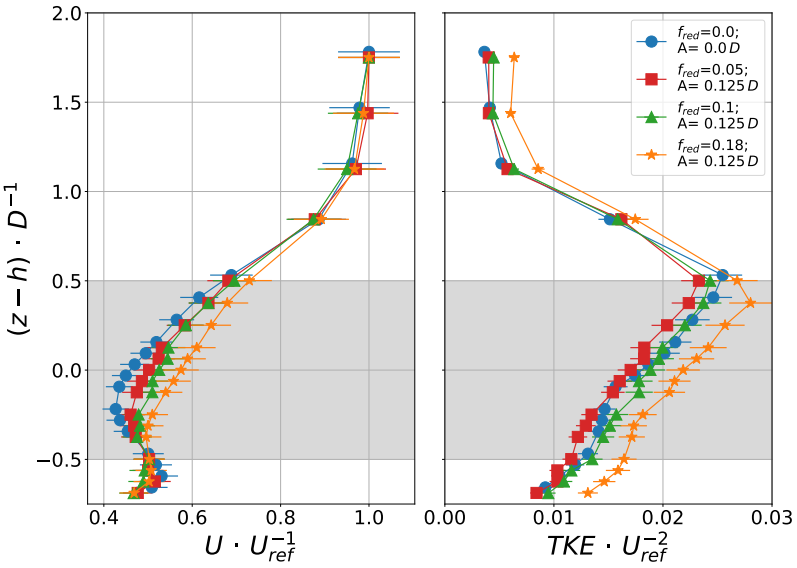

Figure 4.19 – Vertical profiles of the mean normalised velocity (U) and normalised turbulent kinetic energy (TKE). Case: Constant amplitude, varying reduced frequency ($f_{red} = 0.1$). Measured 4.6 D downstream of the actuator disc when subjected to sway motion.

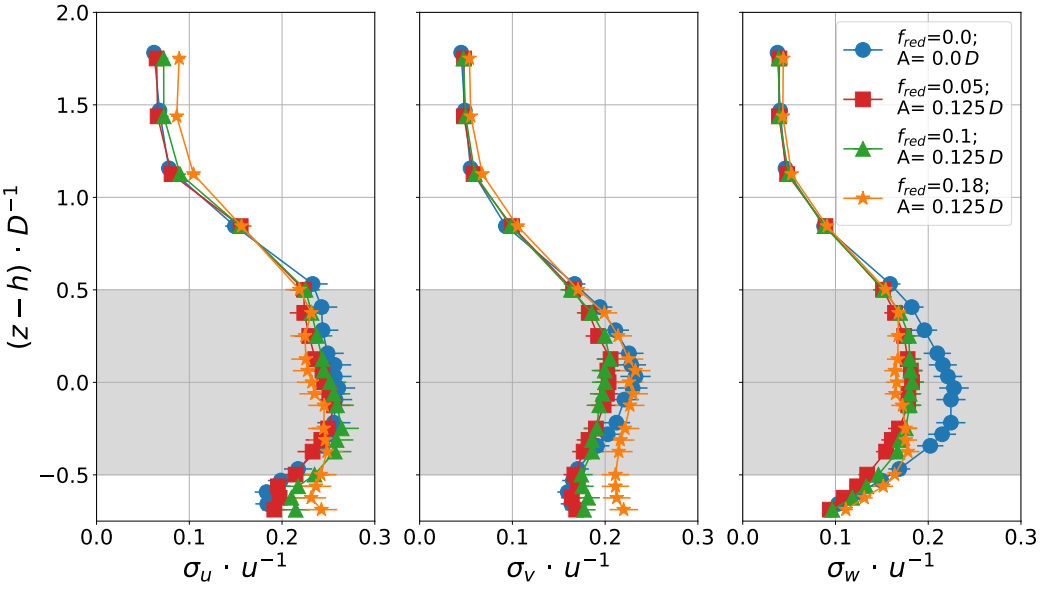

Figure 4.20 – Vertical profiles of the turbulence intensity of each velocity component. Constant amplitude, varying f_{red}. Measured 4.6 D downstream of the actuator disc when subjected to sway motion.

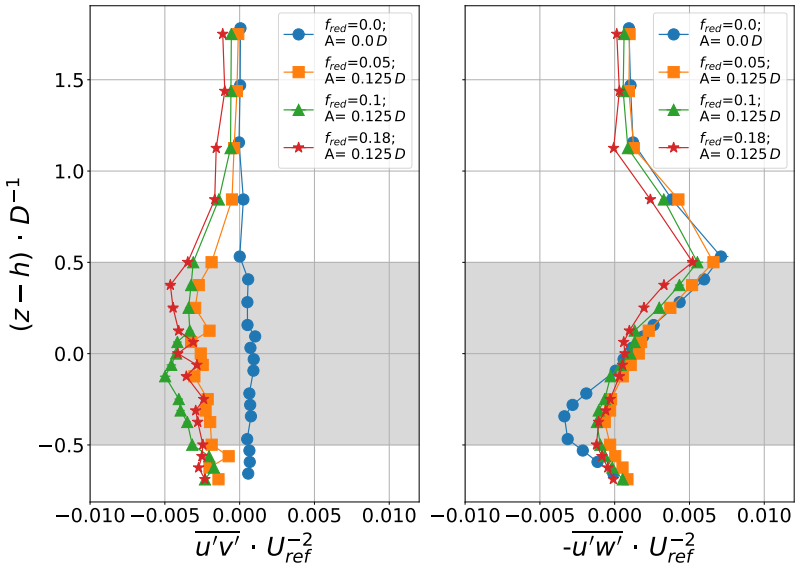

Figure 4.21 – Vertical profiles of the $\overline{u'v'}$ and $\overline{u'w'}$ stresses. Case: Constant amplitude ($A = 0.125\,D$), varying reduced frequency. Measured $4.6\,D$ downstream of the actuator disc when subjected to sway motion.

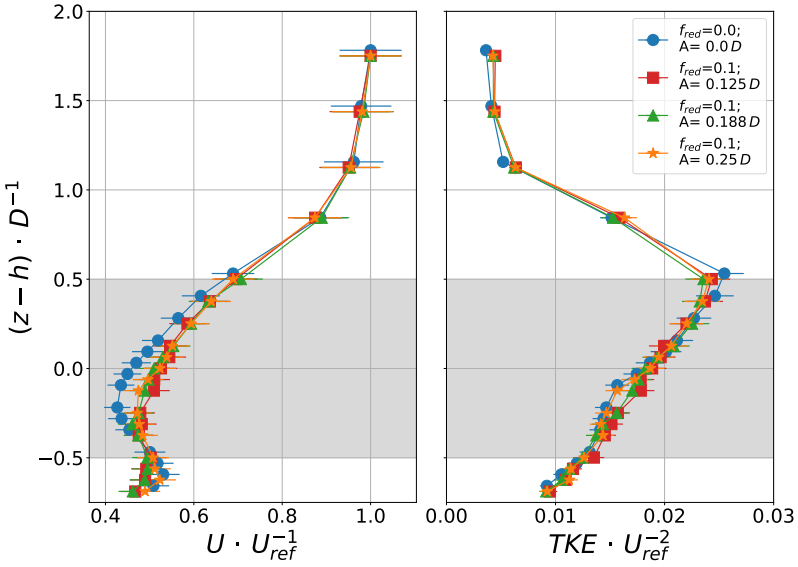

Figure 4.22 – Vertical profiles of the mean normalised velocity (U) and normalised turbulent kinetic energy (TKE). Case: Constant travel velocity, varying amplitudes. Measured $4.6\,D$ downstream of the actuator disc when subjected to sway motion.

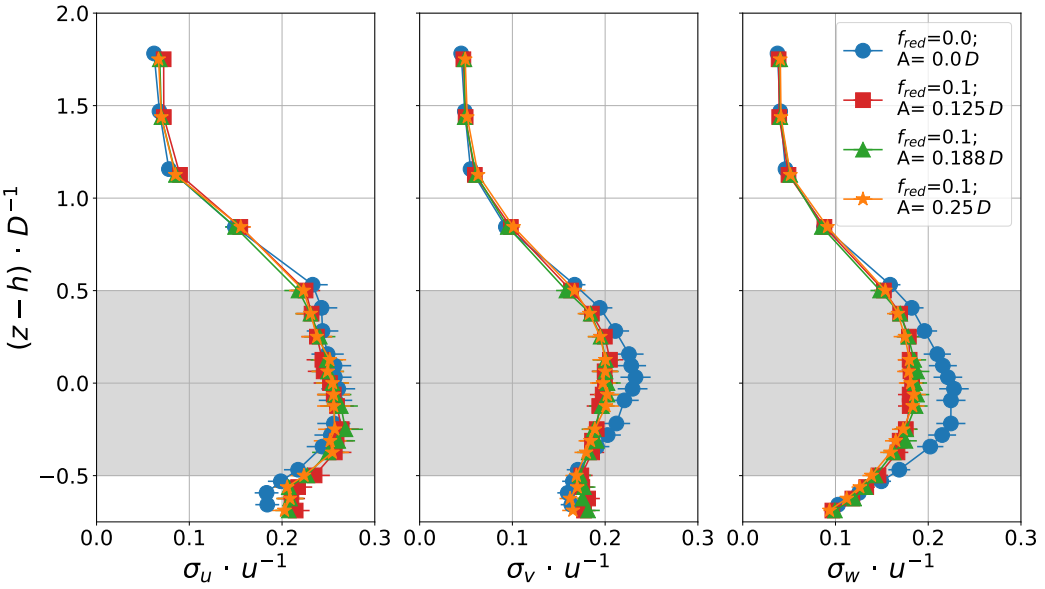

Figure 4.23 – Vertical profiles of the turbulence intensity of each velocity component. Constant travel velocity, varying amplitudes. Measured 4.6 D downstream of the actuator disc when subjected to sway motion.

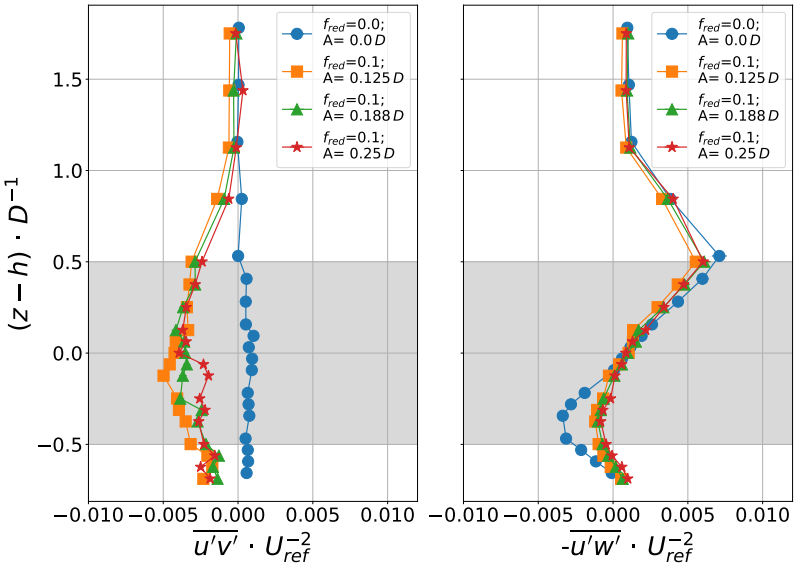

Figure 4.24 – Vertical profiles of the $\overline{u'v'}$ and $\overline{u'w'}$ stresses. Case: Constant travel velocity, varying amplitudes. Measured 4.6 D downstream of the actuator disc when subjected to sway motion.

has since been confirmed by Fontanella et al. (2021). Idealised surge motion leads to stronger shear layers and consequently increased momentum transport in the wake. This confirms the tendency towards an enhanced wake recovery displayed by the mean and turbulent values. Overall the mean quantities are only mildly affected by the introduction of motion, thus the following section will focus on the wake's unsteady behaviour.

4.3 Unsteady Wake Behaviour

In this section the unsteady behaviour of the wake is discussed. It is based on an analysis of spectra measured in the wake at $4.6\,D$ downstream from the turbine. The data is gathered with either a rake of hot-wire anemometers or the Cobra probe. The technology used is mentioned in the respective sections. The measurement height is at hub height unless noted otherwise. The aim is to identify motion regimes that leave a clear signature in the wake, while maintaining motion regimes as close to reality as possible. The spectra presented in the remainder of this section are compared to the spectrum of the fixed turbine. The comparison of the hot-wire data is quantified by calculating the difference between the respective normalised energy spectra:

$$\varphi = \frac{f \cdot E_{motion}}{U_{ref}^2} - \frac{f \cdot E_{fixed}}{U_{ref}^2} \tag{4.8}$$

where f is the frequency, E is the power spectral energy density of the velocity fluctuations and U_{ref} is the mean free stream velocity. As this method enables the detection of small differences between the spectra, φ_{max} is introduced to compare the effects of motion. φ_{max} is the maximum of φ in the frequency range investigated here ($f_{red} \leq 0.5$). In order for φ_{max} to be considered as a peak, it must be greater than 0.01. The value of 0.01 is determined empirically as it captures all clear and few spurious peaks. This method is applied to all data-sets measured using the rake of hot-wires to maintain a high degree of comparability. The peaks and the corresponding frequencies are found using scipy's $find\_peaks$ function.

As an introduction, the normalised pre-multiplied energy spectra of the velocity fluctuations in the undisturbed boundary layer (without the model) and in the wake of the fixed turbine model will be presented and compared. Figure 4.25 shows the energy spectra in the undisturbed boundary layer on the left and that of the fixed turbine's wake on the right. The data is gathered using the hot-wire rake mounted $4.6\,D$ downstream of the model. The probe positions on the rake are named from left to right facing downstream starting at $y \cdot D^{-1} = -0.94$ at the outer left position and finishing at $y \cdot D^{-1} = 0.94$ at the outer right position. Each lateral position is colour coded as follows: $y \cdot D^{-1} = -0.94$ is purple, $y \cdot D^{-1} = -0.625$ is dark blue, $y \cdot D^{-1} = -0.3125$ is blue, $y \cdot D^{-1} = 0$ is dark green, $y \cdot D^{-1} = 0.3215$ is green,

$y \cdot D^{-1} = 0.625$ is light green and $y \cdot D^{-1} = 0.94$ is yellow. The normalised energy is plotted against the corresponding reduced frequency to maintain comparability with the other results discussed in this thesis. Only the frequency range from $f_{red} = 0.001$ to $f_{red} = 2$ is shown, as this encompasses all of the imposed motion frequencies studied in this thesis. The same presentation is maintained for all spectra presented in this section unless mentioned otherwise. The colour codes vary depending on the measurement instrument, as mentioned at the beginning of this chapter.

The energy spectra in the boundary layer at each probe position are superimposed, as can be expected in a laterally homogeneous turbulent flow (fig. 4.25, left hand panel). Introducing the porous disc removes energy from the flow, reducing the maximal normalised energy levels from 0.3 to between 0.1 and 0.01, depending on the lateral measurement position (fig. 4.25, right hand panel). In general, the outer positions at $y \cdot D^{-1} = -0.94$ and $y \cdot D^{-1} = 0.94$ display the lowest energy levels. Compared to the energy spectrum of the boundary layer, the model's wake spectrum is characterised by an extended crest between $f_{red} = 0.2$ to $f_{red} = 0.6$ between the positions at $y \cdot D^{-1} = -0.625$ and $y \cdot D^{-1} = 0.625$. This crest can be related to the presence of the porous disc and can be considered characteristic of said disc. The crest is not present in the outer positions. The motion frequencies chosen to be representative of realistic motions, are in the same frequency band. First, surge motion is presented in section 4.3.1, followed by sway (section 4.3.1), heave (section 4.3.1) and pitch (section 4.3.1).

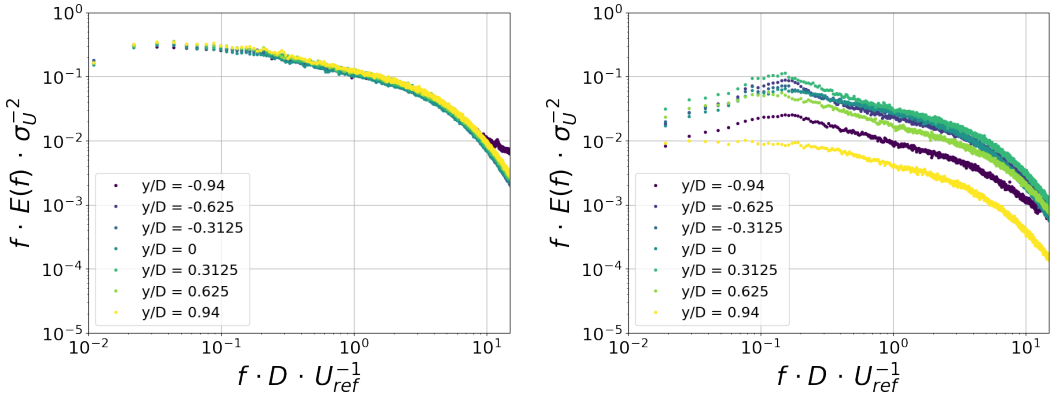

Figure 4.25 – Normalised pre-multiplied energy spectra of the flow magnitude U at hub height measured 4.6 D downstream using hot-wire anemometers. Left hand panel: boundary layer (without model), right hand panel: with a fixed turbine model.

4.3.1 Idealised 1 Dof Motion

Idealised Surge Motion

In the following, the spectral content of all velocity components at hub height is analysed. Then the lateral and vertical distributions and energy magnitudes of the peaks are discussed. A brief summary of the observations made in this section is given at the end.

The data presented here is measured using the Cobra probe. It can be seen in figure 4.26 that the prescribed motion frequency delivers a clear peak at the equivalent frequency in the energy spectrum of the longitudinal flow component u (left hand panel). The spectrum for $f_{red} = 0.05$ does not have an identifiable peak. In all other cases the peaks become more prominent with increasing f_{red}. With $f_{red} \leq 0.18$ the spectra correspond to the reference case. In the case of $f_{red} = 0.27$ a slight decrease in large scale turbulence and gain in small scale turbulence can be observed, when compared to the fixed case. As the crests of each spectrum are located near the crest of the atmospheric boundary layer spectrum at $f_{red} \approx 0.2$, enhanced interaction between the wake and the surrounding flow can be expected.

Similar behaviour can be seen in the w component (right hand panel). $f_{red} = 0.18$ and $f_{red} = 0.27$ show clear peaks at the prescribed motion frequencies. There is no overall shift to smaller scale turbulence, as can be observed for u. With regard to the lateral component v, there appears to be no impact of surge motion on its energy spectrum (central panel).

When maintaining $f_{red} = 0.1$ and varying the amplitude, all peaks in the spectrum of the u component are associated to the prescribed f_{red} (figure 4.27, left hand panel), as is to be expected considering the observations made above. The peaks become more prominent with increasing amplitude. The motion regime using $A = 0.312\,D$ shows a first harmonic. Comparing the spectra suggests that less en-

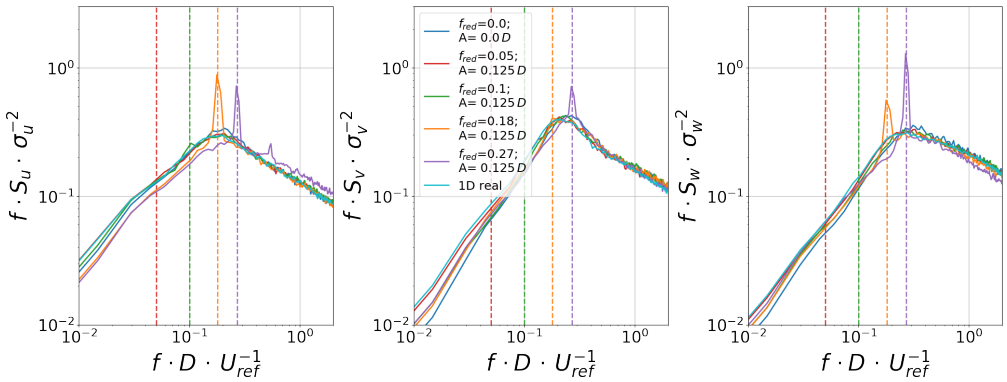

Figure 4.26 – Normalised pre-multiplied energy spectra of the u (left), v (centre) and w (right) components of the wake at hub height measured 4.6 D downstream using the Cobra probe when the model is subjected to surge motion with varying frequencies at an amplitude of 0.125 D. dark blue: fixed turbine, orange: $f_{red} = 0.05$, green: $f_{red} = 0.1$, red: $f_{red} = 0.18$, purple: $f_{red} = 0.27$, light blue: realistic motion (1 Dof).

ergy is present in the wake compared to a fixed turbine when the amplitude of the motion is increased. This is also true for the v and w components (central and right hand panels). A small peak and its first harmonic can be observed in the energy spectrum of the w component at $A = 0.312\,D$.

As shown above, the energy spectra in the wake of a model FOWT can show easily identifiable peaks when the model is subjected to sufficiently strong surge motion. In order to gain an understanding of which lateral and vertical positions of the wake are affected, the rake of hot-wires is employed. To this avail the peak height of each spectrum is determined as described at the beginning of this section. The peak height is plotted against the reduced frequency at which it was detected (figure 4.28). Each lateral position has its own marker. Each vertical position also has a unique marker. The colours of the shapes represent the different motion regimes applied. The naming of the positions follows those shown in figure 3.28 presented in section 3.4 (OL: outer left, L: left, CL: centre left, C: centre, CR: centre right, R: right, OR: outer right, UC: upper centre, T: top).

The left hand panel in figure 4.28 depicts the lateral positions of the detected peak heights with their corresponding frequencies. The amplitude is kept constant at $A = 0.125\,D$ and f_{red} is varied between 0.1 and 0.27. If a motion regime does not appear in the figure it means that there are no detectable peaks in the energy spectrum of the corresponding motion regime. All lateral measurement positions for $f_{red} = 0.19$ and $f_{red} = 0.27$ show clear peaks at their assigned frequencies. The detected peaks are similar in height varying between 0 and 0.5, with the exception of the central position at $f_{red} = 0.27$. The peak is located at $\varphi_{max} = 1$. An even clearer picture presents itself when looking at the vertical distribution of the peak heights for $f_{red} = 0.19$ and $f_{red} = 0.27$ (fig. 4.28 right hand panel). Each peak is associated to the prescribed motion frequency. The peak heights are also clearly

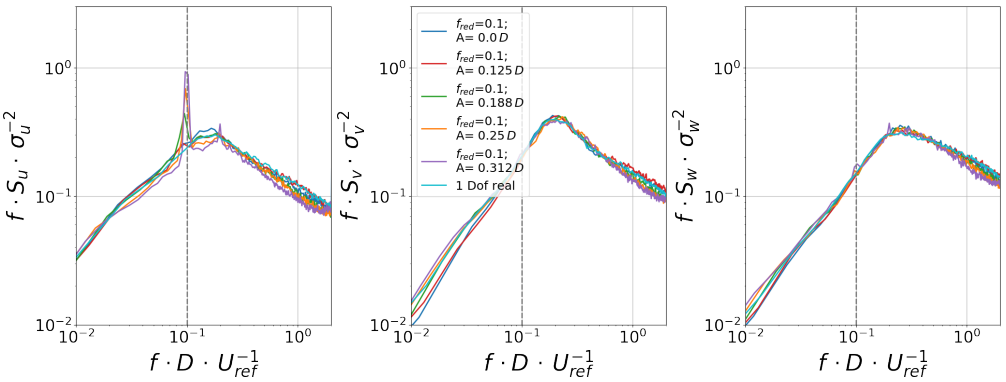

Figure 4.27 – Normalised pre-multiplied energy spectra of the u (left), v (centre) and w (right) components of the wake at hub height measured 4.6 D downstream using the Cobra probe when the model is subjected to surge motion with varying amplitudes at $f_{red} = 0.1$. Blue: fixed turbine, red: $A = 0.125\,D$, green: $A = 0.188\,D$, orange: $A = 0.25\,D$, red: $A = 0.312\,D$, light blue: realistic motion (1 Dof).

organised from hub height to top tip for $f_{red} = 0.27$. The peak heights are around 0.5 for $f_{red} = 0.19$ and reach up to 2 for $f_{red} = 0.27$.

Figure 4.29 shows the effects of varying the motion's amplitude from $A = 0.125\,D$ to $A = 0.25\,D$ at a constant reduced frequency of $f_{red} = 0.1$ on the energy spectra's peak heights. The left hand panel shows the lateral distribution of the peak heights, using the same markers and colour code as described above. The peaks for $A = 0.25\,D$ are mostly associated to $f_{red} = 0.1$. The left and right locations have peaks shifted upwards from the assigned to $f_{red} = 0.18$. The detected peaks correspond to φ_{max} values between 0.15 to 0.45. In the right hand panel the vertical distribution of the peak heights is presented. Similar behaviour can be observed regarding the increased spread of the respective peak heights with respect to the analysis of varying frequencies, though the total spread is reduced. The peaks are located between 0.12 and 0.45.

It may be concluded from the results shown above that imposed characteristic surge motion does leave a clear trace in the energy spectra of the wake of a modelled FOWT. The spectra of longitudinal u and vertical w flow components are affected by surge motion, while the lateral component v is not affected by the motion, as the Cobra data shows. The identified peaks are all found at the imposed motion frequency. A clearer response, i.e. higher peak heights, is obtained from increased amplitudes at constant f_{red} rather than increased motion frequencies at constant amplitudes. Recent results published by Ramos-García et al. (2021) confirm this. Introducing surge motion leads to peaks in the energy spectra at all lateral positions analysed. These peaks are similar in height at each location. Vertically the peak heights spread over a much larger range, especially at $h = 0.625\,D$. This can also be concluded when varying the motion's amplitude at a constant f_{red}. The measurement position at $h = 0.625\,D$ is presumed to be in the shear layer. As discussed in section 4.2.2, the shear layer is affected by the introduction of motion and appears

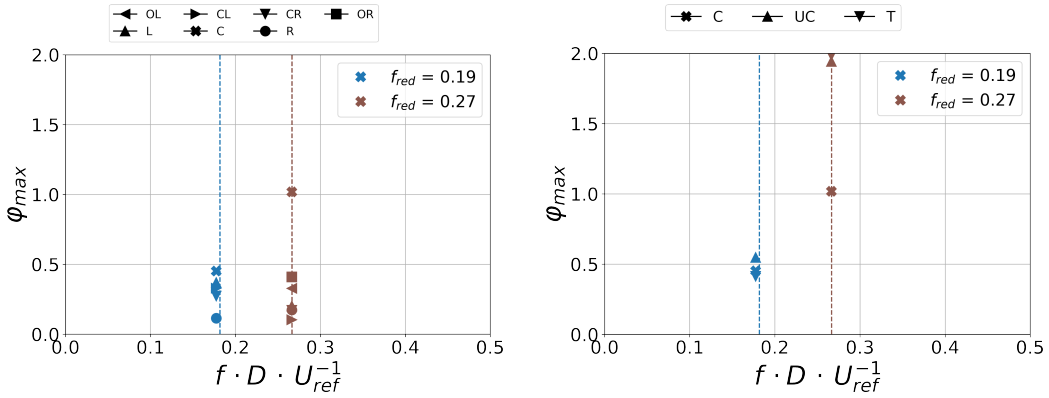

Figure 4.28 – φ_{max} for imposed surge motion with a constant amplitude of $A = 0.125\,D$ at $4.6\,D$ measured at hub height at different lateral (left hand panel), and vertical positions (right hand panel). The colours represent the different motion regimes.

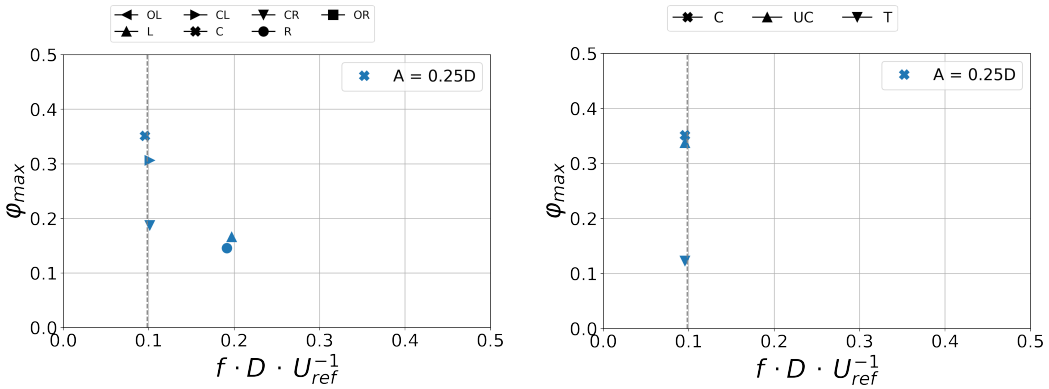

Figure 4.29 – φ_{max} for imposed surge motion with constant $f_{red} = 0.1$ at $4.6\,D$ measured at hub height at different lateral (left hand panel), and vertical positions (right hand panel). The colours represent the different motion regimes.

to be sensitive to the induced frequencies, as shown above.

Idealised Sway Motion

The spectral content of the lateral velocity component at hub height reveals peaks at the assigned frequencies of $f_{red} = 0.05$, $f_{red} = 0.1$ and $f_{red} = 0.18$ (figure 4.30). The longitudinal flow component (left hand panel) shows no clear peak in the spectra at $f_{red} = 0.05$ (red) and $f_{red} = 0.1$. At $f_{red} = 0.18$ (orange) a peak is visible, as well as its first harmonic. The peak at $f_{red} = 0.18$ in the v component's spectrum is the most prominent in all spectra investigated at $4.6\,D$ (central panel). This may indicate non-linear interactions in the wake. The entire spectrum at $f_{red} = 0.18$ is otherwise deprived of energy compared to the reference case. The crest of the spectrum for $f_{red} = 0.1$ is shifted to the right and flattened, suggesting a shift of turbulent broad-band energy to smaller scales. Again $f_{red} = 0.05$ follows the reference case with a small peak at the assigned frequency. The w component (right hand panel) is hardly affected by imposing sway on the turbine model.

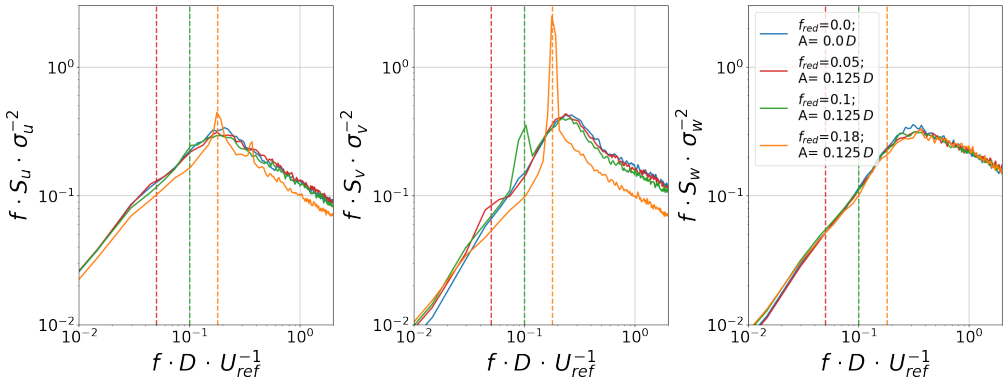

Figure 4.30 – Normalised pre-multiplied energy spectra of the u (left), v (centre) and w (right) components of the wake at hub height measured $4.6\,D$ downstream using the Cobra probe when the model is subjected to sway motion with varying f_{red}. Blue: fixed turbine, red: $f_{red} = 0.05$, green: $f_{red} = 0.1$, orange: $f_{red} = 0.18$.

Maintaining the travel velocity of the model constant, and varying the amplitude of the sway motion, delivers slightly modified spectra (figure 4.31). The peaks in the u and v energy spectra can be associated to their corresponding prescribed f_{red} (left hand and central panels, respectively). The exception is the u component at $A = 0.125\,D$, that does not have a peak at the assigned frequency. The spectra for $A = 0.188\,D$ and $A = 0.25\,D$ are marginally modified from the reference case. The crests are shifted to the left indicating the presence of larger scale turbulent energy. The spectrum at $A = 0.125\,D$ is derived from the same data as the spectrum $f_{red} = 0.1$ described above. Here, a shift of the spectrum to the right can be observed. There is no clear effect of surge motion on the energy spectrum of the w component.

Overall, introducing lateral motion modifies the turbulent spectra in the wake more clearly than introducing longitudinal motion. This indicates that the wake's characteristics are changed significantly with the introduction of sway motion. The

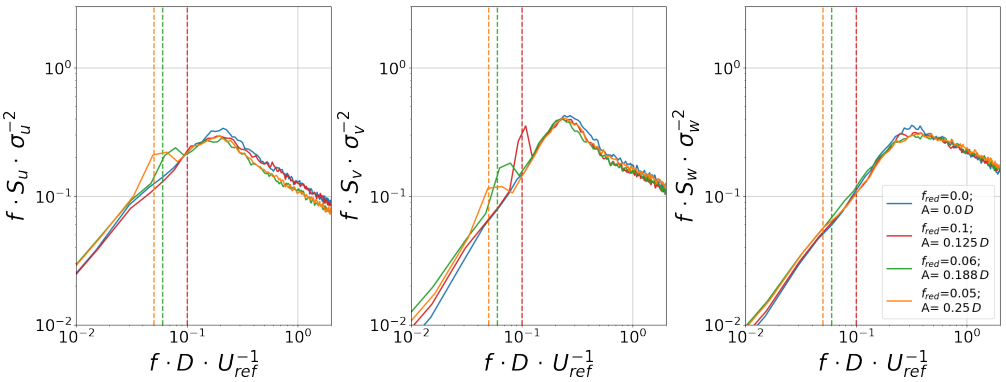

Figure 4.31 – Normalised pre-multiplied energy spectra of the u (left), v (centre) and w (right) components of the wake at hub height measured 4.6 D downstream using the Cobra probe when the model is subjected to sway motion with varying amplitudes. Blue: fixed turbine, red: $A = 0.125\,D$, green: $A = 0.188\,D$, orange: $A = 0.25\,D$.

w component at hub height (right hand panel) is hardly affected by imposing sway on the turbine model. In contrast to the surge motion studied earlier, the amplitude of the imposed sway motion has little effect on the peak height in the energy spectra of the u and v flow components. As a new motion system is used when acquiring hot-wire data, and it can not be turned easily, no lateral and vertical peak data is available for sway motion.

Idealised Heave Motion

As the data shown in figure 4.32 indicates, the amplitude of heave motion has little measurable effects on the energy content of the wake of a modelled FOWT. At hub height φ_{max} (left hand panel) two peaks are detected. The measurement position along the centre line (cross) of the wake is associated to the imposed motion frequency ($f_{red} = 0.15$) for $A = 0.062\,D$. The second peak is a spurious peak and can not be interpreted at this point. Looking at the vertical measurement positions (right hand panel), all φ_{max} can be related to the imposed motion frequency for $A = 0.031\,D$ and $A = 0.062\,D$. The larger the amplitude, the clearer the response of φ_{max} is. When varying the motion frequency and maintaining the amplitude at $0.0125\,D$, no φ_{max} can be detected at any of the imposed frequencies ($f_{red} = 0.15$, $f_{red} = 0.2$ and $f_{red} = 0.3$).

In summary, the effects of heave motion on the energy spectra in the wake of a porous disc appear to be more dependent on the motion's amplitude rather than the motion's frequency. A reduced frequency of $f_{red} = 0.3$ does not deliver detectable peaks in the spectrum at any lateral or vertical location studied here. The motion's amplitude does lead to the appearance of peaks in the energy spectra along the wake's centre line. In order to observe the peaks the heave motion's amplitude must be equal to or greater than $0.031\,D$.

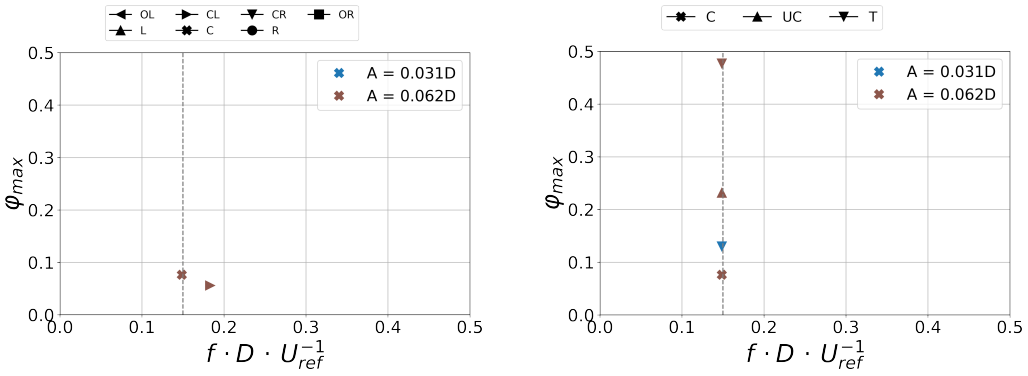

Figure 4.32 – φ_{max} for imposed heave motion with constant $f_{red} = 0.15$ at $4.6\,D$ measured at hub height at different lateral (left hand panel) and vertical positions (right hand panel). The colours represent the different motion regimes.

Idealised Pitch Motion

Considering φ for pitch motion, it can be concluded that this motion leaves no clear signature in most cases (figure 4.33). Only the highest motion frequency at $f_{red} = 0.25$ delivers a detectable peak in φ that is clearly related to the motion frequency. The two peaks detected for $f_{red} = 0.19$ are close to the motion frequency but are located on the right hand side of the wake, where no peaks have been found in any of the other cases. It is thus possible that these are spurious peaks picked up by the detection method, rather than φ_{max} related to the induced motion frequency (left hand panel). Looking at the vertical distribution of φ_{max} on the right hand panel, the peaks associated to $f_{red} = 0.25$ are at the upper centre (UC) and top (T) positions. At the characteristic pitch frequency of $f_{red} = 0.125$ no φ_{max} can be identified for any of the amplitudes tested in the scope of this thesis (2°, 5° and 8°).

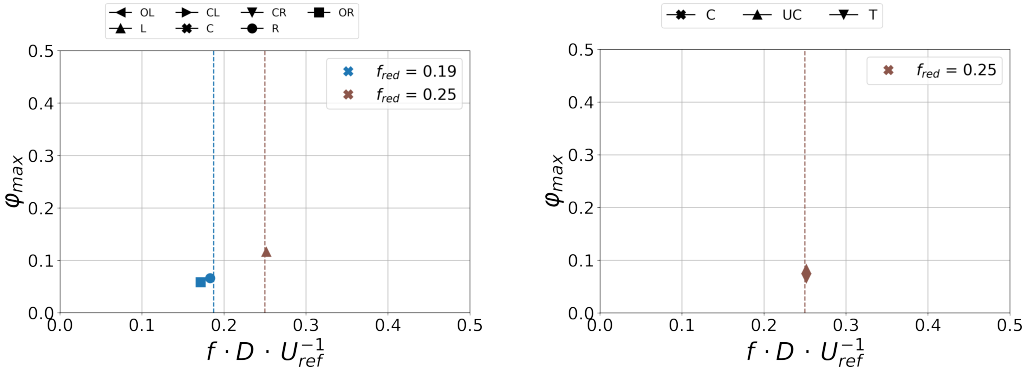

Figure 4.33 – φ_{max} for imposed pitch motion with a constant amplitude of 2° at $4.6\,D$ measured at hub height at different lateral (left hand panel) and vertical positions (right hand panel). The colours represent the different motion regimes.

Similar behaviour is observed in Ramos-García et al. (2021), who find little effect of pitch motion on the turbine's wake. The authors suggest that pitch motion is

comparable to surge motion. The chord of the rotational motion at the top tip, as the point that travels furthest in the x direction, is thus considered as equivalent to the amplitude of surge motion. The maximum amplitude of 8° thus gives an equivalent surge motion amplitude of approximately $0.062\,D$. This amplitude is about half of the minimal amplitude investigated when analysing surge motion ($0.125\,D$), which also shows no clear peaks. Thus the limited effects of pitch motion on the wake can be expected.

4.3.2 Realistic 1 Dof Motion

In the following section the impact of realistic 1 Dof motion on the energy spectra measured in the wake of the moving turbine model are presented. Realistic motion is different from idealised motion in that it contains a frequency band, rather than just one frequency. The motion spectra of each Dof (X, Z and R_y) are shown in figure 4.34. Surge motion (X) is most energetic at lower frequencies, while heave (Z) and pitch (R_y) are most energetic around $f_{red} = 1$. The surge motion also has contributions in this order of magnitude. The reason for this lies in the fact that the floater's surge motion is governed by the swell and the floater's characteristics, while the waves have a secondary, higher frequency, effect. Heave and pitch motions are induced by waves that occur at higher frequencies than swell, thus delivering the peak around $f_{red} = 1$.

As the "real" motion regime is significantly different from the motion regimes studied until now, the results regarding realistic motion regimes are expected to behave differently. Figure 4.35 depicts φ for the realistic surge (left hand panel), heave (middle panel) and pitch motion (right hand panel) for all lateral measurement positions. Realistic surge motion has no clear effects on φ. φ fluctuated around 0 for all measurement locations, indicating that the spectral content of the wake is not modified significantly by the presence of realistic surge motion. Similar observations can be made for realistic heave motion (middle panel). Realistic pitch motion (right

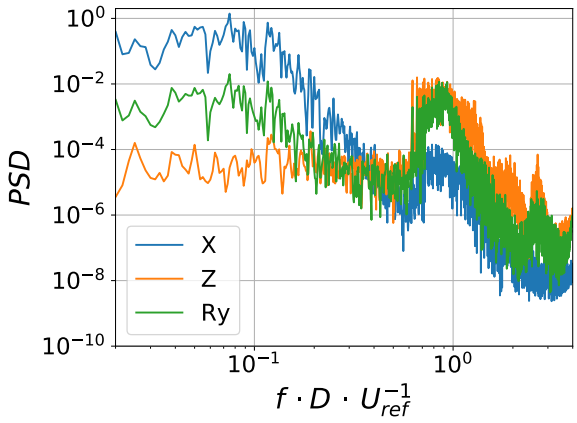

Figure 4.34 – Motion spectrum of the realistic motion profiles of each Dof (X, Z, R_y) studied in the scope of this thesis.

hand panel) appears to induce a shift from low frequencies to higher frequencies. Below $f_{red} = 0.1$ φ is negative, suggesting that energy is removed from the flow in this frequency range compared to the fixed turbine's wake. Above $f_{red} = 0.1$ φ becomes positive for most measurement positions. This confirms the shift to higher frequencies.

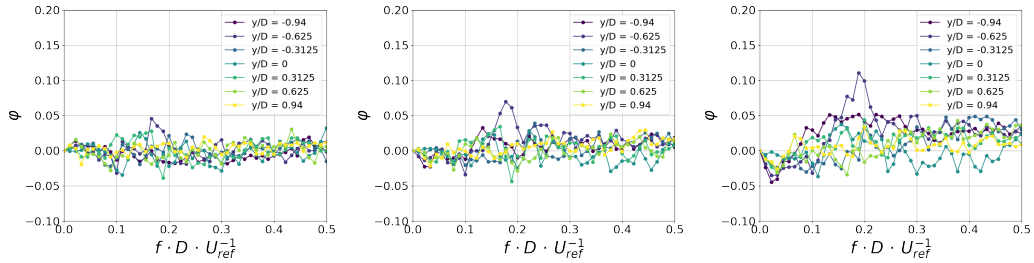

Figure 4.35 – φ for imposed realistic surge (left), heave (centre) and pitch motion (right). Measured 4.6 D downstream at different lateral positions.

Separate but realistic surge and heave motion have limited effects on the spectral content in the wake. Realistic pitch motion induces a frequency shift to higher frequencies. The effects of simultaneous surge, heave and pitch motion will be analysed in the next section.

4.3.3 3D Motion - Idealised and "Real"

In this section the pre-multiplied normalised energy spectra for 3 Dof motion are presented and discussed. Figure 4.36 shows the respective φ for idealised motion (left hand panel) and "real" motion data (right hand panel) measured at 4.6 D. The idealised motion regime uses a combination of characteristic surge ($f_{red} = 0.1$ and $A = 0.125\,D$), heave ($f_{red} = 0.15$ and $A = 0.0125\,D$) and pitch motion ($f_{red} = 0.125$ and $A = 2.5°$). These frequencies are represented by grey dashed lines.

The idealised 3 Dof motion regime does not leave a clear signature in the wake's energy spectra. A weak peak at $f_{red} = 0.1$ is visible for the central measurement positions around $y/D = 0$. The frequency corresponds to the imposed surge motion frequency. A shift towards higher frequencies can not be observed.

A widespread bump between $f_{red} = 0.1$ and $f_{red} = 0.5$ is visible, with a maximum at $f_{red} = 0.2$ for the realistic motion regime. Energy is removed from the low frequency range below $f_{red} = 0.1$ compared to the wake of a fixed turbine (negative φ). A shift from lower to higher frequencies can thus be observed.

Going a step further in looking for a trace of the motion, the coherence between the measured position time series of the model and the flow velocity time series at hub height is calculated. As the left hand panel in figure 4.37 shows, a coherence of 0.64 can be detected at $f_{red} = 0.1$ for the motion produced along the x axis. The other motion frequencies at $f_{red} = 0.125$ (pitch or R_y) and $f_{red} = 0.15$ (heave or z) show weak levels of coherence. The level of coherence at $f_{red} = 0.1$ is in the same order of magnitude as that found between the inflow and the wake (Muller et al.,

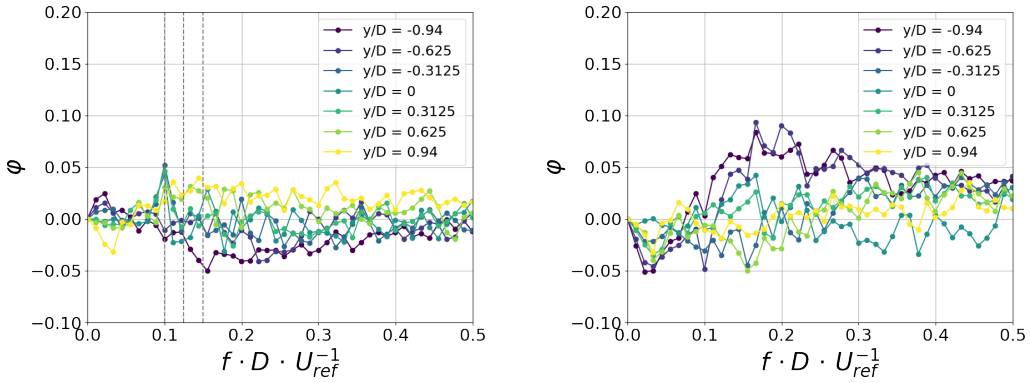

Figure 4.36 – φ at hub height across all lateral positions measured 4.6 D downstream with hot-wire anemometers when the model is subjected to idealised 3 Dof motion (surge, heave, pitch). The left hand panel: idealised 3 Dof motion, right hand panel: "real" 3 Dof motion

2015). No significant coherence can be found between the "real" motion profile and the corresponding velocity (right hand panel). This indicates that the frequency band of the realistic motion incites non-linear processes in the wake. The idealised monochromatic motion appears to have a linear component in its interaction with the wake. This linear component would also be present in a transfer function between the floater's motion spectrum and the wake's energy spectrum. Consequently, the mean flow velocity and turbulence intensity in the wake should be modified to different degrees between the fixed turbine case, the idealised 3 Dof motion and the "real" motion.

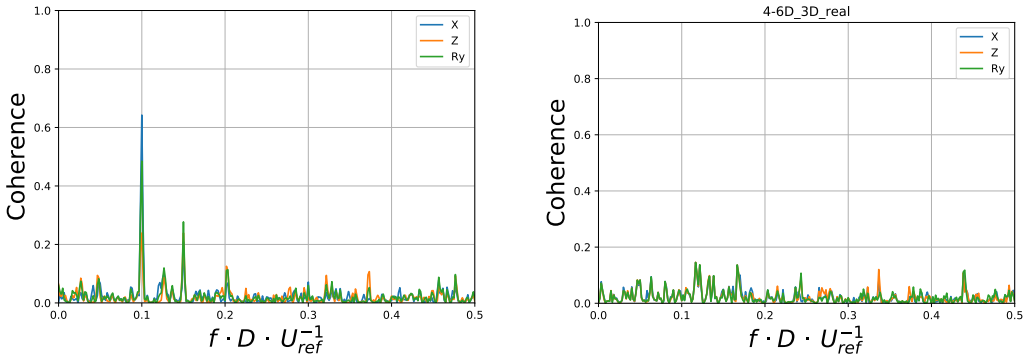

Figure 4.37 – Coherence between the motion time series and the wake flow at hub height 4.6 D downstream from the turbine. Idealised 3 Dof motion (left hand panel) and realistic motion (right hand panel).

Figure 4.38 shows the normalised mean velocity measured at 4.6 D downstream from the model. From top to bottom the panels depict the fixed turbine case, the idealised 3 Dof case and the realistic 3 Dof case, respectively. Each circle represents one measurement point. The circle's size and colour reflect the magnitude of the normalised mean velocity. A larger circle diameter corresponds to a higher velocity. The grey dashed circle represents the area covered by the wind turbine model.

Comparing the three panels it becomes clear that there are notable differences between the three cases. Idealised 3 Dof motion delivers higher mean velocities, especially at the edges of the wake compared to the fixed turbine's wake. The "real" 3 Dof motion also leads to increased mean velocities at the edges, but to a lesser extent, compared to the idealised motion. Overall the mean velocity increases in the wake centre in both cases. The mean velocity is increased at hub height by 0.06 dimensionless velocity units for the idealised 3 Dof case. When applying realistic 3 Dof motion the mean velocity is increased by 0.04 dimensionless velocity units.

The turbulence intensities corresponding to the velocity measurements described above are depicted in figure 4.39. Again the panels show the fixed turbine case, the 3 Dof idealised motion case and the realistic motion case, from top to bottom. The fixed turbine case shows the highest turbulence intensities in the centre of the wake. The turbulence intensity decreases relative to the fixed turbine case for both motion regimes, as indicated by the prevalence of increasingly green colours. The realistic 3 Dof motion delivers the lowest turbulence intensities $4.6\,D$ downstream from the model. Combined with increased mean velocity, the decreased turbulence intensity can be interpreted as an indication for accelerated wake recovery. The turbulence intensity is decreased at hub height by 0.02 for the idealised 3 Dof case. When applying realistic 3 Dof motion the turbulence intensity is decreased by 0.024 at the same location. The wake recovery is modified when realistic motion is applied, compared to idealised motion.

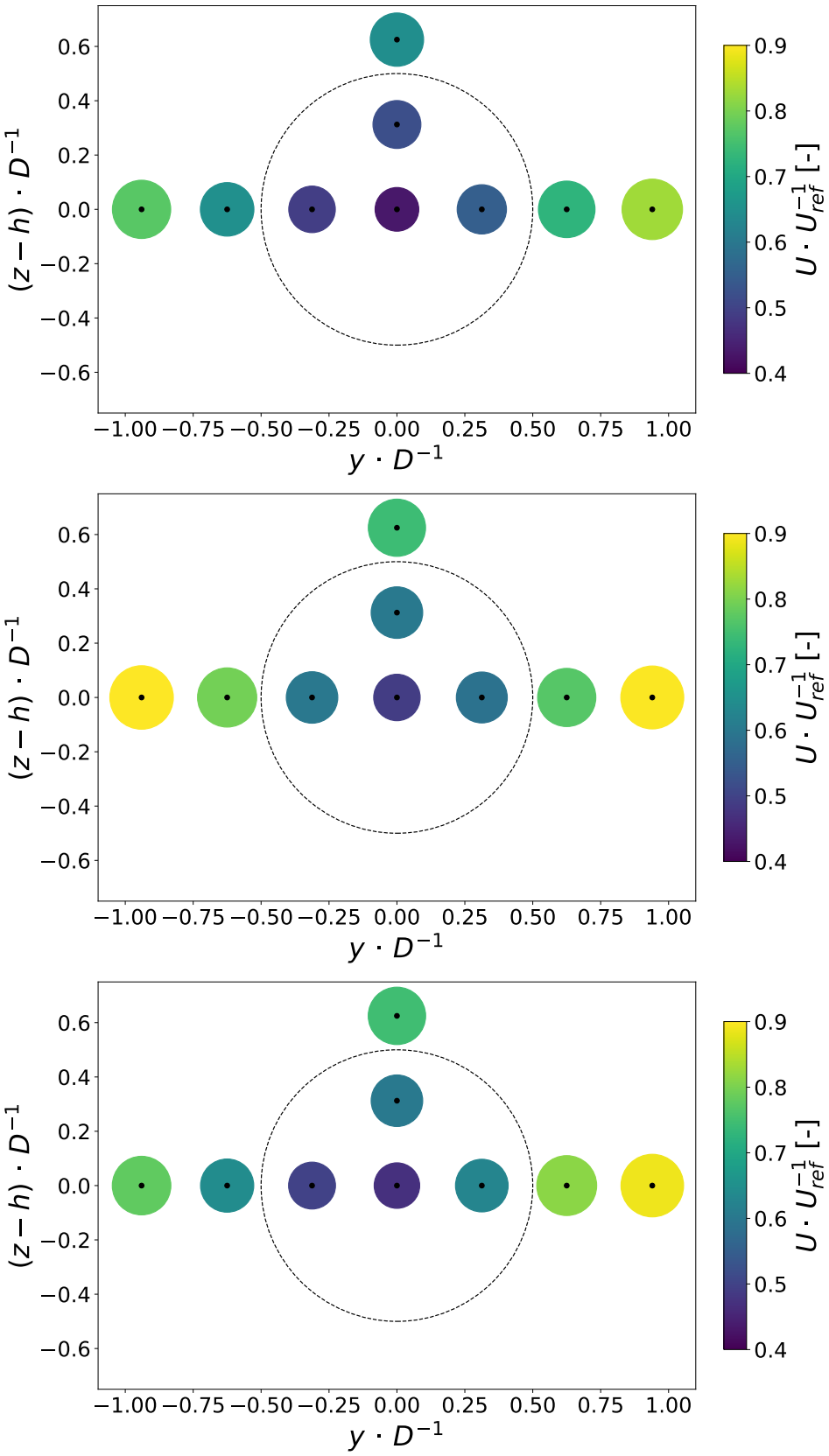

Figure 4.38 – Normalised mean velocity U in the wake of the porous disc model at $4.6\,D$ downstream. Each circle represents one measurement location. The colour and size of the circles indicate the strength of the normalised velocity. The dotted line represents the wind turbine model, for reference.

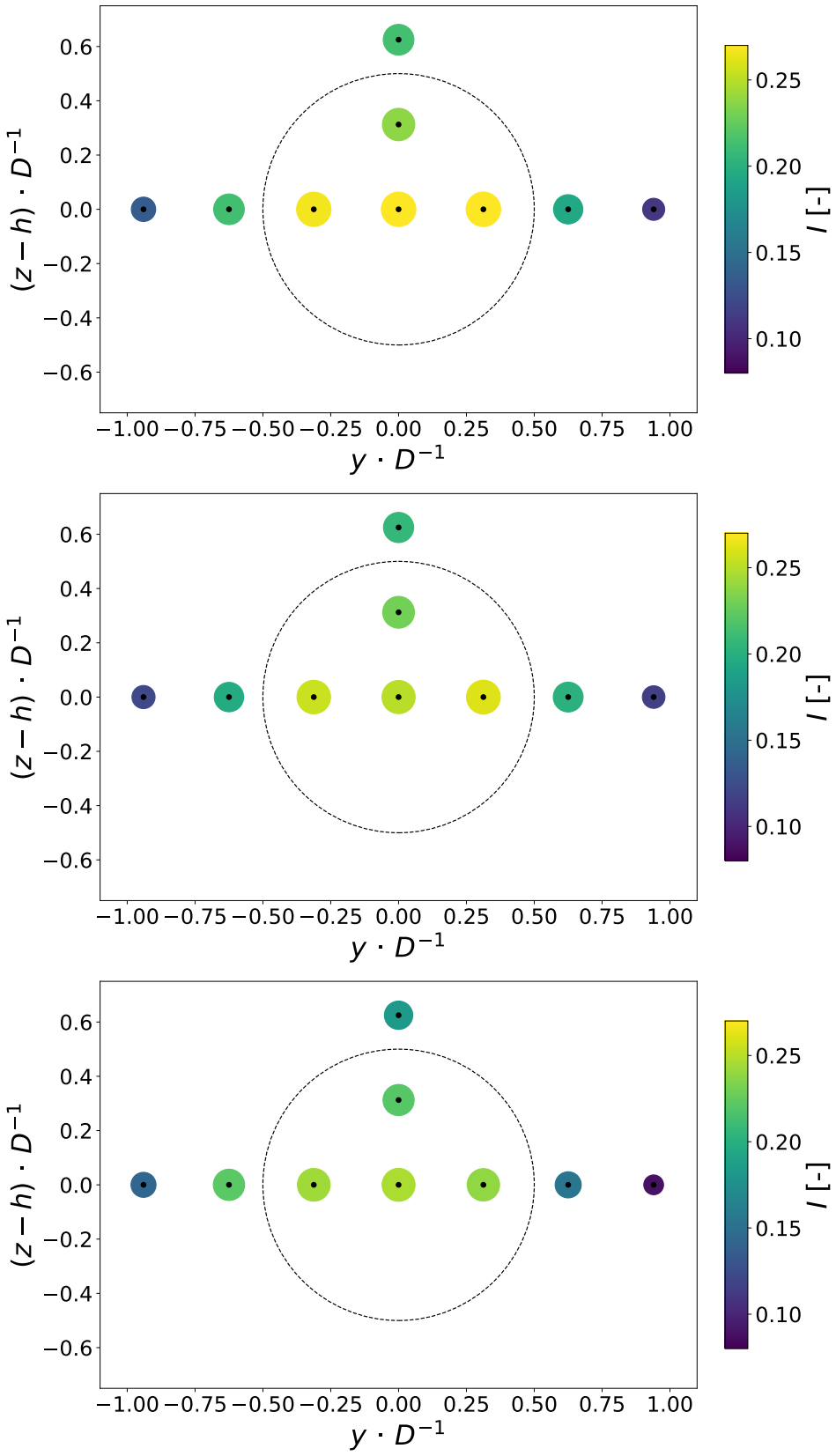

Figure 4.39 – Local turbulence intensity I in the wake of the porous disc model at $4.6\,D$ downstream. Each circle represents one measurement location. The colour and size of the circles indicate the strength of the turbulence intensity. The dotted line represents the wind turbine model, for reference.

Summary

In conclusion, it is found that imposed 1 Dof at sufficiently high frequencies or amplitudes does leave a clear signature in the energy spectra of the wake of a modelled FOWT. This is true for both surge and heave motions. For surge motion the threshold for a minimal frequency lies around $f_{red} = 0.15$ and at amplitudes of at least $0.25\,D$. The longitudinal and vertical flow components are most affected by imposed surge motion. Similar conclusions can be drawn regarding sway, where the longitudinal and lateral flow components are most affected. In contrast to surge, varying the amplitude of sway motion does not affect the peak height in the energy spectrum as clearly. With respect to heave the highest motion frequency tested at $f_{red} = 0.3$ does not leave a clear trace in the spectra. Amplitudes greater than $0.031\,D$ do lead to detectable clear peaks in the energy spectra. Pitch motion at the frequencies and amplitudes tested in this study do not lead to identifiable peaks in the wake.

Idealised characteristic and "real" 3 Dof motions do not deliver a clear signature in the wake's energy spectra. Weak traces of the imposed surge motion can be found, when the model turbine is subjected to idealised 3 Dof motion. No clear signature can be detected for heave and pitch motions. This is most likely due to the small amplitudes present in both the idealised and "real" 3 Dof motion data. As Wei and Dabiri (2021) conclude in their preprint (as of December 2021), the amplitude of motion plays a more important role than the assigned frequency, thus confirming what can be observed in the present study. A shift towards higher frequencies is observed in the wake, when the model is subjected to realistic motion. This could point towards increased turbulent diffusion and would be consistent with the observations presented in section 4.2.3.

For idealised motion the transfer function from the motion spectrum to the wake's energy spectrum has a linear component, as suggested by the coherence at the applied motion frequencies. The lack of coherence with regard to the "real" motion indicates that non-linear interactions between the wake and moving FOWT are predominant. The differences in the normalised mean velocity and turbulence intensity in the wake between the idealised and realistic motion cases can be considered further indicators for non-linear interactions between the moving turbine and its wake. As the induced motion frequencies lie in the range of the most unstable frequencies, as identified by Li et al. (2021), it is not unlikely that non-linear behaviour can be observed.

Chapter 5

Conclusions and Outlook

In this thesis a number of characteristics of the wake of a modelled floating offshore wind turbine (FOWT) was studied. First important achievements were the development of the modelled atmospheric boundary layer in the wind tunnel and the installation of a 3 degree of freedom (Dof) motion system. The central results from the ensuing measurement campaigns reveal some of the characteristics of a FOWT. These results are summarised, starting with the previous work, followed by the measurements. Finally, an outlook into possible future work is given.

5.1 Conclusions

Previous work on FOWT's wakes can be classified into two groups. The first group (Rockel et al., 2014; Hu et al., 2015) state that wakes would replenish more slowly due to decreased shear, while the second group (Fu et al., 2019; Kopperstad et al., 2020; Fontanella et al., 2021) find that the wake recovery is enhanced, with Fu et al. (2019) and Kopperstad et al. (2020) arguing that the accelerated wake recovery is driven by increased shear production. There are a number of fundamental differences between these two sets of studies. Different approaches to generating the motion of the model are employed. The first group allow the flow to induce the motion, while the second group impose the motion externally. This alone will result in different motion regimes as the characteristic lengths and times are different between the air and water. Furthermore the inflow conditions, which significantly modify the wake's characteristics, are not identical.

When considering these two different sets of behaviour, it is necessary to emulate the conditions encountered by an operational FOWT as accurately as possible. This is where the work presented in this thesis aims to contribute to a better understanding. The atmospheric wind tunnel at LHEEA/Centrale Nantes is employed. A model wind turbine is placed in a modelled atmospheric boundary layer flow and subjected to various motions in three separate Dofs (surge, heave and pitch) and in all three Dofs simultaneously. Both idealised and realistic motion regimes are investigated here.

While developing the 3 Dof motion system, a number of observations were made. The 3 Dof motion system consists of two linear motors and a rotational element that can be used modularly. The central control unit allows a versatile use of the system, with a precision of 2% and a temporal resolution of $1\,ms$. There is an offset of $4\,ms$ between the commanded position and the real position. Currently, this motion system is considered to be one of the very few available anywhere.

The other central part of the preparations was the development of a modelled atmospheric boundary layer. The final modelled boundary layer is coherent within itself. The flow fulfils most of the criteria proposed by VDI Guideline 3783 (VDI, 2000), the exception being the roughness length, which is too small. Field data suggests that the roughness length calculated for the modelled boundary layer is in fact realistic for coastal waters (He et al., 2021). A high fidelity boundary layer is important since the turbine's wake is sensitive to the incoming flow (section 2.2.2).

As the actuator disc is central to this work, the assumptions made about constant power and thrust coefficients as well as a constant induction factor were tested using numerical simulations of an FOWT. The analysis revealed that both the mean values and the variability of each quantity are dependent on the sea state. Rough sea conditions lead to modified mean values and increased variability. This limits the applicability of the actuator disc concept when using physical modelling to investigate FOWTs. The porosity of the disc could be varied according to the sea state, yet this would only reflect the modified mean values of C_t, C_p and a and not their increased variability. Further research is also needed to determine the effects of this variability on the wake.

When analysing the PIV data, it was found that the boundary layer can vary more than expected (section 4.2.2). This is most likely related to the long gap between the measurement campaigns. During this time the ambient conditions changed. The modified flow conditions limit the comparability of the data. They also render the normalisation of the data nearly impossible, as the boundary layer thickness changes, affecting all quantities. It is thus recommended that test campaigns be planned in such a manner, that they can be executed in a timely way to avoid the difficulties encountered. The responses to the research questions presented in section 2.4 are given in the following.

How does turbine motion affect the development of the wake?

The overall effect of idealised surge, or sway, motion has limited effect on the mean and turbulent values. The general tendency of the mean and turbulent values points towards slightly accelerated wake recovery processes. This tendency has been confirmed by Fontanella et al. (2021).

Are there differences compared to a stationary model? Overall, the mean quantities are only mildly affected by the introduction of motion. The vertical profiles of the mean and turbulent quantities point in the same direction, showing changes in

the range of 5% for the turbulence intensity. The spatial distribution of the same mean and turbulent quantities is also slightly affected by the introduction of surge motion. Indications of an accelerated wake recovery can be found in the increased levels of wake-added turbulence intensity, TKE and shear stresses for $f_{red} \geq 0.1$ compared to a fixed turbine. These results appear to confirm those discussed in Schliffke et al. (2020). The thicker shear layer and wider areas of increased TKE indicate enhanced mixing processes in the near and medium wake regions (section 4.2.2).

Are the results dependent on the motion's frequency and amplitude? Yes, but the dependence is not always clear. The data suggests that stronger motion has a clearer effect on the wake. Realistic motion seems to have a stronger effect on the wake, when compared to idealised motion (see section 4.3).

What are the physical explanations for the observed differences? The observed enhanced wake recovery is driven by increased momentum transport in the shear layer of the actuator disc's wake, as the TKE budget analysis revealed (section 4.2.3). The momentum transport is increased by about 10% and appears to be independent of the motion frequencies as tested in the scope of this work. Thickened shear layers and larger areas affected by wake-added TKE also point towards enhanced wake recovery processes. It is possible that the actual levels of TKE measured here are underestimated compared to a rotating model turbine (Camp and Cal, 2016). A TKE budget analysis in the wake of a rotating model is thus necessary to verify these results.

Is there an identifiable spectral signature of the turbine's motion on the wake?

Yes, once a certain threshold is surpassed. Imposed 1 Dof motion at sufficiently high frequencies or amplitudes leaves a clear signature in the energy spectra of the wake. This is true for surge, sway and heave motions for the motion regimes tested. For surge motion the threshold for a minimal frequency lies around $f_{red} = 0.15$ and at amplitudes of $0.25\,D$. Even the highest motion frequency tested for heave at $f_{red} = 0.3$ does not deliver clear traces in the spectra at an amplitude of $0.0125\,D$. Interestingly, amplitudes greater than $0.03125\,D$ do lead to detectable peaks in the energy spectrum. The frequencies and amplitudes tested for pitch motion do not show identifiable peaks in the wake's energy spectrum. Further detailed experiments are needed to better define these thresholds. Idealised characteristic 3 Dof motion shows a small peak associated to surge motion. Surge motion is the dominant Dof in the idealised 3 Dof motion regime. Realistic 3 Dof motions also do not show clear peaks in the wake flow's energy spectra.

How does the unsteady response of the wake develop laterally and vertically? The signature can still be detected at $4.6\,D$ in cases where the motion is strong enough. How far downstream the motion's signature can be detected remains to

be established in future work. Laterally, the clearest signature can be found along the centre line of the turbine at hub height. The effects of the motion become less clear towards the edges of the wake. Vertically, the shear layer, which is located just above the top tip of the turbine, shows the strongest peaks in the energy spectra.

Are all flow components affected equally by the imposed motion? The longitudinal and vertical flow components are affected by imposed surge motion. When imposing sway motion, longitudinal and lateral flow components show clear responses in the wake's energy spectra. In contrast to surge, varying the amplitude of sway motion does not affect the peak height as clearly.

Is the wake's unsteady response dependent on the motion's frequency and amplitude? Yes. This is most clear when applying idealised and realistic 3 Dof motion. Regarding idealised 3 Dof motion, the coherence between the motion spectrum and wake flow shows a clear response for the imposed surge motion frequency, while weak responses can be identified at the imposed heave and pitch frequencies. This indicates that the transfer function from the floater's motion spectrum to the wake's energy spectrum has a linear component. The lack of coherence with regard to the realistic motion indicates that non-linear interactions between the wake and moving FOWT are predominant. The differences in the normalised mean velocity and turbulence intensity in the wake between the idealised and realistic motion cases can be considered further indicators for non-linear interactions between the moving turbine and its wake. The results point towards modified wake recovery processes for realistic motion compared to idealised motion. As the induced motion frequencies lie in the range of the most unstable frequencies, as identified by Li et al. (2021), it is not unlikely that non-linear behaviour can be observed.

5.2 Outlook

The data collected in the course of this work can be used for future research of a number of topics. Further in-depth analysis of the time series measured with the Cobra probe or the rake of hot-wires should be considered. In this context an analysis of the intermittency of the flow would be of interest, as an indicator for the "gustiness" as a function of the imposed motion (e.g. Kadum et al., 2021). The central question here would be to determine the degree of additional material fatigue and variations in power production encountered by a downstream turbine.

A targeted measurement of the shear layer of the moving wind turbine can also be of considerable added value. Combining stereoscopic PIV (S-PIV) and high frequency hot-wire measurements can help improve the estimation of the TKE budget in the shear layer. The hot-wire anemometers would be used to measure diffusive processes, thus reducing the error imposed on the dissipation estimation, when applying the LE-PIV method. The targeted application of S-PIV would deliver the other terms of the TKE budget equation with a significantly improved spatial resolution compared to the data used in the scope of this thesis.

The hot-wire rake data enables the application of wake tracing algorithms (e.g. Aubrun et al., 2015). The main question here concerns the wake's meandering dependency on the induced motion. This is of special interest as the downstream turbines are directly impacted by wake meandering, both in terms of fatigue and power production. A dependency of the meandering process on the sea conditions encountered by the FOWT can be expected as the energy spectra of the flow presented in this work are impacted by the imposed motion.

The differences between an actuator disc and a rotating turbine have been investigated by Camp and Cal (2016) for the case of a fixed turbine. There is justifiable interest in conducting a similar systematic comparison between the two model types for FOWT modelling. Camp and Cal (2016) have observed differences in the TKE budgets particularly in the near wake of the turbine model. As described above, the introduction of motion can change parts of the TKE budget, thus begging the question what differences can be observed between an actuator disc and a rotating model. Another point of interest is the observed shift towards higher frequencies in the wake of the porous disc model as used in this thesis. The frequency shift has a positive effect on the wake as it enhances turbulent diffusion. The cause of the frequency shift is not clearly identifiable with the data at hand. It could be related solely to the induced motion, in which case the same effects can be measured in the wake of a rotating model. The frequency shift could also be related to the porosity of the disc, as it introduces grid scale turbulence to its wake flow. An extensive round robin test between a rotating turbine model and an actuator disc would clarify the issues raised above regarding the modified TKE budget and the observed frequency shift.

It is also advisable to investigate the effects of the variability of C_t, C_p and a on the wake of a moving actuator disc model. The aim would be to test the limits in the representativeness of the actuator disc concept in the context of FOWTs. What are acceptable degrees of variability? Depending on the response to the question the sea conditions investigated may have to be limited to calmer seas.

It would also be of interest to repeat the analysis conducted in Muller et al. (2015). The authors find a high degree of coherence between inflow and the wake using hot-wire anemometry. A similar set-up could be using with an FOWT model subjected to idealised and realistic 3 Dof motion. The aim would be to determine the effect of the motion on the governing scales in the wake of an FOWT, relative to the dominant scales in the inflow. In this context, the necessary steps to determine the transfer function from the floater's motion spectrum to the wake's energy spectrum could also be undertaken.

In the context of FOWT farms the question of the effects of motion on the interaction between the first turbine's wake and that of a second downstream turbine can be investigated. A starting point could be to subject both turbines to idealised and then realistic motion. The interaction between the wakes can then be studied. It is likely that monochromatic motion has significantly different effects on the wake

interactions from realistic motion, since only one frequency is excited. A phase shift between the motion regimes could also be introduced to add another degree of realism to the experiment.

In the future, it is advisable to use motion time series derived from marine wave spectra to better reflect the conditions encountered by an FOWT. As observed in this thesis, the wake can react differently if excited by monochromatic motion or by a larger frequency band. Idealised motion is a good point of departure but may lead to conclusions with limited validity in more complex scenarios.

Appendix

Installation of Corner Fillets

Figure A1 shows the resulting measurements after the installation of the corner fillets at the centre and the right hand side of the wind tunnel. The blue data represents the measurements with corner fillets, while the orange data shows the data without corner fillets.

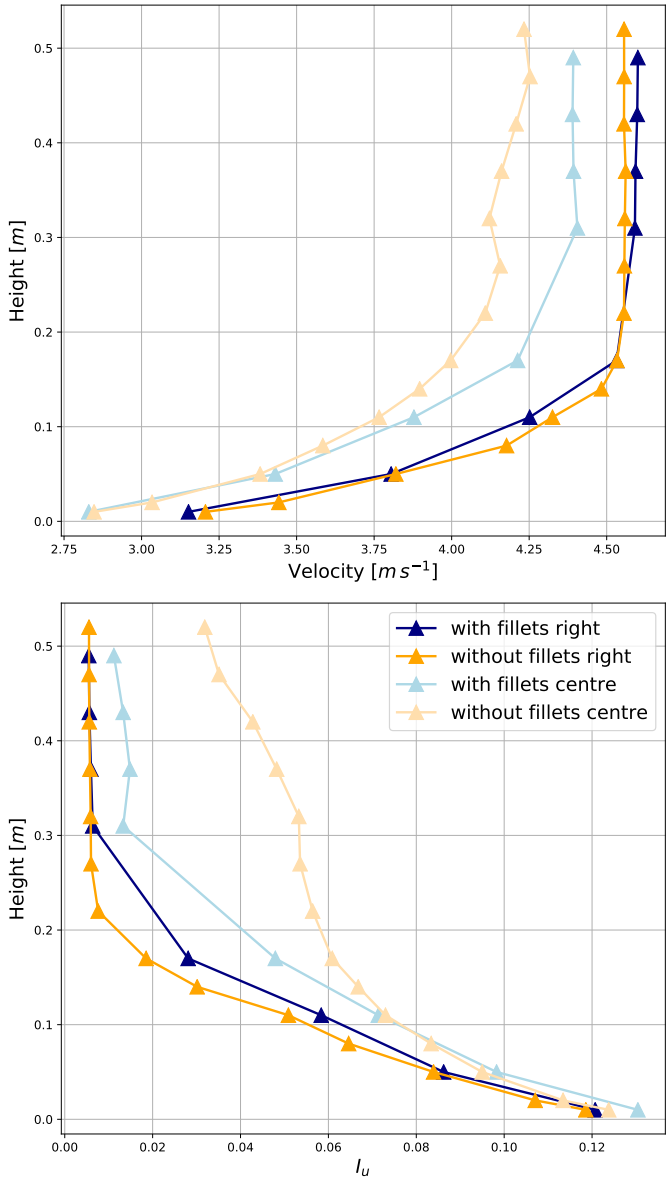

Figure A1 – Mean magnitude and turbulence intensity in the centre of the wind tunnel with corner fillets. The orange profiles represent measurements without corner fillets. The x-axis shows the velocity (top, in $[m\,s^{-1}]$) and turbulence intensity (bottom).

Cobra Probe's Sensitivity

The following list describes the tests conducted to better understand the Cobra probe's sensitivity:

- v1: original offset of the initial time-series (afternoon)
- v2: offset of a measurement conducted in the morning applied to the initial time-series
- v3: probe head covered, static open, wait 3 minutes between closing doors and measurement, engine off
- v4: probe head covered, static covered, wait 3 minutes between closing doors and measurement, engine off
- v5: probe head covered, static open, wait 3 minutes between closing doors and measurement, engine off
- v6: probe head open, static open, wait 3 minutes between closing doors and measurement, engine off
- v7: probe head open, static open, wait 3 minutes between closing doors and measurement, engine on at 0 RPM
- v8: probe head covered, static covered, wait 3 minutes between closing doors and measurement, engine on at 0 RPM
- v9: probe head covered, static covered, wait 3 minutes between closing doors and measurement, engine off
- v10: probe head covered, static covered, wait 3 minutes between closing doors and measurement, engine off
- v11: probe head covered, static covered, wait 3 minutes between closing doors and measurement, engine off, in post-processing tool: ambient pressure at 1030.15 hPa, ambient temperature at 15°C
- v12: probe head covered, static covered, wait 3 minutes between closing doors and measurement, engine off, in post-processing tool: ambient pressure at 1013.25 hPa, ambient temperature at 30°C

Figure A2 shows the resulting measurements of the different test cases presented above (next page):

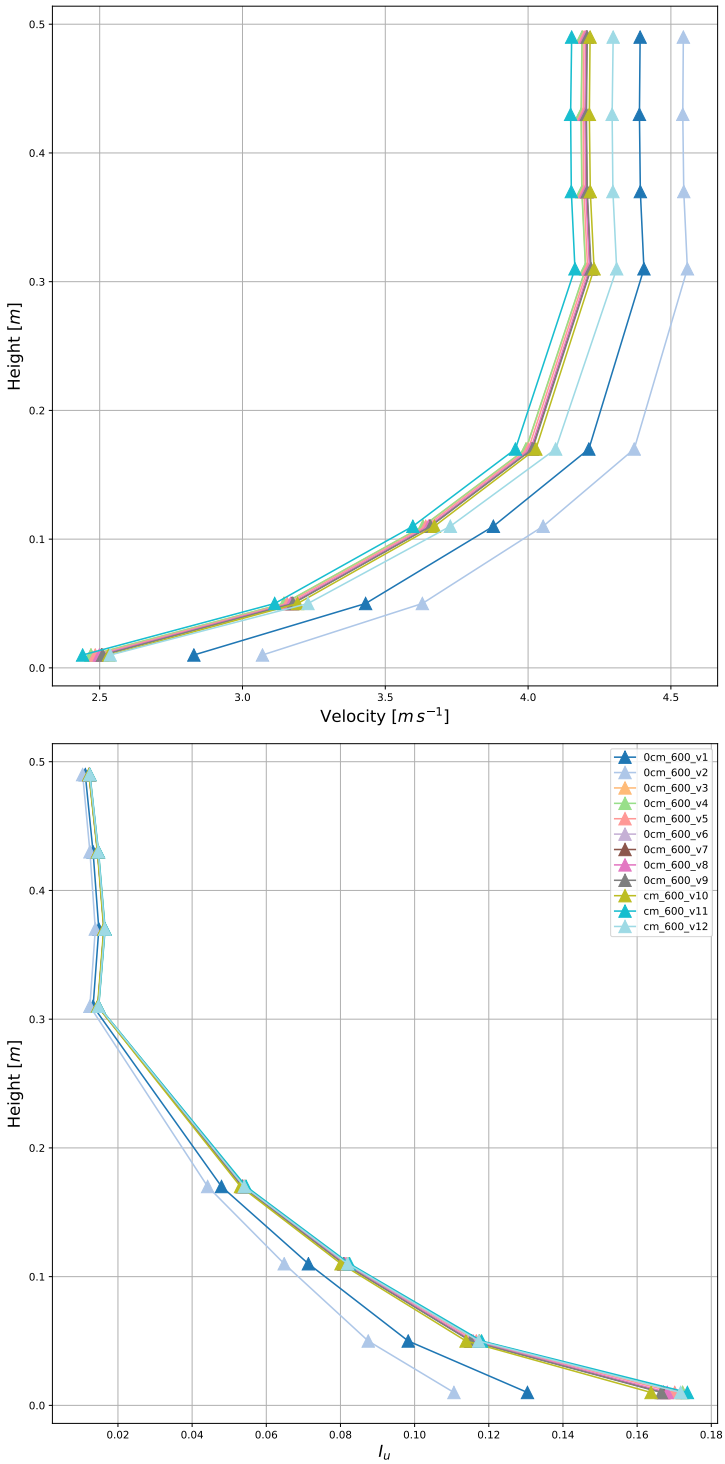

Figure A2 – Mean magnitude and turbulence intensity in the centre of the wind tunnel with corner fillets. Each profile represents one of the test cases mentioned in the list above. The x-axis shows the velocity (top, in $[m\,s^{-1}]$) and turbulence intensity (bottom).

3 Dof Motion System

Figure A3 shows the installed 3 Dof motion system. The coloured boxes indicate the positions of the three actuators that compose the 3 Dof system.

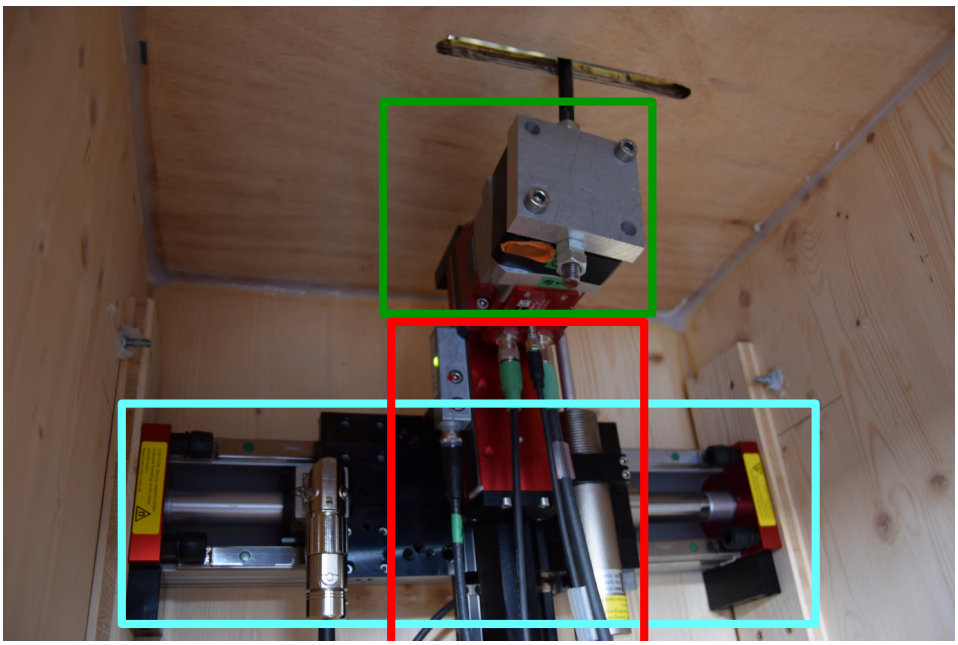

Figure A3 – Photo of the 3 Dof motion system installed in its airtight case under the atmospheric wind tunnel. The light blue box encompasses the x axis, the red box the z axis and the green box the R_y actuator.

Bibliography

Abkar, M. and Porté-Agel, F. (2015). Influence of atmospheric stability on wind-turbine wakes: A large-eddy simulation study. *Physics of Fluids*, 27(3):035104.

Archer, C. L., Vasel-Be-Hagh, A., Yan, C., Wu, S., Pan, Y., Brodie, J. F., and Maguire, A. E. (2018). Review and evaluation of wake loss models for wind energy applications. *Applied Energy*, 226:1187–1207.

Aubrun, S., Bastankhah, M., Cal, R. B., Conan, B., Hearst, R. J., Hoek, D., Hölling, M., Huang, M., Hur, C., Karlsen, B., et al. (2019). Round-robin tests of porous disc models. *Journal of Physics: Conference Series*, 1256(1):012004.

Aubrun, S., Loyer, S., Hancock, P., and Hayden, P. (2013). Wind turbine wake properties: Comparison between a non-rotating simplified wind turbine model and a rotating model. *Journal of Wind Engineering and Industrial Aerodynamics*, 120:1–8.

Aubrun, S., Muller, Y., and Masson, C. (2015). Predicting wake meandering in real-time through instantaneous measurements of wind turbine load fluctuations. *Journal of Physics: Conference Series*, 625(1):012005.

Bastankhah, M. and Porté-Agel, F. (2014). A new analytical model for wind-turbine wakes. *Renewable Energy*, 70:116–123.

Bastankhah, M. and Porté-Agel, F. (2016). Experimental and theoretical study of wind turbine wakes in yawed conditions. *Journal of Fluid Mechanics*, 806:506–541.

Berger, F., Kröger, L., Onnen, D., Petrović, V., and Kühn, M. (2018). Scaled wind turbine setup in a turbulent wind tunnel. *Journal of Physics: Conference Series*, 1104(1):012026.

Blackman, K., Perret, L., Calmet, I., and Rivet, C. (2017). Turbulent kinetic energy budget in the boundary layer developing over an urban-like rough wall using PIV. *Physics of Fluids*, 29(8):085113.

Blondel, F. and Cathelain, M. (2020). An alternative form of the super-Gaussian wind turbine wake model. *Wind Energy Science*, 5(3):1225–1236.

Bottasso, C. L., Campagnolo, F., and Petrović, V. (2014). Wind tunnel testing of scaled wind turbine models: Beyond aerodynamics. *Journal of Wind Engineering and Industrial Aerodynamics*, 127:11–28.

Bruun, H. and Bruun, L. (1995). *Hot-wire Anemometry: Principles and Signal Analysis*. Oxford Science Publications. Oxford University Press.

Buckingham, E. (1914). On physically similar systems: illustrations of the use of dimensional equations. *Physical Review*, 4(4):345.

Burton, T., Jenkins, N., Sharpe, D., and Bossanyi, E. (2011). *Wind Energy Handbook*. John Wiley & Sons.

Butterfield, S., Musial, W., Jonkman, J., and Sclavounos, P. (2007). Engineering challenges for floating offshore wind turbines. Technical report, National Renewable Energy Lab.(NREL), Golden, CO (United States).

BW Ideol, Centrale Nantes (2014). FLOATGEN Press Kit. `https://floatgen.eu/sites/default/files/medias/press_kit_-_floatgen.pdf`. Accessed: 2021-12-10.

Camp, E. H. and Cal, R. B. (2016). Mean kinetic energy transport and event classification in a model wind turbine array versus an array of porous disks: Energy budget and octant analysis. *Physical Review Fluids*, 1(4):044404.

Campagnolo, F., Petrović, V., Schreiber, J., Nanos, E. M., Croce, A., and Bottasso, C. L. (2016). Wind tunnel testing of a closed-loop wake deflection controller for wind farm power maximization. *Journal of Physics: Conference Series*, 753(3):032006.

Canet, H., Bortolotti, P., and Bottasso, C. L. (2021). On the scaling of wind turbine rotors. *Wind Energy Science*, 6(3):601–626.

Chamorro, L. P., Arndt, R., and Sotiropoulos, F. (2012). Reynolds number dependence of turbulence statistics in the wake of wind turbines. *Wind Energy*, 15(5):733–742.

Chamorro, L. P. and Porté-Agel, F. (2009). A wind-tunnel investigation of wind-turbine wakes: boundary layer turbulence effects. *Boundary Layer Meteorology*, 132(1):129–149.

Chamorro, L. P. and Porté-Agel, F. (2010). Effects of thermal stability and incoming boundary layer flow characteristics on wind-turbine wakes: a wind-tunnel study. *Boundary Layer Meteorology*, 136(3):515–533.

Churchfield, M. J., Lee, S., Moriarty, P. J., Hao, Y., Lackner, M. A., Barthelmie, R., Lundquist, J. K., and Oxley, G. (2015). A comparison of the dynamic wake

meandering model, large-eddy simulation, and field data at the egmond aan zee offshore wind plant. *33rd Wind Energy Symposium*, page 0724.

Counihan, J. (1975). Adiabatic atmospheric boundary layers: a review and analysis of data from the period 1880–1972. *Atmospheric Environment*, 9(10):871–905.

Espana, G., Aubrun, S., Loyer, S., and Devinant, P. (2011). Spatial study of the wake meandering using modelled wind turbines in a wind tunnel. *Wind Energy*, 14(7):923–937.

Espana, G., Aubrun, S., Loyer, S., and Devinant, P. (2012). Wind tunnel study of the wake meandering downstream of a modelled wind turbine as an effect of large scale turbulent eddies. *Journal of Wind Engineering and Industrial Aerodynamics*, 101:24–33.

Etling, D. (2008). Theoretical Meteorology. An Introduction. 3. enlarged and updated edition; Theoretische Meteorologie. Eine Einfuehrung.

Fontanella, A., Bayati, I., Mikkelsen, R., Belloli, M., and Zasso, A. (2021). UNAFLOW: a holistic experiment about the aerodynamics of floating wind turbines under imposed surge motion. *Wind Energy Science Discussions*, pages 1–29.

Frandsen, S., Barthelmie, R., Pryor, S., Rathmann, O., Larsen, S., Højstrup, J., and Thøgersen, M. (2006). Analytical modelling of wind speed deficit in large offshore wind farms. *Wind Energy: An International Journal for Progress and Applications in Wind Power Conversion Technology*, 9(1-2):39–53.

Frederik, J. A., Weber, R., Cacciola, S., Campagnolo, F., Croce, A., Bottasso, C., and van Wingerden, J.-W. (2020). Periodic dynamic induction control of wind farms: proving the potential in simulations and wind tunnel experiments. *Wind Energy Science*, 5(1):245–257.

Frost, W. (2012). *Handbook of Turbulence: Volume 1 Fundamentals and Applications*. Springer Science & Business Media.

Fu, S., Jin, Y., Zheng, Y., and Chamorro, L. P. (2019). Wake and power fluctuations of a model wind turbine subjected to pitch and roll oscillations. *Applied Energy*, 253:113605.

Garcia, E. T., Aubrun, S., Coupiac, O., Girard, N., and Boquet, M. (2019). Statistical characteristics of interacting wind turbine wakes from a 7-month LiDAR measurement campaign. *Renewable Energy*, 130:1–11.

Harms, F. (2010). *Systematische Windkanaluntersuchungen zur Charakterisierung instationärer Ausbreitungsprozesse einzelner Gaswolken in urbanen Rauigkeitsstrukturen*. PhD thesis, Meteorologisches Institut Universität Hamburg.

He, Y., Fu, J., Chan, P. W., Li, Q., Shu, Z., and Zhou, K. (2021). Reduced Sea-Surface Roughness Length at a Coastal Site. *Atmosphere*, 12(8):991.

Hegazy, A., Blondel, F., Cathelain, M., and Aubrun, S. (2021). Lidar and scada data processing for interacting wind turbine wakes with comparison to analytical wake models. *Renewable Energy*, 181:457–471.

Heronemus, W. E. (1972). Pollution-free energy from offshore winds. *8th Annual Conference and Exposition, Marine Technology Society, Sep. 11-13, 1972, Washington, DC*.

Holton, J. R. (2004). *An Introduction to Dynamic Meteorology*. International Geophysics Series. Elsevier Academic Press, Burlington, MA, 4 edition.

Howard, K. B., Singh, A., Sotiropoulos, F., and Guala, M. (2015). On the statistics of wind turbine wake meandering: An experimental investigation. *Physics of Fluids*, 27(7):075103.

Hu, H., Morteza Khosravi, M., and Sarkar, P. (2015). An experimental investigation on the performance and the wake characteristics of a wind turbine subjected to surge motion. *33rd Wind Energy Symposium*.

Hunter, J. D. (2007). Matplotlib: A 2d graphics environment. *Computing in Science Engineering*, 9(3):90–95.

IEA (2019). Offshore Wind Outlook 2019. `https://www.iea.org/reports/offshore-wind-outlook-2019`. Accessed: 2021-12-05.

Jensen, N. O. (1983). A note on wind generator interaction.

Johl, G. (2010). *The design and performance of a 1.9 m x 1.3 m indraft wind tunnel*. PhD thesis, Loughborough University.

Kadum, H., Rockel, S., Hölling, M., Peinke, J., and Cal, R. B. (2019). Wind turbine wake intermittency dependence on turbulence intensity and pitch motion. *Journal of Renewable and Sustainable Energy*, 11(5):053302.

Kadum, H., Rockel, S., Viggiano, B., Dib, T., Hölling, M., Chevillard, L., and Cal, R. B. (2021). Assessing intermittency characteristics via cumulant analysis of floating wind turbines wakes. *Journal of Renewable and Sustainable Energy*, 13(1):013302.

Kaimal, J. C., Wyngaard, J., Izumi, Y., and Coté, O. (1972). Spectral characteristics of surface-layer turbulence. *Quarterly Journal of the Royal Meteorological Society*, 98(417):563–589.

King, L. V. (1914). On the convection of heat from small cylinders in a stream of fluid: Determination of the convection constants of small platinum wires with

applications to hot-wire anemometry. *Philosophical Transactions of the Royal Society of London. Series A, Containing Papers of a Mathematical or Physical Character*, 214(509-522):373–432.

Kopperstad, K. M., Kumar, R., and Shoele, K. (2020). Aerodynamic characterization of barge and spar type floating offshore wind turbines at different sea states. *Wind Energy*, 23(11):2087–2112.

Larsen, G. C. (1988). A simple wake calculation procedure. *Risø National Laboratory*.

Larsen, G. C., Aagaard Madsen, H., and Bingöl, F. (2007). Dynamic wake meandering modeling.

Larsen, G. C., Madsen, H. A., Thomsen, K., and Larsen, T. J. (2008). Wake meandering: a pragmatic approach. *Wind Energy: An International Journal for Progress and Applications in Wind Power Conversion Technology*, 11(4):377–395.

Lee, H. and Lee, D.-J. (2019). Effects of platform motions on aerodynamic performance and unsteady wake evolution of a floating offshore wind turbine. *Renewable Energy*, 143:9–23.

Li, Z., Dong, G., and Yang, X. (2021). Onset of wake meandering for a floating offshore wind turbine under side-to-side motion. *arXiv preprint arXiv:2107.13842*.

Lignarolo, L., Ragni, D., Krishnaswami, C., Chen, Q., Ferreira, C. S., and Van Bussel, G. (2014). Experimental analysis of the wake of a horizontal-axis wind-turbine model. *Renewable Energy*, 70:31–46.

Liu, Y., Xiao, Q., Incecik, A., Peyrard, C., and Wan, D. (2017). Establishing a fully coupled CFD analysis tool for floating offshore wind turbines. *Renewable Energy*, 112:280–301.

Mehta, R. D. and Bradshaw, P. (1979). Design rules for small low speed wind tunnels. *The Aeronautical Journal*, 83(827):443–453.

Mohamed, M. S. and Larue, J. C. (1990). The decay power law in grid-generated turbulence. *Journal of Fluid Mechanics*, 219:195–214.

Monin, A. S. and Obukhov, A. M. (1954). Osnovnye zakonomernosti turbulentnogo peremesivanija v prizemnom sloe atmosfery. *Trudy geofiz. inst. AN SSSR*, 24:163–187.

Muller, Y.-A., Aubrun, S., and Masson, C. (2015). Determination of real-time predictors of the wind turbine wake meandering. *Experiments in Fluids*, 56(3):1–11.

Munters, W. and Meyers, J. (2018). Towards practical dynamic induction control of wind farms: analysis of optimally controlled wind-farm boundary layers and sinusoidal induction control of first-row turbines. *Wind Energy Science*, 3(1):409–425.

Murata, J., Endo, M., Maeda, T., Kamada, Y., et al. (2016). Experimental and numerical investigation of the effect of turbulent inflow on a Horizontal Axis Wind Turbine (part II: Wake characteristics). *Energy*, 113:1304–1315.

Musial, W., Butterfield, S., and Boone, A. (2004). Feasibility of floating platform systems for wind turbines. *42nd AIAA Aerospace Sciences Meeting and Exhibit*.

Neunaber, I., Hölling, M., Whale, J., and Peinke, J. (2021). Comparison of the turbulence in the wakes of an actuator disc and a model wind turbine by higher order statistics: A wind tunnel study. *Renewable Energy*, 179:1650–1662.

Parada, L., Herrera, C., Flores, P., and Parada, V. (2017). Wind farm layout optimization using a Gaussian-based wake model. *Renewable Energy*, 107:531–541.

Pope, S. B. (2000). *Turbulent flows*. Cambridge University Press.

Porté-Agel, F., Bastankhah, M., and Shamsoddin, S. (2019). Wind-Turbine and Wind-Farm Flows: A Review. *Boundary Layer Meteorology*.

Raffel, M., Kompenhans, J., Wereley, S. T., and Willert, C. E. (2007). *Particle image velocimetry: a practical guide*. Springer.

Ramos-García, N., Kontos, S., Pegalajar-Jurado, A., González Horcas, S., and Bredmose, H. (2021). Investigation of the floating IEA Wind 15 MW RWT using vortex methods Part I: Flow regimes and wake recovery. *Wind Energy*.

Rockel, S., Camp, E., Schmidt, J., Peinke, J., Cal, R., and Hölling, M. (2014). Experimental study on influence of pitch motion on the wake of a floating wind turbine model. *Energies*, 7(4):1954–1985.

Rockel, S., Peinke, J., Hölling, M., and Cal, R. B. (2016). Wake to wake interaction of floating wind turbine models in free pitch motion: An eddy viscosity and mixing length approach. *Renewable Energy*, 85:666–676.

Rodrigues, S., Pinto, R. T., Soleimanzadeh, M., Bosman, P. A., and Bauer, P. (2015). Wake losses optimization of offshore wind farms with moveable floating wind turbines. *Energy Conversion and Management*, 89:933–941.

Schliffke, B., Aubrun, S., and Conan, B. (2020). Wind Tunnel Study of a "Floating" Wind Turbine's Wake in an Atmospheric Boundary Layer with Imposed Characteristic Surge Motion. *Journal of Physics: Conference Series*, 1618:062015.

Sclavounos, P. (2008). Floating offshore wind turbines. *Marine Technology Society Journal*, 42(2):39–43.

Sebastian, T. and Lackner, M. (2012a). Analysis of the induction and wake evolution of an offshore floating wind turbine. *Energies*, 5(4):968–1000.

Sebastian, T. and Lackner, M. (2013). Characterization of the unsteady aerodynamics of offshore floating wind turbines. *Wind Energy*, 16(3):339–352.

Sebastian, T. and Lackner, M. A. (2012b). Development of a free vortex wake method code for offshore floating wind turbines. *Renewable Energy*, 46:269–275.

Sheng, J., Meng, H., and Fox, R. (2000). A large eddy PIV method for turbulence dissipation rate estimation. *Chemical Engineering Science*, 55(20):4423–4434.

Snyder, W. (1981). *Guideline for fluid modeling of atmospheric diffusion.* Research and development / United States Environmental Protection Agency. Environmental Sciences Research Laboratory, Office of Research and Development, U.S. Environmental Protection Agency.

Stevens, R. J. and Meneveau, C. (2017). Flow structure and turbulence in wind farms. *Annual Review of Fluid Mechanics*, 49:311–339.

Stull, R. (1988). *An Introduction to Boundary Layer Meteorology.* Atmospheric and Oceanographic Sciences Library. Springer Netherlands.

Tarpin, G. (2018). Physical Modelling of Floating Offshore Wind Turbines Inside a Wind Tunnel. Technical report, Centrale Nantes.

Taylor, G. I. (1938). The spectrum of turbulence. *Proceedings of the Royal Society of London A: Mathematical, Physical and Engineering Sciences*, 164:476–490.

Tian, G. and Xiao, Z. (2020). New insight on large-eddy simulation of flow past a circular cylinder at subcritical reynolds number 3900. *AIP Advances*, 10(8):085321.

Toba, Y. and Ebuchi, N. (1991). Sea-surface roughness length fluctuating in concert with wind and waves. *Journal of the Oceanographical Society of Japan*, 47(3):63–79.

Townsend, A. A. (1976). *The structure of turbulent shear flow* 2^{nd} *edition.* Cambridge and New York, Cambridge University Press.

Tran, T.-T. and Kim, D.-H. (2015). The platform pitching motion of floating offshore wind turbine: A preliminary unsteady aerodynamic analysis. *Journal of Wind Engineering and Industrial Aerodynamics*, 142:65–81.

Turbulent Flow Instruments (2015). *Getting Started Series 100 Cobra Probe (v3.7).*

Van der Hoven, I. (1957). Power spectrum of horizontal wind speed in the frequency range from 0.0007 to 900 cycles per hour. *Journal of Meteorology*, 14(2):160–164.

VDI (2000). Umweltmeteorologie - Physikalische Modellierung von Strömungs- und Ausbreitungsvorgängen in der atmosphärischen Grenzschicht - Windkanalanwendungen. Technical report, VDI Verein Deutscher Ingenieure e.V., VDI-Platz 1, 40468 Düsseldorf, Germany.

Vermeer, L., Sørensen, J. N., and Crespo, A. (2003). Wind turbine wake aerodynamics. *Progress in Aerospace Sciences*, 39(6-7):467–510.

Virtanen, P., Gommers, R., Oliphant, T. E., Haberland, M., Reddy, T., Cournapeau, D., Burovski, E., Peterson, P., Weckesser, W., Bright, J., van der Walt, S. J., Brett, M., Wilson, J., Millman, K. J., Mayorov, N., Nelson, A. R. J., Jones, E., Kern, R., Larson, E., Carey, C. J., Polat, İ., Feng, Y., Moore, E. W., VanderPlas, J., Laxalde, D., Perktold, J., Cimrman, R., Henriksen, I., Quintero, E. A., Harris, C. R., Archibald, A. M., Ribeiro, A. H., Pedregosa, F., van Mulbregt, P., and SciPy 1.0 Contributors (2020). SciPy 1.0: Fundamental Algorithms for Scientific Computing in Python. *Nature Methods*, 17:261–272.

Von Karman, T. (1948). Progress in the statistical theory of turbulence. *Proceedings of the National Academy of Sciences of the United States of America*, 34(11):530.

Wang, C., Campagnolo, F., Canet, H., Barreiro, D. J., and Bottasso, C. L. (2021). How realistic are the wakes of scaled wind turbine models? *Wind Energy Science*, 6(3):961–981.

Wang, J., Wang, C., Castañeda, O., Campagnolo, F., and Bottasso, C. (2018). Large-eddy simulation of scaled floating wind turbines in a boundary layer wind tunnel. *Journal of Physics: Conference Series*, 1037(7):072032.

Wei, N. J. and Dabiri, J. O. (2021). Phase-Averaged Dynamics of a Periodically Surging Wind Turbine. *arXiv preprint arXiv:2110.10312*.

WindEurope (2020). Floating Offshore Wind Energy - A Policy Blueprint for Europe. `https://windeurope.org/wp-content/uploads/files/policy/position-papers/Floating-offshore-wind-energy-a-policy-blueprint-for-Europe.pdf`. Accessed: 2021-12-05.

Wise, A. S. and Bachynski, E. E. (2020). Wake meandering effects on floating wind turbines. *Wind Energy*, 23(5):1266–1285.

Xie, S. and Archer, C. (2015). Self-similarity and turbulence characteristics of wind turbine wakes via large-eddy simulation. *Wind Energy*, 18(10):1815–1838.

Yılmaz, A. E. and Meyers, J. (2018). Optimal dynamic induction control of a pair of inline wind turbines. *Physics of Fluids*, 30(8):085106.

Yoshioka, S., Obi, S., and Masuda, S. (2001). Turbulence statistics of periodically perturbed separated flow over backward-facing step. *International Journal of Heat and Fluid Flow*, 22(4):393–401.

Acknowledgments

First of all, I would like to thank my supervisors Sandrine Aubrun and Boris Conan for their continuous support and advice during the last years. Thank you for your patience, motivation, guidance, constructive feedback, and for always having an open door for me and my questions, even during the challenging times we have and are currently facing.

Without the continuous technical support from Thibaud Piquet none of this work would have been possible. I think we managed to remove a significant number of bugs in several systems, but who knows how many more are hiding in the obscurity?

I would also like to thank ADEME, especially Valerie Pineau and Vincent Guenard, for being a supportive and active employer and co-financer of this thesis.

This work was carried out within the framework of the WEAMEC, West Atlantic Marine Energy Community, and with funding from the Pays de la Loire Region and Europe (European Regional Development Fund).

At BW IDEOL Adrien Courbois and Thomas Choisnet deserve a special mention at this point for their support in providing vital data, input and knowledge of floating offshore wind turbines. Without them the preliminary work would have been much more complicated!

I would like to thank all current and former members of DAUC and SEMREV+ teams, in particular Laurent Perret, Carlo Cossu and Jean-Christophe Guillautaux for their guidance on technical, theoretical and hydrodynamic topics. A special thank you also goes out to Ingrid Neunaber for (too) long discussions on all topics, professional and personal.

Further, I would like to thank everybody at LHEEA/Centrale Nantes for the good atmosphere and support I have experienced over the years.

Finally, I would like to sincerely thank my parents, by aunt and uncle, my brother, and my partner for their support and love. Barbara, Harold, Elisabeth, Helmut, Nico, Nicole, thank you for always being there for me, and for giving me confidence in myself and my work. You always motivated me and nurtured by interests in scientific and technical subjects. This PhD work would not have been possible without any you.

Titre : Caractérisation expérimentale de l'impact de la houle sur le comportement aérodynamique des éoliennes flottantes

Mots clés : éolien flottant, soufflerie atmosphérique, sillage

Résumé : La décarbonation du secteur de l'énergie est un défi majeur de notre époque. Les énergies renouvelables offrent une solution viable. L'éolien offshore peut contribuer à une grande partie de la demande énergétique. Pour accéder à l'importante ressource éolienne en mer, il est nécessaire d'installer des éoliennes flottantes. Comme la technologie est encore à l'état préindustriel, plusieurs questions restent à résoudre. En utilisant la modélisation physique à une échelle réduite, cette thèse vise à étudier le comportement instationnaire et le développement du sillage d'un modèle simplifié d'éolienne. Le modèle est placé dans une soufflerie atmosphérique et soumis à une gamme de mouvements idéalisés et réalistes. Les valeurs de vitesse moyenne restent globalement inchangées mais l'intensité de turbulence et l'énergie cinétique turbulente (TKE) sont modifiées. Le bilan TKE révèle que la production et la dissipation turbulentes sont augmentées avec l'introduction du mouvement de vague idéalisé. Les spectres d'énergie de l'écoulement sont affectés par l'introduction du mouvement. Un mouvement idéalisé à fréquence unique entraîne une signature claire dans les spectres d'énergie du sillage. Un déplacement vers des fréquences plus élevées peut être observé pour plusieurs régimes de mouvement. Un mouvement réaliste à 3 degrés de liberté affecte le sillage différemment d'un mouvement idéalisé à 3 degrés de liberté.

Title : Experimental Characterisation of the Far Wake of a Modelled Floating Wind Turbine as a Function of Incoming Swell

Keywords : FOWT, atmospheric wind tunnel, wake

Abstract : Decarbonising the energy sector is a major challenge of our times. Renewable energies offer a viable solution. Offshore wind alone can contribute a large portion of the energy demand. To access the large wind resource further offshore floating wind turbines are necessary. Floating offshore wind turbines (FOWTs) are a potential source for increased offshore energy production. As the technology is still in a pre-industrial state several questions remain to be addressed. Using physical modelling at a reduced scale, this thesis aims to investigate the unsteady behaviour and the development of the wake in a simplified FOWT model. The model is placed in an atmospheric wind tunnel and subjected to a. range of idealised and realistic motions. Each degree of freedom is studied separately and all three degrees of freedom (Dof) together. The effects of induced sinusoidal surge motion on the characteristics of the model's wake up to 8D downstream are studied. The results show globally unchanged mean velocity values but modified turbulence intensity and turbulent kinetic energy (TKE). A TKE budget analysis reveals that the turbulent production and dissipation are increased with the introduction of idealised surge motion. The energy spectra of the flow are affected by the introduction of motion. Idealised single frequency motion leaves a clear signature in the wake spectra. A shift to higher frequencies can be observed for several motion regimes. Realistic 3 Dof motion affects the wake differently compared to idealised 3 Dof motion.